INVESTIGATION OF ELECTRIC QUADRUPOLE STRENGTH IN ^{13}N USING THE $^{12}C(\vec{p},\gamma_0)^{13}N$ REACTION

by

RICHARD LLOYD HELMER

B.A.Sc., University of British Columbia, 1966
M.A.Sc., University of British Columbia, 1969

A THESIS SUBMITTED IN PARTIAL FULFILLMENT OF

THE REQUIREMENTS FOR THE DEGREE OF

DOCTOR OF PHILOSOPHY

in

THE FACULTY OF GRADUATE STUDIES

(Department of Physics)

We accept this thesis as conforming
to the required standard

THE UNIVERSITY OF BRITISH COLUMBIA

September, 1977

In presenting this thesis in partial fulfilment of the requirements for an advanced degree at the University of British Columbia, I agree that the Library shall make it freely available for reference and study. I further agree that permission for extensive copying of this thesis for scholarly purposes may be granted by the Head of my Department or by his representatives. It is understood that copying or publication of this thesis for financial gain shall not be allowed without my written permission.

Department of Physics

The University of British Columbia
2075 Wesbrook Place
Vancouver, Canada
V6T 1W5

Date Nov. 8, 1977

ABSTRACT

The E2 cross section for the $^{12}C(\vec{p},\gamma_0)^{13}N$ reaction has been measured from 10 MeV to 17 MeV in the laboratory system by bombarding an enriched carbon-12 target with beams of polarized protons. A 10 in. ϕ x 10 in. NaI(Tl) detector with a plastic anti-coincidence shield was used to detect the gamma rays. The total E2 capture cross sections were of the order of 0.2 μbarns and no resonance effects were observed. The amount of the E2 energy-weighted sum rule depleted in this energy range is (10.3 ± 4.0)%. Calculations based on a direct semi-direct capture model provide a good description of the experimental results by including only direct E2 capture and direct plus collective E1 capture.

TABLE OF CONTENTS

LIST OF TABLES

LIST OF FIGURES

ACKNOWLEDGEMENTS

I owe sincere appreciation to my supervisor, Dr. Mike Hasinoff, for the judicious prodding which has brought me to the end of my graduate student days. Refocussing my attention was made necessary by my many drinking friends at the Cecil Hotel, sailing friends at the Kitsilano Yacht Club, hockey friends at the Winter Sports Centre and school friends at the Universities of British Columbia and Washington who all distracted me from my studies.

I wish to thank the staff at the Nuclear Physics Laboratory of the University of Washington for their very friendly and helpful assistance during the course of the experimental measurements.

I wish especially to thank John Bussoletti, Katsu Ebisawa and Dr. Kurt Snover for many helpful and stimulationg discussions about this work, and Dr. Phil Dickey for putting up with me during my stays in Seattle.

I would have thanked Lee at this point for all the love and encouragement she has given me and for the tremendous amount of work she did in helping to prepare this thesis, but she preferred cash instead!

Chapter I

INTRODUCTION

1.1 General Introduction

Photonuclear reactions are a relatively simple way to obtain some of the details of the structure of the nucleus. The simplicity arises because the electromagnetic operator which mediates the interaction is relatively weak, so that perturbation theory can be used with some confidence to describe the effects of the interaction. In addition, the electromagnetic operator is well understood, so that the information acquired is direct, in the sense that no a priori knowledge of the less well known nuclear force need be assumed.

One of the most fruitful of the types of photonuclear reactions to be studied has been the excitation and decay of the Giant Dipole Resonance (GDR). This resonance, which was first shown to exist in the late forties (BA 47), is characterized by three basic properties (FU 73). First, it exists in all nuclei at an excitation energy which varies from approximately $80A^{-1/3}$ MeV for the heavy nuclei to approximately $50A^{-1/3}$ MeV for the lighter nuclei. Second, it has great strength in that it exhausts slightly in excess of the classical dipole sum rule. This sum rule was first derived for nuclei by Levinger and Bethe (LE 50), and gives a conservation law for the integrated absorption cross section. Neglecting exchange and velocity dependent forces, the sum rule is given by

$$\int \sigma \, dE = 0.06 \frac{NZ}{A} \text{ MeV} \cdot \text{barns} \qquad \text{I-1}$$

Finally, the dipole strength is concentrated in a relatively narrow energy region, the width varying from about 3 MeV for closed shell nuclei to about 9 MeV for deformed nuclei. These last two properties combine to give the GDR its resonance shape.

The GDR is viewed in the collective model as a bulk oscillation of all the protons in the nucleus moving against all the neutrons in the nucleus (GO 48 and ST 50). In shell model language, the resonance is formed by the action of the incoming gamma raising a nucleon to the next higher major shell (WI 56). This would imply that the energy of the GDR should be $1\,\hbar\omega$ (or about $41A^{-1/3}$ MeV) which is too low. Brown and Bosterli (BR 59a) pointed out that the hole that is left behind in this process must be strongly correlated in angle with the excited nucleon because the two are coupled to an angular momentum and parity of 1^-. These authors then showed that the GDR is constructed from a coherent superposition of these particle-hole states. Both the collective model and shell model descriptions of the GDR have their limits of applicability (SP 69), and both have had many extensions and refinements to improve the agreement between theory and experiment (see, for example, DA 65 and SP 69).

In the past few years, evidence of a resonance other than the GDR has come to light. This was first seen in inelastic electron scattering data (PI 71) and in reexamination (LE 72) of earlier inelastic proton scattering data (TY 58), both of which showed a new resonance located 2 to 3 MeV below the GDR. These early studies, as well as more recent ones (BE 76a), strongly suggest that this new resonance is electric quadrupole (E2) in character, and hence it has come to be called the Giant Quadrupole Resonance (GQR). The GQR had been expected for some time before its discovery, since the effective charges needed to explain electric quadrupole transition rates and moments depended explicitly on some of the E2 strength to be lying at high excitation energies (BO 69a).

The shell model depicts the GQR as a superposition of particle-hole states in which the particles have been excited through two major shells. Two modes of coherent motion are possible, one in which the neutrons and protons move in phase (isoscalar) and one in which they move out of phase (isovector). Because the interaction between the nucleons is attractive in the isoscalar mode, the resonance energy is pulled down from the expected value of 2 $\hbar\omega$. Bohr and Mottelson have shown, on quite general grounds, that the expected energy of the isoscalar GQR is $58A^{-1/3}$ MeV (BO 69b), and this is approximately the observed resonance energy. There should also be an isovector part to the GQR, which, because of the repulsive nature of the interaction between nucleons in this mode, is expected to lie at higher excitation energies.

Finally, excitation of particle-hole states within a major shell contribute to collective, isoscalar E2 strength. These states correspond to the low-lying 2^+ states of even-even nuclei.

In nuclei heavier than ^{40}Ca, the GQR seems to be localized enough to appear as a resonance, with about 80 or 90 per cent of the Gell-Mann-Telegdi (GE 53) energy-weighted sum rule (EWSR) being depleted. This sum rule is a conservation law for isoscalar E2 transitions that is essentially model independent. The EWSR is given by

$$\int \frac{\sigma(E2)}{E^2}\, dE = \frac{\pi^2}{137}\, \frac{A}{12}\, \frac{<r^2>}{Mc^2} \qquad \text{I-2}$$

where $<r^2>$ is the mean squared displacement from the centre-of-mass of a nucleon in the ground state of the nucleus, and E is the energy. The expression I-2 is developed in Appendix A.

The peak energy of the GQR lies at approximately $63A^{-1/3}$ MeV for nuclei in the range $40 \leq A \leq 120$, possibly a little higher than this for nuclei with higher mass numbers and a little lower for nuclei with lower mass numbers (BE 76a). The width of the resonance is smallest for closed shell nuclei, and decreases from 7 MeV for the lighter nuclei to 3 MeV for the heavier. Only about 30% of the EWSR is exhausted in the giant resonance region for nuclei with $A \leq 40$. This is partly due to the fact that more of the strength apparently resides in the low-lying bound states of light nuclei than heavy nuclei.

A study of inelastic electron scattering on ^{40}Ca showed that the E2 strength was rather uniformly spread between 10 and

20 MeV (TO 73). Spreading of the quadrupole strength has also been seen in inelastic electron scattering studies on ^{16}O (HO 74), where 43% of the EWSR limit was found below E_x = 20 MeV. Further examples of this effect have been seen in many radiative alpha capture reactions. For example, α capture reactions on ^{12}C (SN 74), $^{24,26}Mg$ and ^{28}Si (ME 68), ^{36}Ar (WA 73), and several other nuclei (KU 74), show that a considerable fraction of the sum rule is exhausted below $63A^{-1/3}$ MeV, and that the strength is spread from this energy down to the first excited 2^+ state (in even-even nuclei). However, inelastic alpha scattering studies on ^{40}Ca (RU 74) and several other light nuclei (KN 76) do show evidence of a GQR which exhausts about 30% of the EWSR. A similar inelastic alpha scattering measurement on ^{12}C (KN 76) showed no evidence of a GQR although a small amount (6 ± 2%) of the EWSR was seen near E_x = 27 MeV. This result is consistent with a recent continuum shell model calculation for ^{12}C (BI 75) which predicted a GQR at about this energy, but which was expected to be quite broad (Γ>>5 MeV) because of coupling to low-lying collective states (KN 76). Thus it now appears that a resonance structure persists perhaps down to A = 16 MeV, but for nuclei as light as ^{12}C, the resonance has either disappeared or has been washed out because of broadening.

Good resolution (~150 keV) alpha particle scattering from ^{16}O showed a number of peaks in the expected GQR region that were assigned to L=2 transfer (HA 76), the sum of which exhausted about 40% of the EWSR. Similar peaks have been observed with inelastic proton scattering in the giant resonance region of ^{12}C (GE 75), although these findings were not confirmed in the inelastic alpha scattering measurements of Knopfle et al. (KN 76). Thus, in addition to the spreading of the quadrupole strength in light nuclei, there is some evidence for it to be fragmented. This makes experimental observation more difficult, and may help to explain why so much less of the EWSR is observed in light nuclei than in heavy nuclei. Among the heavier nuclei, only ^{208}Pb seems to exhibit any similar fine structure (MO 76).

In general, theories of the giant resonances predict little more than total cross sections and strength distributions. For example, calculations based on the bound particle-hole excitations of Brown and Bosterli (BR 59a) can do no more than describe the gross shape of the GDR. When more complicated configurations are introduced to describe the intermediate structure, the calculations become much more difficult and the physical effects tend to become obscured. It is also necessary to include the effects of the continuum to describe the situation properly. Such calculations have been done, but they have not met with total success. For example, Wang and Shakin (WA 72) included both the above effects to describe the intermediate structure seen in the photodisintegration of ^{16}O. It was found that fairly large phenomenological E2 amplitudes were then required to fit the neutron polarization data of Cole et al. (CO 69). However, measurements of polarized proton capture in ^{15}N by Hanna et al. (HA 74a) found that the E2 amplitudes were much less than predicted. Thus the theoretical description of the giant resonances is not yet in a satisfactory state.

The present work is a study of quadrupole absorption in ^{13}N via the inverse reaction, radiative polarized proton capture on ^{12}C. The inverse $^{13}N(\gamma,p_0)^{12}C$ reaction is related to the one studied by the principle of detailed balance. An expression relating the two reactions is given in Appendix A. The reason for using polarized rather than unpolarized protons is that physically independent information is obtained on the interference between the various partial waves taking part in the reaction (GL 73). Thus there are more constraints available to help extract the parameters of interest.

Studies with capture reactions suffer from several disadvantages. First, quadrupole radiation is 10 to 100 times less intense than dipole radiation, and therefore it is difficult to observe directly. Second, information concerning giant resonances built on the ground state of the residual nucleus is all that can be obtained, although in isolated cases it should also be possible to obtain information about the giant resonances built on low-lying excited states of the residual nucleus. Third, it may happen that the GQR of the nucleus under consideration particle decays to high-lying excited states in the residual nuclei, so very little strength will appear in the ground state channels.

However, the E2 strength that is seen can often be extracted with great confidence, since the interpretation of angular distribution and polarization measurements has been well developed. In addition, the backgrounds underlying the peaks of interest in the γ-ray spectra are much less severe and much better understood than the continuum underlying the peaks in inelastic scattering spectra. Finally, for the particular case being considered, ^{13}N beta decays to ^{13}C with a half life of about 10 minutes (AJ 70) and therefore the giant resonances in ^{13}N can be studied directly only via radiative capture reactions.

Most previous $(\vec{p},\gamma)$ (the adoptions of the Madison Convention (BA 70) are used throughout this thesis) studies have concentrated on learning more details about the GDR. The first such measurement was made by Glavish et al. (GL 72) who studied the $^{11}B(\vec{p},\gamma_0)^{12}C$ reaction. The GDR in other nuclei, for example ^{4}He (GL 73), ^{90}Zr (HA 73a), ^{20}Ne (GL 73) and ^{28}Si (GL 73) have also been investigated using this technique.

The above mentioned studies were all carried out by the Stanford group, who also made the first extensive study of E2 strength with the $(\vec{p},\gamma_0)$ reaction. The results of their work on the $^{15}N(\vec{p},\gamma_0)^{16}O$ reaction have already been discussed briefly. They found evidence for a GQR in the (γ,p_0) channel which exhausted 30% of the EWSR between E_x = 20 MeV and 26.5 MeV. Recently, this reaction and the $^{14}C(\vec{p},\gamma_0)^{15}N$ reaction have been studied at the University of Washington (AD 77, BU 76a). This work will be described more fully in later chapters where comparisons to the present experiment will be made.

1.2 Review of Previous Work

Previous experimental work on $^{12}C(p,\gamma_0)^{13}N$ in the giant resonance region has centred on extracting the details of the GDR. The first measurements of the ground state gamma radiation in the giant resonance region were obtained over a very limited energy range by Warburton and Funsten (WA 62). Fisher et al. (FI 63) later investigated the region from E_p = 11 MeV to 39 MeV. Both measurements were hampered by poor beam energy resolution and by poor detector energy resolution; nevertheless, the gross features of the GDR were elucidated and a first effort (ME 65a) at describing the mechanisms involved in its excitation was made by comparison to the shell model calculations of Barker (BA 61) and Easlea (EA 62).

In order to learn more about the details of the low energy "pygmy" resonance seen at $E_x \sim 14$ MeV in the earlier measurements, Measday et al. (ME 73a) measured the 90° yield curve from E_p = 8.6 MeV to 16.0 MeV with much improved resolution. Thus they were able to observe some interesting features in this region, including two dramatic interference dips at 10.6 MeV and 13.1 MeV. The 90° yield curve was later extended to E_p = 24.4 MeV by Berghofer et al. (BE 76b) who found that the main strength of the GDR seen in the (p,γ_0) channel was centred at E_x = 20.8 MeV with a width of 4 MeV. In addition, the yield curve in the experimentally difficult region from E_p = 3 MeV to 9 MeV has been measured by Johnson (JO 74).

Angular distributions were measured at several incident proton energies between 10 and 24 MeV by Berghofer et al. A Legendre polynomial expansion of the angular distributions required the presence of odd terms to fit the data, and it will be shown in Chapter III that the odd terms arise from E2 radiation. Thus there was evidence in these measurements that E2 radiation was present and was interfering with the dominant E1 radiation, but no quantitative estimates could be made.

Evidence of E2 radiation in the giant resonance region of the stable mirror nucleus ^{13}C was seen in the inelastic electron scattering data of Shin et al. (SH 71), but again no quantitative estimates were made. This latter measurement will be discussed more fully in Chapter IV.

Further evidence of E2 strength in ^{13}C was seen by Arthur, Drake and Halpern (AR 75). These authors studied radiative neutron capture by ^{12}C at an excitation energy in ^{13}C of 18 MeV, and found non-zero odd Legendre polynomial coefficients in the angular distribution. It can be shown that radiative neutron capture is more sensitive than radiative proton capture to collective E2 strength (HA 73b), so this measurement gives strong evidence for a possible GQR in ^{13}C (although it was not clear whether this strength was isoscalar or isovector in character).

1.3 Present Work

It can be seen from the previous section that a measurement of the E2 strength in the giant resonance region is a natural extension of the work already done. It is not usually possible to extract the E2 amplitudes unambiguously even from a polarized proton capture experiment. However, for the particular instance of polarized spin 1/2 particles incident on a spin 0 (or spin 1/2) nucleus, as is the case here, these amplitudes can, in principle, be uniquely obtained (provided M1 radiation can be neglected). Therefore, a study of $^{12}C(\vec{p},\gamma_0)^{13}N$ is useful because it may be one of those cases mentioned earlier where the E2 strength can be confidently extracted.

Recently, however, considerable ambiguity has been found in the interpretation of even these simple experiments (BU 76b). These ambiguities include finding double solutions to the E2 cross sections derived from the data. This difficulty, and others, will be discussed more fully in later chapters where comparisons will be made to the present results.

The fact that it might be possible to reliably determine the quadrupole strength provides a second independent reason to study this reaction. It was mentioned earlier in the introduction that difficulties are encountered when attempts are made to calculate theoretically the properties of the giant resonances. In order to ameliorate the situation, at least temporarily, it is necessary to resort to reaction models to help distinguish among the possible alternatives. Reaction models provide a connection between the parameters of the states concerned and the experimentally observed quantities. Such a reaction model is being developed by Snover and Ebisawa (SN 75) to help understand the E2 strength seen in radiative capture reactions. This model is based on the direct semi-direct capture (DSD) model first proposed by Brown to explain E1 cross sections near the GDR (BR 64). The reaction $^{12}C(\vec{p},\gamma_0)^{13}N$ should provide a good test of this reaction model. The model and comparisons to the data presented here will be described in Chapter IV.

The energy range covered in this experiment is from 10 MeV to 17 MeV incident proton energy. This range of energies approximately covers the "pygmy" resonance observed in the 90° yield curve and in the total cross section (ME 73a, BE 76b). This resonance also appears in the 90° yield curve of the $^{13}C(\gamma,n_0)^{12}C$ reaction (JO 77), and in the $^{13}C(\gamma,n)^{12}C$ data of Koch and Thies (KO 76). Below 10 MeV, the dipole strength begins to fall rapidly. The quadrupole strength presumably falls off even more rapidly, except for the possible presence of isolated narrow states. The upper limit of 17 MeV was dictated by the maximum beam energy available.

An account of the apparatus and measurement techniques used in this experiment is given in Chapter II.

The methods of data analyses and the results are presented in Chapter III.

Comparison of the results for the $^{12}C(\vec{p},\gamma_0)^{13}N$ reaction to other experiments and to the EWSR are given in Chapter IV, in addition to a description of the attempts to fit the data with the DSD model.

Chapter V contains a summary of the results and the conclusions.

Chapter II

EXPERIMENTAL APPARATUS AND PROCEDURE

The main objective of this experiment was to measure the E2 cross section as a function of energy for the reaction $^{12}C(\vec{p},\gamma_0)^{13}N$. In addition, it was desirable to measure, as accurately as possible, polarized and unpolarized angular distribution coefficients and various other parameters related to the partial waves taking part in the reaction. All the quantities extracted from the data could then be compared to the reaction model of Snover and Ebisawa. This chapter contains a description of the equipment and procedures used to collect the data.

2.1 General Experimental Arrangement

A schematic diagram of the experimental set-up is given in Figure II-1. The incident polarized proton beam was produced by the University of Washington Lamb-shift Polarized Ion Source (FA 71). The beam was then accelerated by the University of Washington FN tandem Van de Graaff accelerator, bent through a 90° analyzing magnet and directed down the appropriate beam line (30°) by a switching magnet. The beam was magnetically focussed through a collimator and skimmer system onto the target. After passing through the target, the beam travelled

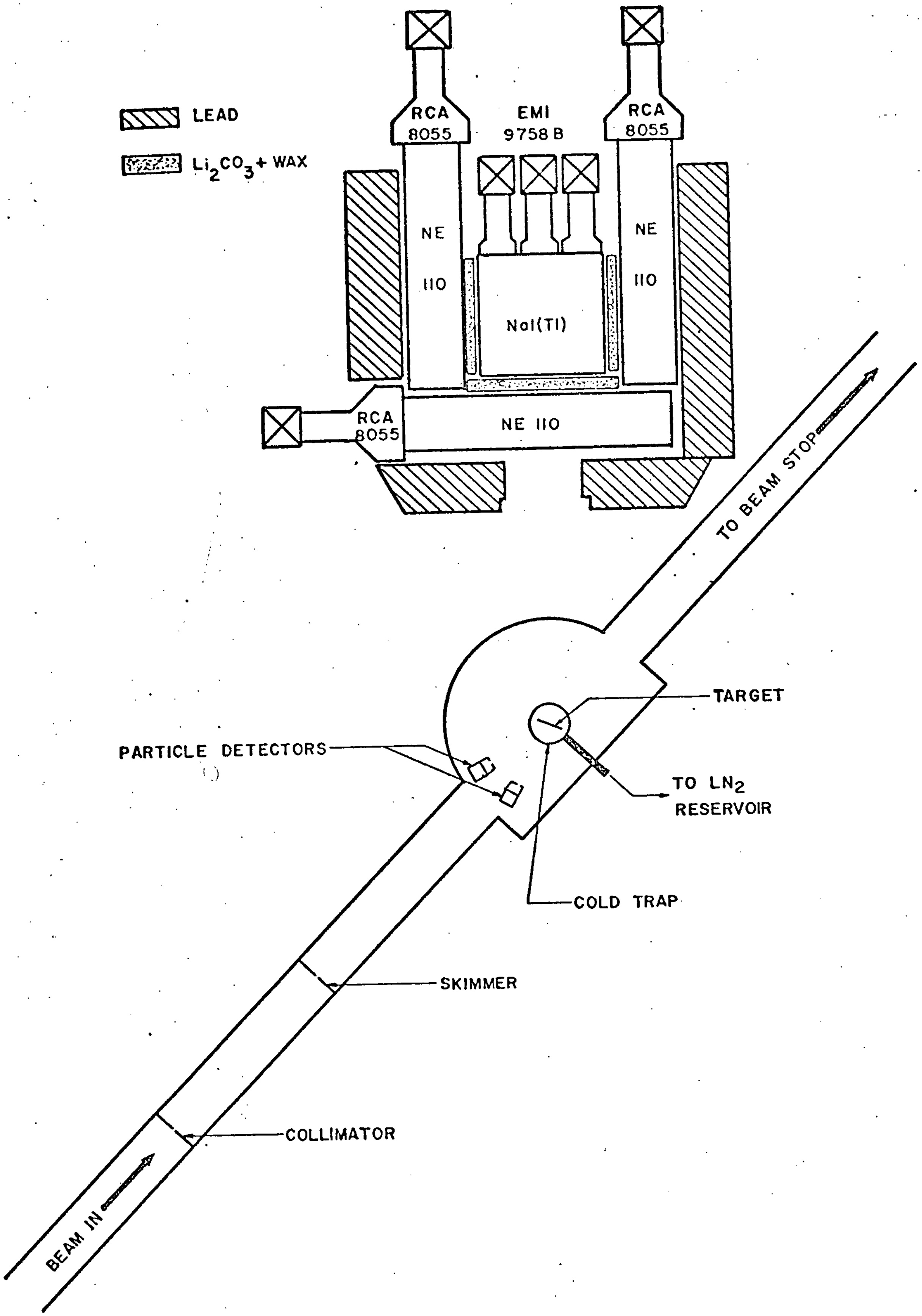

Fig. II-1 : Schematic view of the beam line.

another 7 m further downstream until it reached the beamstop located behind concrete and wax shielding. The long downstream beam tube served as the Faraday cup.

The beam line was optically aligned by viewing through a telescope mounted at the downstream end and focussing on a cross-hair located at the exit of the switching magnet. The collimator and skimmer, which are located in a separate section of beam line, were then accurately centred by shifting this section the necessary amount. Finally, a cross-wire was mounted in the centre of the target chamber and the chamber was moved until the cross-wire was centred in the beam line. At the same time, a plumb bob was used to check that the cross-wire was vertically above the centre axis of the gamma ray angular distribution table.

The spin orientation of the polarized proton beam was changed by reversing the quench and argon fields. This was controlled by means of a flipper described by Adelberger et al. (AD 73). The polarization could be flipped automatically from one to ten times a second, or it could be flipped manually when desired. The flipper also provided a logic routing signal which was used to route other signals according to whether the proton spin was up or down.

The amount of beam on target was limited by the counting rate in the NaI(Tl) detector. Currents from 30 namps to 60 namps were satisfactory, depending on the beam energy. The beam striking the collimators was continuously monitored and was typically 0.2 namp. If the collimator current rose as high as 2 namps, the experiment was stopped and the beam refocussed.

This was necessary to prevent the appearance of troublesome backgrounds in the spectrum.

The target holder was a ladder on which three targets could be mounted. One of these was an aluminum blank with the same diameter hole as the actual target. The ladder could be rotated to any orientation about a vertical axis. This was useful in that it allowed the target holder and ladder frame to be turned out of the line of sight of the gamma detector.

The target holder was surrounded by a copper cylinder which was maintained at liquid nitrogen temperature. This helped to reduce any buildup of beam line contaminants on the target. A slot was cut out of the middle of the cylinder to allow the beam and scattered protons to pass through freely. A copper strip 0.002 inches thick was soldered over the slot where the gamma rays passed to the detector. This produced virtually no attenuation of the gamma flux, but did improve the vacuum in the immediate vicinity of the target.

Undesirable backgrounds can arise from beam striking the aluminum target frame or the copper cold-trap. However, a collimator of diameter 3/16 inch and skimmer of diameter 1/4 inch seemed to be small enough to prevent this happening. Checks were made at various times by passing the beam through the aluminum blank in the target holder. No elastically scattered protons were observed in the particle spectra under these conditions.

2.2 Gamma Ray Spectrometer

The most important instrument used in this experiment was the gamma spectrometer. It consisted of a large central NaI(Tl) detector surrounded by a plastic anti-coincidence (AC) shield. This spectrometer has been described in detail elsewhere (HA 74b), and general considerations for the design of such spectrometers have been given by Paul (PA 74), so only the salient features will be described here. A view of the spectrometer is shown in Figure II-1.

The central crystal is in the form of a cylinder 25.4 cm in diameter by 25.4 cm long. It is viewed by seven EMI 9758B photomultipliers.

The surrounding anti-coincidence shield, manufactured from the plastic scintillator NE 110, is 10.8 cm thick. It covers the sides and front face of the central crystal. The cylinder is viewed by six phototubes and the front plastic by two phototubes (RCA 8055).

The space between the two detectors is filled with a 1 cm thick self-supporting mixture of lithium carbonate and wax (LI 75). This helps to reduce the background due to slow neutron capture in the central crystal.

The sides of the entire assembly are surrounded by 4 inches of lead to reduce the cosmic ray flux reaching the central crystal. The front is also shielded by 4 inches of lead. This reduces the low energy gamma background reaching the detector from the target. The front shielding has provision for different size collimators to be inserted. The resolution of the spectrometer is improved with smaller collimators, but since this was not of paramount importance in the present experiment, the insertion hole, with a diameter of 6 inches, was left completely open.

The gamma spectrometer was located sufficiently far from the beam line - about 16 inches from the centre of the target to the front face of the lead shielding - that it could be swung through angles from 43° to 137°. It would have been desirable, of course, to have had a larger angular range in order to reduce the errors in the experiment. However, this would have meant having the detector further back with a consequent decrease in counting rate.

The constancy of the distance from the detector to the centre of the chamber was checked by mounting a RaTh source in the target holder and measuring the "angular distribution" as the detector was swung through its range. The counts recorded were isotropic to within 1/4%. This test also ensured that absorption through the chamber walls was uniform.

2.3 Gamma Spectrometer Electronics

A fairly complex, but now basically standard, system for processing the signals from the gamma spectrometer was utilized. The fundamental idea behind the electronic system is to veto events which are affected by pile-up, and to reject cosmic ray events and events for which some of the energy escapes from the central crystal. All of these effects worsen the detector resolution and often make it difficult to extract from the spectrum the number of true events associated with the reaction being studied. A block diagram of the electronics is given in Figure II-2 and a description follows.

The signals from the seven phototubes on the NaI(Tl) detector are actively summed, then sent to a fan-out from which one branch, the linear signal, is amplified and sent to a linear gate. A second branch from the fan-out is cable clipped to a width of 50 nsec, amplified and sent to a constant fraction discriminator called the High Level Discriminator (HLD). The bias on the discriminator is set just far enough below the region of interest in the spectrum that any threshold effects of the HLD have disappeared. In this way, pile-up of two low level pulses is effectively prevented from appearing in the spectrum. No attempt is made to discriminate against high-low pile-up.

One output of the HLD opens the linear gate, allowing the linear signal to pass to an analog-to-digital converter (ADC) interfaced to the Nuclear Physics Laboratory SDS 930 computer. The signal is shaped correctly and delayed appropriately for the ADC by a linear gate and stretcher. A second output from the HLD is fed to two coincidence circuits via an updating (dead time-less) discriminator to check for coincidences with the AC channel.

The signals from all eight phototubes on the plastic scintillators are actively summed. The resultant pulse is then amplified, cable clipped to a width of 80 nsec, amplified again and passed to an updating discriminator. The bias level on

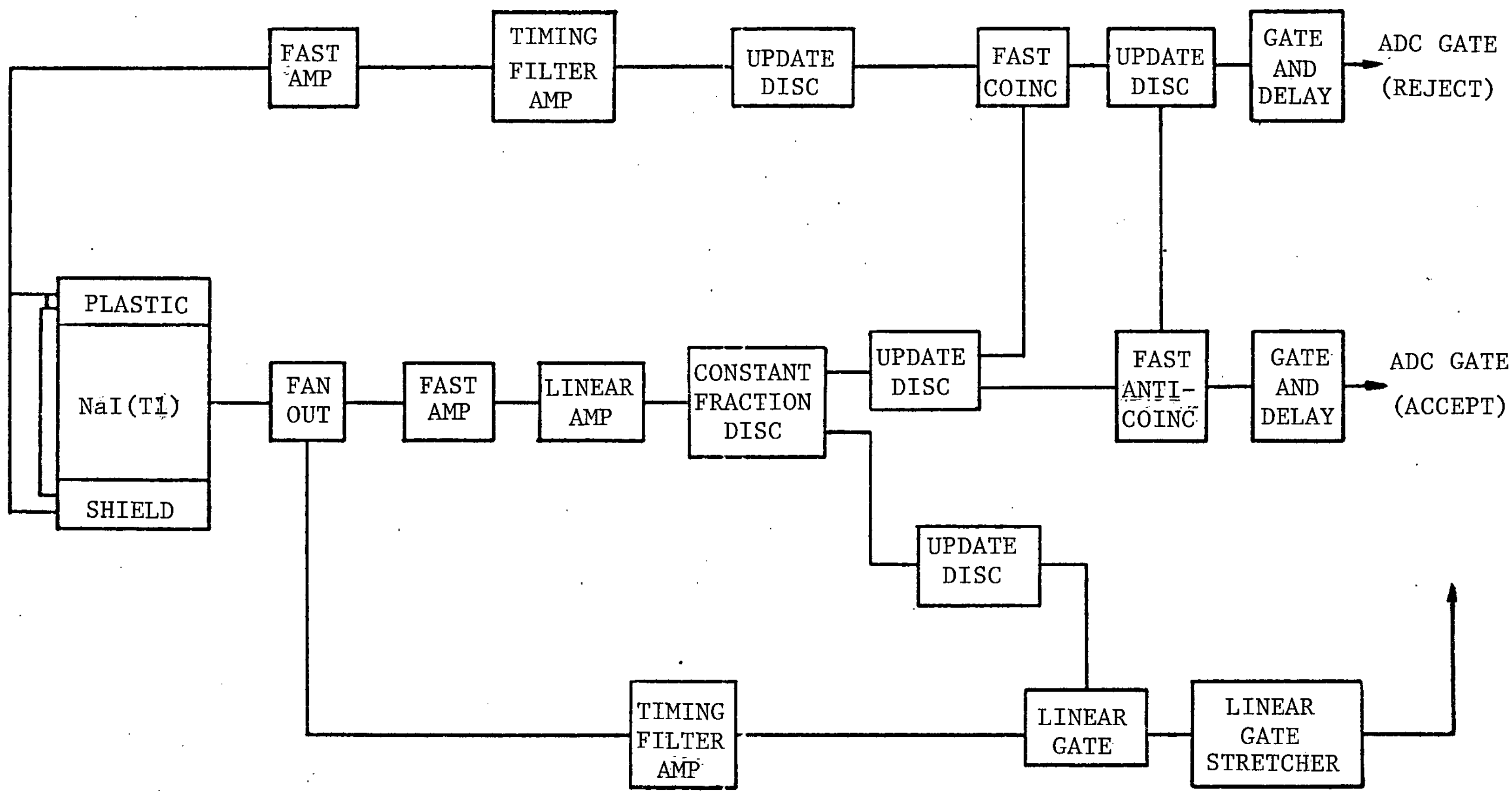

Fig. II-2 : Block diagram of the gamma spectrometer electronics.

this discriminator is set just above the noise, somewhere around 100 keV, and the output is fed into a fast coincidence with the output of the HLD (after suitable delays - not shown). A coincidence here implies that energy has been deposited in both the central crystal and the surrounding shield. Therefore the linear signal is routed into a portion of computer memory labelled "reject", because these events are normally discarded. Actually, in this experiment, the "reject" spectra were used in the subsequent analysis.

If there is no coincidence between the two channels, then in principle no energy was lost from the central detector. Hence linear signals for these events are routed into the "accept" portion of memory. This is accomplished by the second coincidence test, which requires a coincidence between the HLD output and a null output from the first coincidence (again after suitable delays).

The reject and accept routing pulses are further split according to whether the proton beam is spin up or spin down. This is accomplished using the flipper referred to earlier.

In addition, a signal from a pulse generator was fed directly into the fan-out in parallel with signals from the NaI(Tl) detector. The pulser was fired by the current integrator and hence gave a direct measure of the dead time in the detector electronics system. The pulser was also used to check the linearity of the electronics prior to each set of measurements.

Various outputs were scaled in case it became necessary to consider rejecting a questionable data point. This is not shown in the figure. The scaled outputs included the number of accept and reject routing pulses and the number of counts in the plastic scintillators. In addition, all events which deposited more than about 250 keV in the NaI(Tl) detector were scaled, and the counting rate for these events was kept below 40 kHz. The signals for these low level events were derived from a separate branch of the fan-out.

Finally, it was necessary to stabilize the phototubes on the NaI(Tl) detector against drifts incurred by variable counting rates. This was accomplished dynamically by an external feedback system which adjusted the high voltage on the tubes in such a way as to keep constant the height of the pulse from some peak in the low energy part of the spectrum. Gamma rays from the inelastically excited level at 4.43 MeV were used for this purpose.

An example of a spectrum obtained with the spectrometer is shown in Figure II-3. The HLD cut off is noted around $E_\gamma = 7$ MeV, and the part of the spectrum below this energy has been omitted. It is seen that the accept spectrum is considerably improved over the combined spectrum. Removal of those events associated with the loss of one of the pair annihilation quanta is responsible for most of the improvement. The resolution (full width at half maximum) of the accept part is about 4.0% compared to 7.0% for the sum spectrum.

The background above the peak results mainly from cosmic rays, although there is a small excess over the background expected from this source in the accept spectrum. This excess background is due partly to high energy gamma rays from the

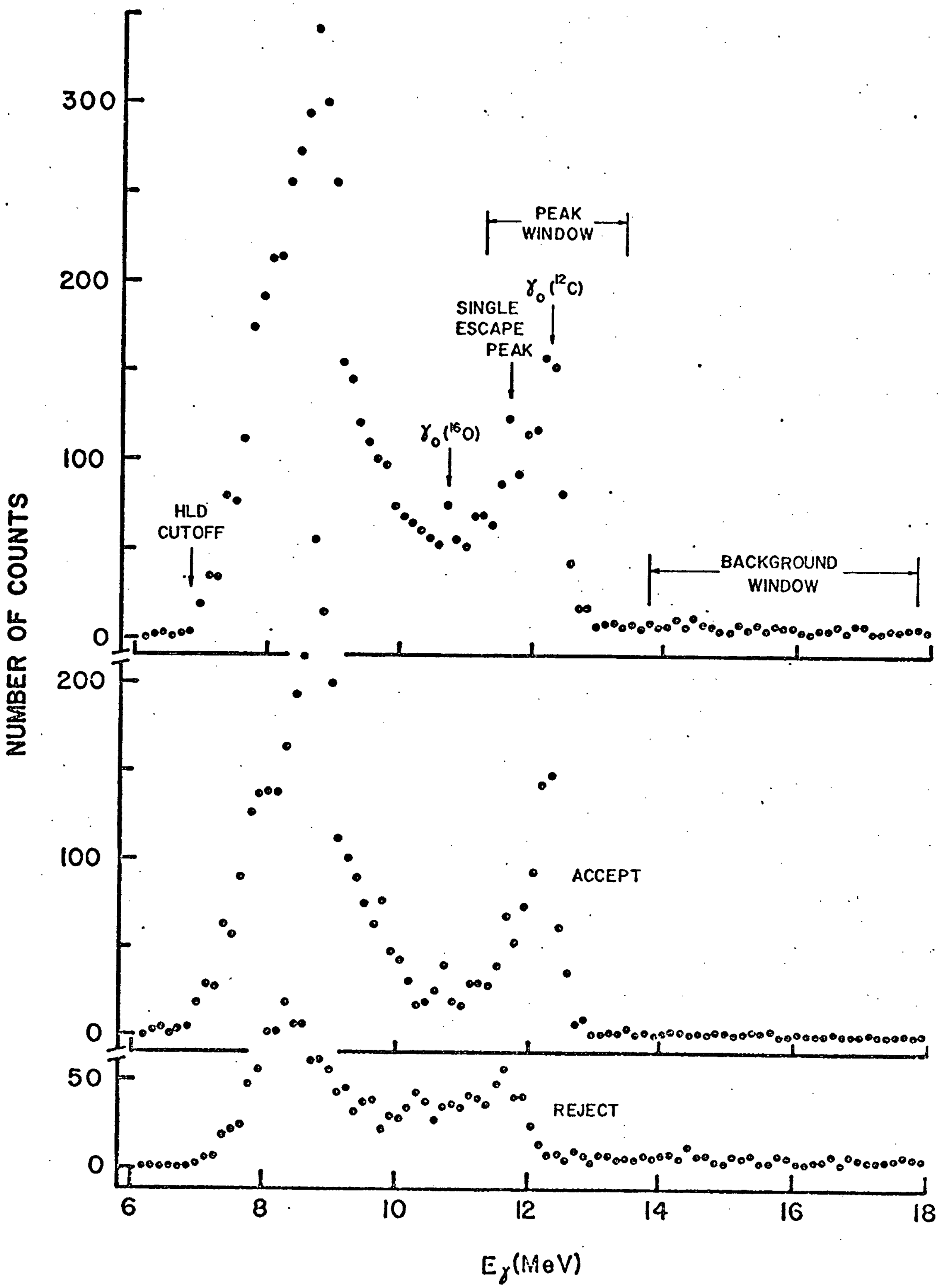

Fig. II-3 : $^{12}C(\vec{p},\gamma_0)^{13}N$ gamma ray spectrum at $E_{\vec{p}}$ = 11.2 MeV.

$^{14}N(\vec{p},\gamma)^{15}O$ reaction, although the particle yields indicated there was only a trace of ^{14}N in the target. Some of the excess background might also arise from pile-up, or from some unidentified contaminant in the target. In any event, it did not prove to be a difficult problem to handle.

A peak due to $^{16}O(\vec{p},\gamma_0)^{17}F$ is also noted around E_γ = 11 MeV. Without the excellent detector resolution, this peak would have merged with the $^{12}C(\vec{p},\gamma_0)^{13}N$ peak and would have been included in the analysis, although this would not have been a serious problem in the present case.

The pulser peak lies off-scale at an equivalent gamma ray energy of about 30 MeV.

The window regions in which the number of counts was summed are also shown. The positioning of the windows is discussed in Chapter III.

2.4 Particle Detection

Two lithium drifted silicon detectors were located in the scattering chamber as shown in Figure II-1. Their purpose was to provide a constant monitor of the beam polarization via the $^{12}C(\vec{p},p_0)^{12}C$ reaction, and to provide a secondary means of data normalization. They were symmetrically placed at 160° to the incident beam direction. This angle was far enough back not to interfere with gamma rays going to the gamma spectrometer when it was located at back angles, but not so far back to interfere with the incoming beam.

Collimators consisting of vertical slits 0.125 inches wide by 0.44 inches high were mounted in front of the detectors. The distance from the centre of the target to the collimators was 4.25 inches.

Signals from the detectors were fed to Ortec 109A preamplifiers located immediately outside the target chamber and thence to the counting room where they were processed. A block diagram of the electronics is shown in Figure II-4, and a description follows.

From the linear amplifier, one branch was sent to a linear gate and stretcher, where the signals were delayed appropriately and then passed to a sum amplifier and the ADC.

The logic branch was sent to a single channel analyzer (SCA) where a low level discriminator was used to cut out the low energy pulses. The counting rate for pulses above the discriminator threshold was about 2 kHz. The output from the SCA was mixed with the logic signals from the pulser and then sent to route linear signals present at the ADC into the appropriate portion of memory.

The logic signals were also fed to an "exclusive-or" mixer. The purpose of the mixer was to gate the ADC when there was a logic pulse present from only one detector. Otherwise, the ADC would not know from which detector the linear pulse had come, and in any event, this linear signal from the sum amplifier would probably be a pile-up of pulses from both detectors.

The pulser was fired by the current integrator so that dead time corrections could be made directly. Unfortunately,

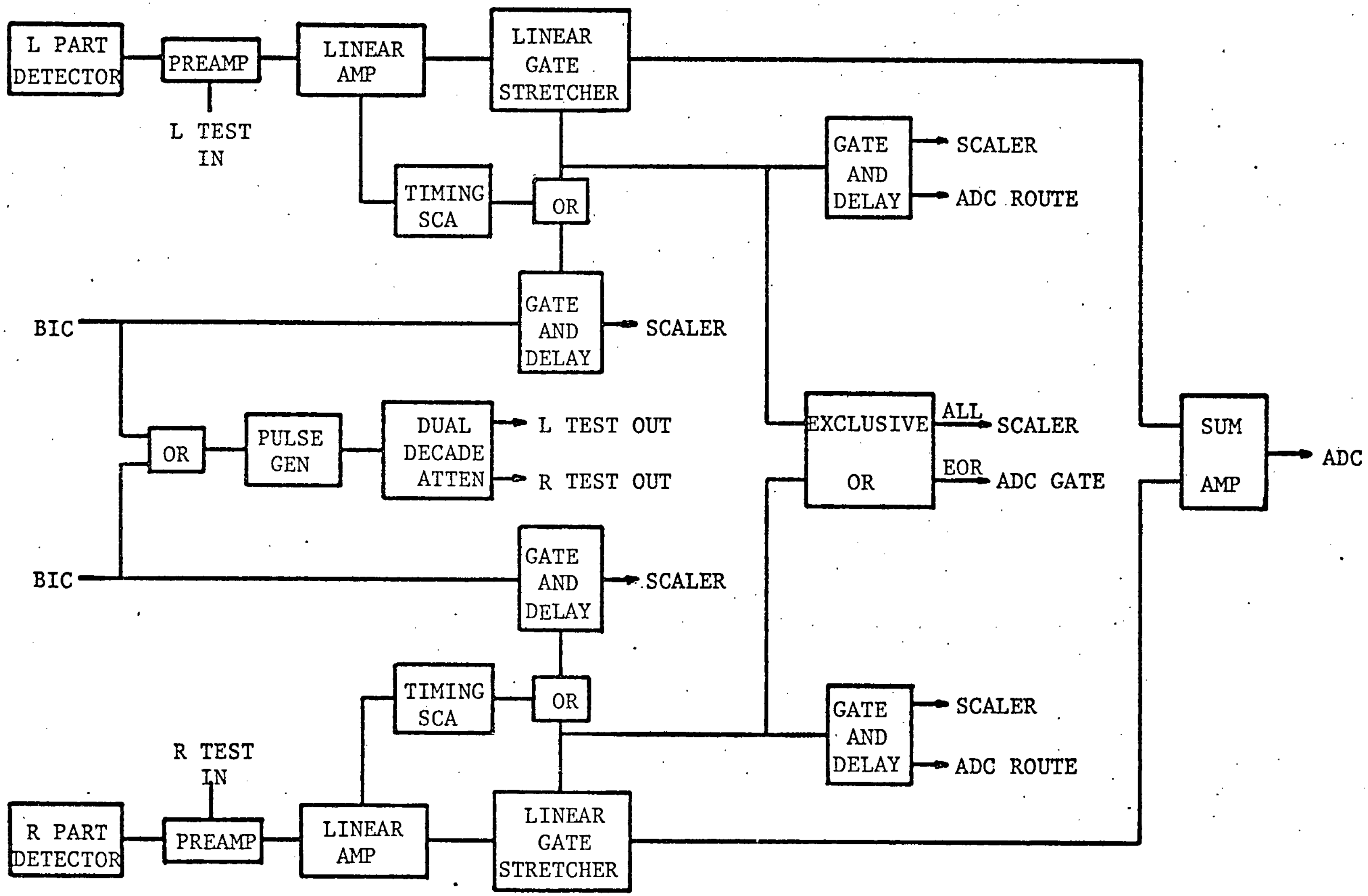

Fig. II-4 : Block diagram of the particle detector electronics.

the pulse generator later appeared to be faulty, and it was found that the results were more self-consistent if the counts were not dead time corrected.

As with the gamma electronics, all linear pulses were further separated according to whether the proton spin was up or down.

Several of the branches were scaled. These are shown in the figure.

An example of a particle spectrum is given in Figure II-5. The strongest peaks are from elastic scattering off ^{12}C and inelastic scattering leaving ^{12}C in its first excited state. The peaks resulting from elastic scattering off ^{14}N and ^{16}O are also clearly seen, but note the logarithmic scale. The pulser peak lies below the threshold for linear signals so that it is in a background-free region of the spectrum.

2.5 Targets

Three different targets were used in the course of this experiment. A natural carbon target of thickness 1.9 mg/cm^2 was used for the measurement at $E_{\vec{p}}$ = 13.5 MeV. It was found that gamma rays from the $^{13}C(\vec{p},\gamma)^{14}N$ reaction contaminated the spectrum above the peak of interest (natural carbon contains about 1.1% ^{13}C). Although it would always have been necessary to subtract a background due to cosmic rays, the presence of the $^{13}C(\vec{p},\gamma)^{14}N$ gamma rays made the background subtraction less certain. Thus it was decided to run with pure ^{12}C targets. It

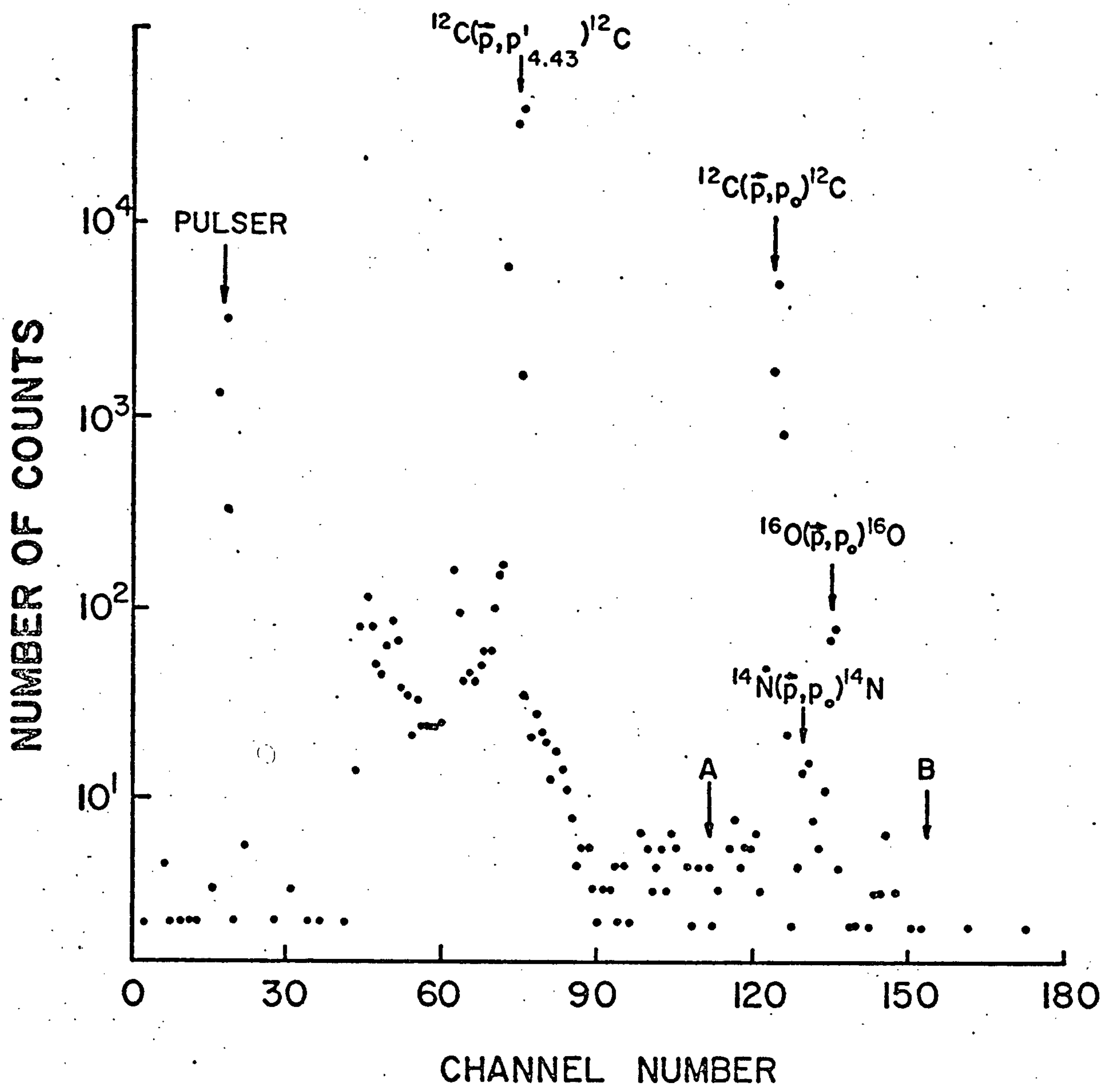

Fig. II-5 : Particle spectrum at $E_{\vec{p}}$ = 11.2 MeV. Note the logarithmic scale of the ordinate. The arrows 'A' and 'B' define the window region referred to in the text (Chapter III).

was hoped that only the much more certain cosmic ray background subtraction would then be necessary.

Accordingly, two targets were ordered from Penn Spectra Tech.[1] The targets were approximately 1 mg/cm^2 thick. The thickness was measured by comparing yields in this experiment to the elastic scattering cross section data of Meyer et al. (ME 76) and the inelastic scattering data of Swint et al. (SW 66). A gamma spectrum from one of the targets is shown in Figure II-3 and a particle spectrum is shown in Figure II-5. Although there is no evidence for the presence of ^{13}C in these spectra, it has already been pointed out that there is some contamination from nitrogen and oxygen. By comparing the particle yields in this experiment with the differential cross section data of Daehnick (DA 64), it was found that the oxygen content in the target was about 0.01 mg/cm^2. Comparison of the nitrogen yield to the data of Hintz (HI 57) indicates the nitrogen content is only 0.0004 mg/cm^2. All runs except those at 13.5 MeV were taken with one or the other of these enriched ^{12}C targets.

2.6 Current Integration

The current collected in the Faraday cup was measured by a Brookhaven Instruments Corporation (BIC) current integrator.

---

[1] Penn Spectra Tech
411 Bickmore Drive
Wallingford, Pennsylvania 19086

The BIC delivers a routing pulse for a certain amount of charge collected. These pulses were divided, as usual, according to whether the proton spin was up or down. Scalers were then used to record the integrated charge.

The BIC output pulse was also used to fire the pulsers in the detector electronic circuits to keep track of dead times.

2.7 Polarization Measurements

The beam polarization was continuously monitored during the runs by the $^{12}C(\vec{p},p_o)^{12}C$ reaction whose analyzing power is well known (ME 76). In addition, the polarization was measured several times throughout the runs with a helium polarimeter (BA 75) in a separate beam line. The particle detectors were placed at 112.5° to the incoming proton beam since at this angle, the analyzing power for the $^{4}He(\vec{p},p_o)^{4}He$ reaction is close to 1.0 for all the energies measured (SC 71).

2.8 Data Accumulation

Three different runs were made in this experiment. In the first, data were obtained only for a proton energy of 13.5 MeV. In the second, data were taken at 12 MeV, 14 MeV and 16 MeV. In the final run, data were gathered at 10 MeV, 11.2 MeV, 12.8 MeV, 15 MeV and 17 MeV. Because the GQR lies at a high excitation energy, there should be a large number of allowed decay channels and hence the resonance will be quite broad.

Thus it was felt that measurements in approximately 1 MeV steps would be adequate to survey the region.

In order to help detect possible systematic errors, the data at most energies were collected with four passes over the angles measured. At one energy (17 MeV), only two passes were made because of time constraints and at two other energies (11.2 MeV and 13.5 MeV) three passes were made.

It was necessary to have the face of the target pointing at an angle greater than 20° from the gamma detector angle to avoid absorption through the target holder. Therefore the angles 43°, 55°, 70°, 90°, and 137° were measured with the target at 110°. The angles 43°, 110°, 125°, and 137° were measured with the target at 70°. The end points were measured with the target at both orientations in each pass to ensure that there were no systematic effects associated with the target rotation. None were observed.

The angles were chosen to be equal to the zeros of the various Legendre polynomials. There was no other reasonable criterion for the choice of angles - for example, no angle is more sensitive than another to the presence of E2 radiation.

When the gamma spectrometer was located at the forward angles, 6 inches of lead was placed between the beam collimators and spectrometer collimator. This prevented radiation produced by the beam striking the collimators from reaching the NaI(Tl) detector directly.

Some runs were taken by collecting the complete charge of 30 μcoul first with the proton spin in one direction, then in the other. Others were taken with the spin flipping automatically once a second. When this was the case, the electronics was automatically shut down for 1 msec while the fields were reversing.

The data for each measurement were stored directly in the SDS 930 computer. A preliminary analysis of the data was carried out at the end of each run while the detector angle was being changed. The data were also written onto magnetic tape for later off-line analysis.

Chapter III

DATA ANALYSIS AND RESULTS

The main aim of this experiment was to measure a very small E2 cross section in the presence of a very large E1 "background". Thus it was necessary to scrutinize the data very carefully to ensure that no systematic biasing of the results occurred. In this chapter, the methods used to analyze the data and to check its consistency will be described, and then the results of the analysis will be presented.

In several places throughout the chapter, comparison is made between the experimental results and the results of a direct semi-direct model calculation. The model and the parameters used in the calculations will be described in Chapter IV.

3.1 Gamma Ray Spectra Analysis

There are essentially two ways to determine the area of the peaks in the spectra. One is to use standard line-shapes to fit all the peaks of interest. This is useful when the peaks are sitting on large backgrounds or when two or more of them overlap. The other is to define a window around the peak or peaks of interest and simply sum the counts within this window. In this experiment, the spectra were reasonably clean and the peaks were well separated except for a small number of high energy background gamma rays from proton capture on oxygen and nitrogen. Thus it was decided to use the second method of analysis, taking care to place the lower limit of the window above the peak from the reaction $^{16}O(\vec{p},\gamma_0)^{17}F$, which has a Q-value of 0.6 MeV. It was also necessary to subtract a small background which arose from the contaminants in the target and from cosmic rays which penetrated the lead shield. The same computer program was used to analyze the data both on-line and off-line (BU 75a). A brief description of the analysis procedure follows.

First, a window was defined as a fraction (>1.0) above and a fraction (<1.0) below the centroid of a strong peak in the spectrum and an initial guess of the centroid of this window was made. A new centroid was then calculated for the window so defined, and from this centroid a new window was defined and a new centroid calculated. This procedure continued until successively determined centroids agreed to within 0.1 channel, since the error in the centroid position was typically 0.1 channel. For the purpose of defining the centroid, the spin up and spin down spectra, including both the accept and reject parts, were summed.

When the centroid had been determined, the counts were summed within a second window, also defined as fractions of the centroid. For the data at 16 MeV and 17 MeV, there were strong lines in the spectra from inelastic scattering off the 12.7 MeV and 15.1 MeV levels of ^{12}C, respectively. At these energies, the centroid was determined from these strong peaks since they are less susceptible to shifts due to background variations. For all other energies, there was no peak stronger than γ_0 in the spectra, hence this line was used to define the centroid. An example of a window region defined in this way is shown in Figure II-3.

The counts within the window for the individual spin up and spin down, accept and reject, spectra, were then summed. Yields in the fractional channels at the ends of the window were determined by linear extrapolation between the channels above and below the window limit. The counts in a background window defined above the peak window were summed for each of the four spectra. The background counts were normalized to the number of channels in the peak window, and were then subtracted from each peak sum. The error of the counts in each peak was given as simply the statistical error; that is, (total area + background area)$^{1/2}$.

The yields were corrected for dead time by dividing by the number of counts in the pulser peak. This automatically corrected for any differences in the charge collected during the spin up and spin down parts of the run. Alternatively, the spin up and spin down counts could be normalized according to the number of counts obtained in the particle detectors. Differences between the normalization methods will be discussed in section 3.4.

Ratios of counts in the reject spectra to counts in the accept spectra were calculated for each spin up and spin down run. In Figure III-1, these ratios are plotted as a function of angle for one energy. It is seen that the average values

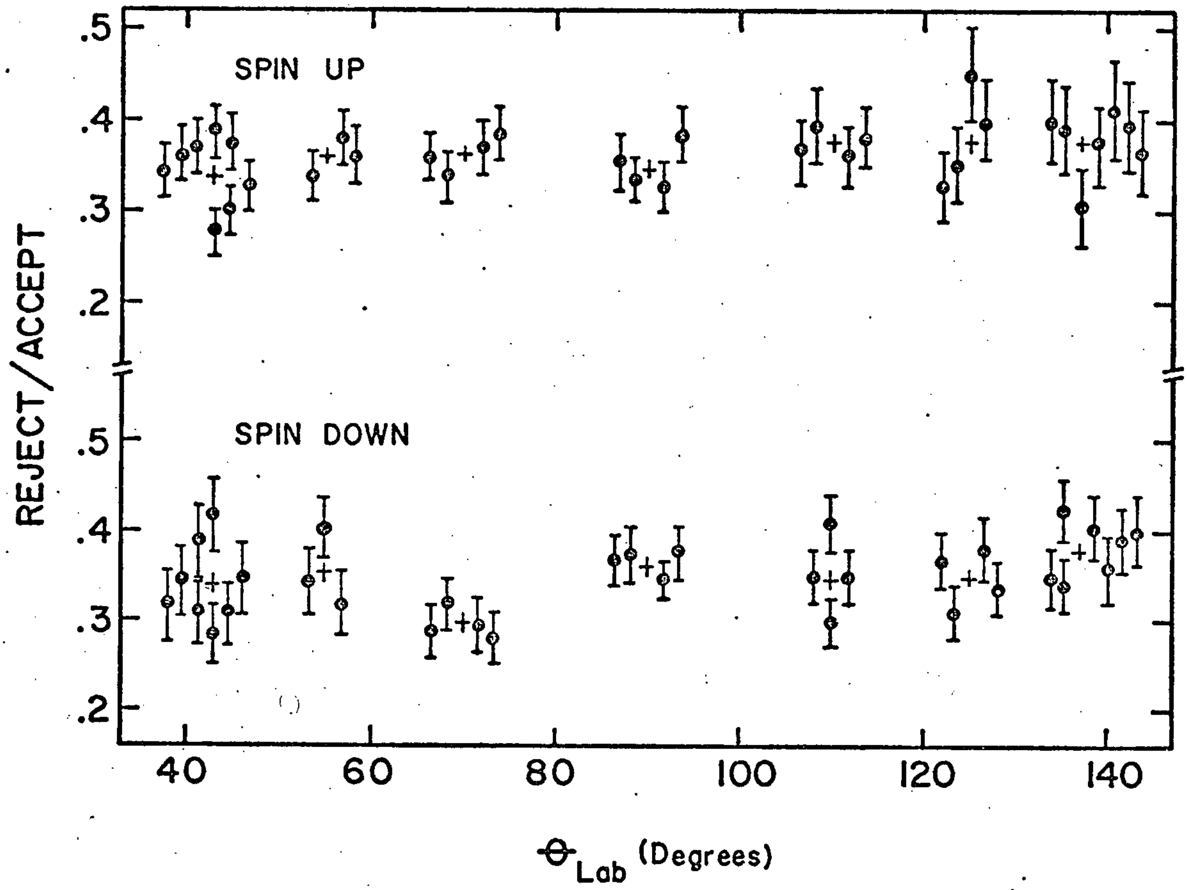

Fig. III-1 : Reject to accept ratios for $E_{\vec{p}}$ = 10 MeV. The plus signs are the averages at the given angles and spin orientations; the surrounding points with error bars are the corresponding experimental measurements. See text for discussion.

fluctuate a fair amount as a function of angle, particularly for the spin down spectra. In addition, there is a fair fluctuation about the average value at each angle. Although different in details, the data at each energy showed similar variations. In some, but not all, cases, the fluctuations seemed to be correlated with the total number of counts recorded in the AC shield. It was because of these variations that it was necessary to include the reject spectra in the analysis. The repeat measurements at each angle were found to be more self-consistent when this was done compared to using only the accept analysis.

3.2 Particle Spectra Analysis

The particle peaks were also summed within a defined window. Channel locations for the peak window and background windows below and above the peak were read into the computer on cards. An option was to have the program slide the windows until the centroid calculated for the peak was within one channel of the centre of the peak window. In the initial analysis, the four peaks shown in Figure II-5 were analyzed. It was found in all cases that the beam polarization measured by the $^{12}C(\vec{p},p_0)^{12}C$ reaction agreed within errors with the measurements using the helium polarimeter. After this was established, the final analysis was carried out with a broad window defined over the ^{12}C, ^{14}N and ^{16}O elastic scattering peaks (between arrows 'A' and 'B' in Figure II-5). Summing all three peaks improved the statistical accuracy and reduced background uncertainties.

The program calculated the charge and solid angle asymmetries associated with the polarized beam, and these were monitored throughout the runs. The analyzing power was also calculated and monitored. Expressions for these quantities are given in Appendix C.

3.3 Results from the Particle Analysis

The three asymmetries for the summed peaks at $E_{\vec{p}} = 15$ MeV are plotted in the upper half of Figure III-2. These are quite typical results. In this particular case, both the solid angle asymmetry and analyzing power show a slow increase as well as more rapid, but not statistically significant, fluctuations superimposed on this general trend. There is no simple explanation for these results. They could be due to small beam steering effects which may or may not be coupled with target non-uniformities. They could be real beam polarization changes, possibly for only one spin orientation. The dashed lines in the charge ratio and solid angle asymmetry plots correspond to measurements made with unpolarized beam. The measurements of the analyzing power with unpolarized beam will be discussed in section 3.5.

It is in general very difficult to distinguish between beam shifts and polarization changes unless there is a reaction taking place in the target for which the analyzing power is

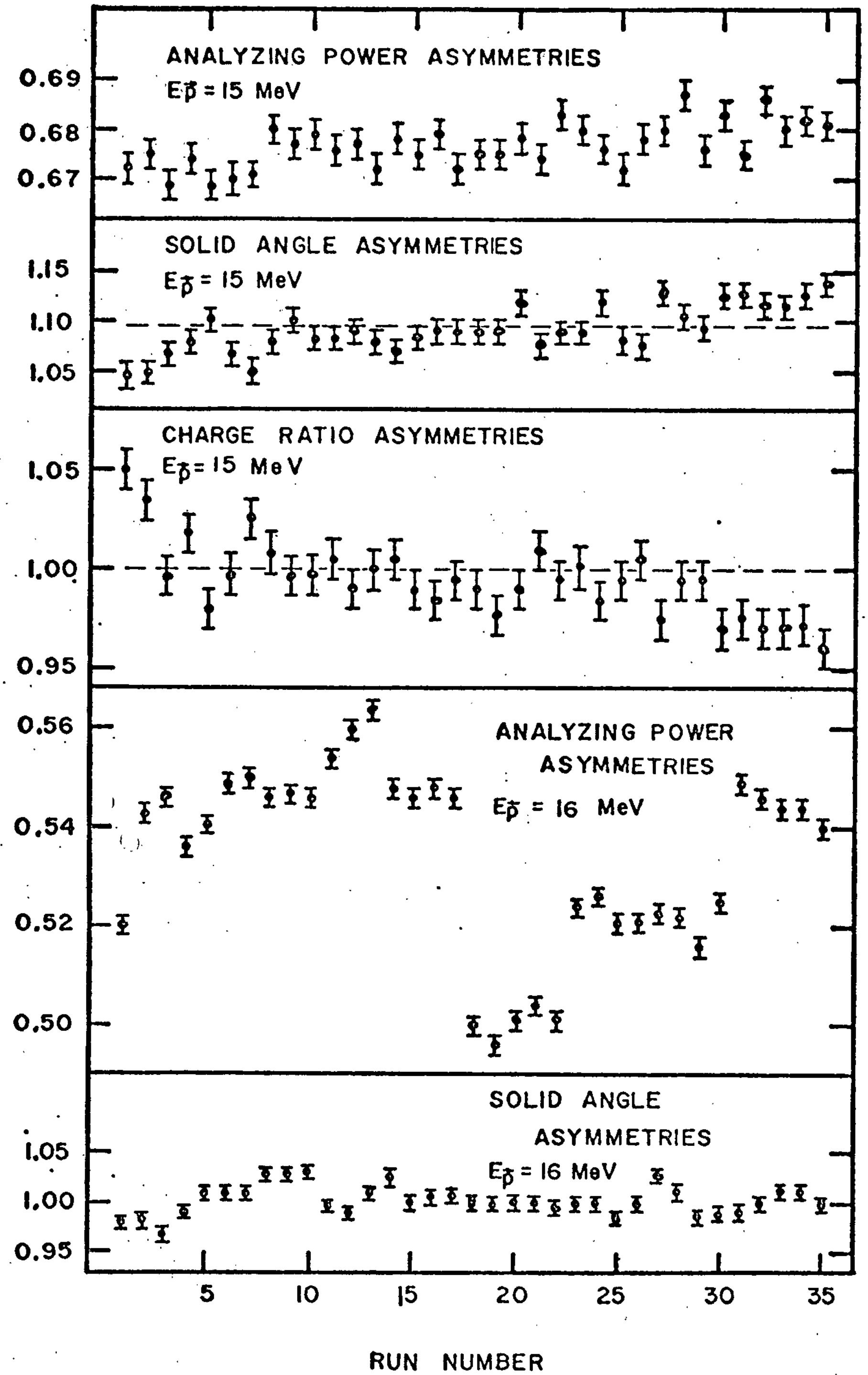

Fig. III-2 : Polarized proton beam asymmetries at $E_{\vec{p}}$ = 15 MeV and 16 MeV.

close to zero. Such is not the case here, but the drifts are small in any event. If they are due to polarization changes, then the change of 1 or 2% is no more than the assumed error in the polarization, as will be seen later.

An exception to these comments occurs in the data for $E_{\vec{p}}$ = 16 MeV. Shown in the bottom part of Figure III-2 are the beam polarization and solid angle asymmetries measured at this energy. It is seen that the polarization takes a substantial drop at run 18, and then returns to the original average value in two stages. There is no corresponding variation in the solid angle asymmetry, thus there is fairly strong evidence that the polarization change is real. The gamma data at 16 MeV were therefore handled slightly differently from the data at other energies and this will be discussed in section 3.5.

3.4 Results from the Gamma Ray Analysis

There were four possible final results for the gamma ray analysis at each angle, according to whether the accept only (ACC) or the accept plus reject (A+R) sums were used, normalized to either the charge collected (Qnorm) or the particles counted (Pnorm) for each spin orientation. All four results were punched out on cards with their respective statistical errors and analyzed by a computer program in which the results were averaged at each of the seven angles for all four possibilities. The output from this program included these averages and their respective errors transformed into the centre of mass frame.

It was after this averaging was done that it was noticed that the A+R results were more self-consistent than the ACC results. It was also noted that the Qnorm results were more consistent than the Pnorm results. The method of determining these facts was as follows.

At the seven angles measured for each energy, the number of results that were within one standard deviation (1σ) of the average was counted, the number between one and two standard deviations (2σ) was counted, etc. Assuming these numbers follow a normal distribution, 67% should be within 1σ, and 94.5% should be within 2σ. The number of points that could be expected to lie more than 2σ away from the appropriate average can be found from the mean and standard deviation of the binomial distribution

$$B(n) = \frac{N!}{n!(N-n)!} p^n (1-p)^{N-n} \qquad \text{III-1}$$

where N is the number of samples and n is the number of events that occur with probability, p. In the normal case of four passes over the angular distribution, there are 36 data points and, for $p = .055$, the mean (Np) is 2.0 and the standard deviation ($\sqrt{Np(1-p)}$) is 1.4. Thus no more than two or three points would be expected to lie more than 2σ away from the appropriate average. This was always true for the Qnorm A+R results. A small increase in the errors was required to make it true for the Qnorm ACC results. The Pnorm results also needed a slight increase in the errors. The latter result can be understood when it is recalled that the particle yields were fluctuating because of small beam shifts or polarization variations, while the charge collected was not sensitive to these changes. There may also have been small dead time variations in the particle yields for which no corrections were made. The improvement of the A+R over the ACC results is understood from the fluctuations mentioned earlier in the reject/accept ratios.

Thus the Qnorm A+R analysis of the raw data was the most self-consistent. In addition, because a larger number of counts was being used in the analysis, the A+R results had smaller statistical errors than the ACC results. For the above two reasons, the Qnorm A+R results were used in all further analyses. At some energies, the various parameters of interest were extracted using the other three sets of raw data. Disagreement with the Qnorm A+R results occurred only rarely, and no systematic effects were observed.

An example of an angular distribution and polarized angular distribution obtained for the reaction $^{12}C(\vec{p},\gamma_0)^{13}N$ is shown in Figure III-3. The ordinate of the angular distribution plot is the sum of the spin up and spin down yields. The ordinate of the polarized angular distribution plot is the asymmetry, defined as the difference of these yields divided by $2\mathscr{P}A_0$, where $\mathscr{P}$ is the magnitude of the beam polarization, and A_0 is related to the total strength of the reaction. The plus signs are the average values at each angle, the surrounding points with error bars are the actual data. The consistency of the separate measurements is seen to be very good.

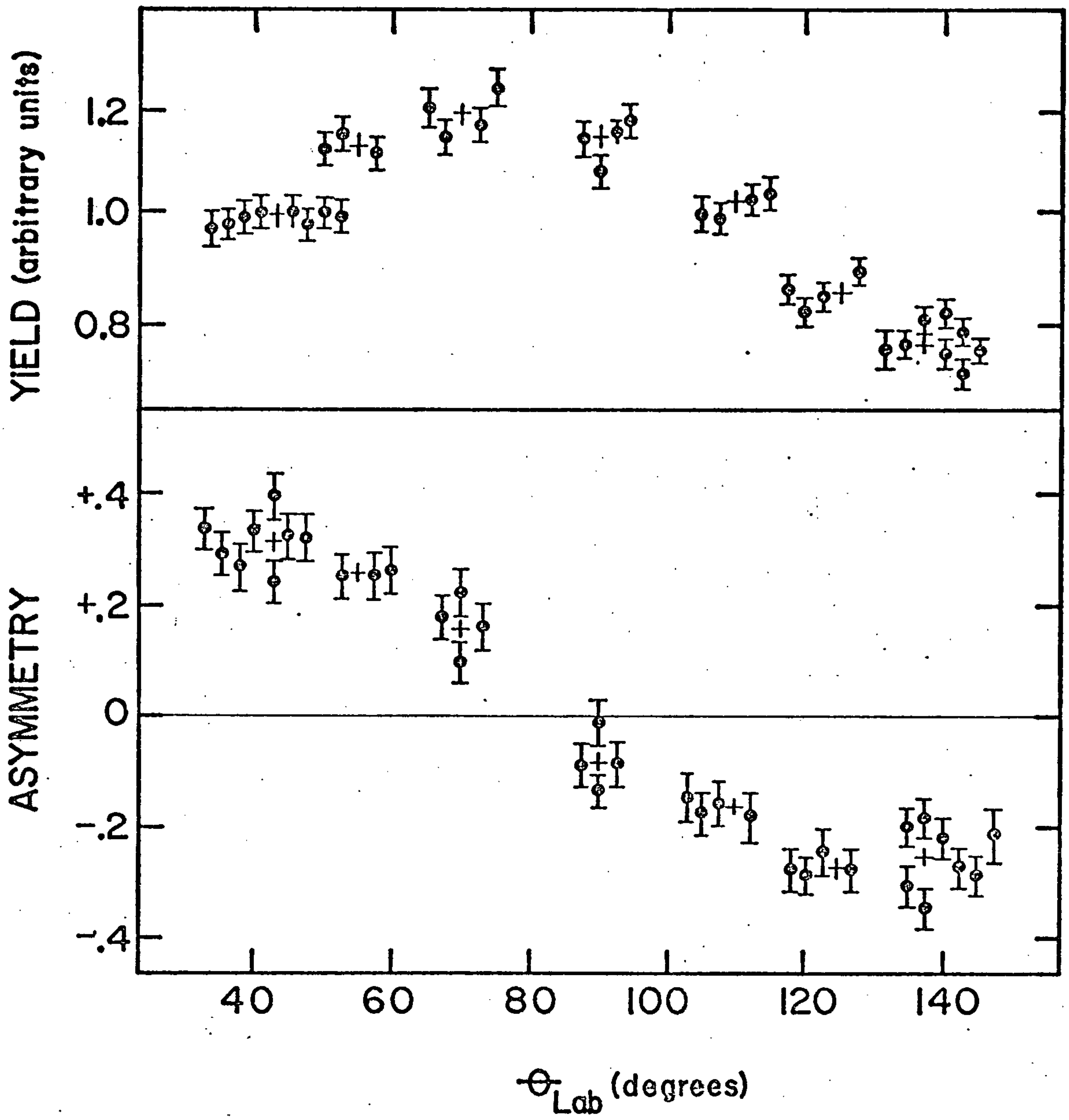

Fig. III-3 : The complete angular distribution measurements at $E_{\vec{p}}$ = 10 MeV. The ordinate of the upper plot is the sum of the spin up and spin down yields. The ordinate of the lower plot is the difference of these yields divided by $2\mathcal{P}A_0$ (see text). The plus signs are the averages of the measurements at a given angle; the surrounding points with error bars are the actual measurements at that angle.

One other interesting test of the consistency of the data was made. For every energy, the results for the yield and analyzing power at each angle were averaged and a chi-square (χ^2) for the averaging process was calculated. The data were actually averaged in pairs in the order in which they were measured for a given angle (i.e. the first two measurements at a given angle were averaged together and then the next two measurements at that angle were averaged) to increase the number of chi-square values. The resulting chi-squares for all energies and angles were then counted in 0.1 wide bins. There were a total of 128 values for both the yield and analyzing power. This procedure would be expected to yield chi-square distributions with one degree of freedom. Plotted in Figure III-4 are the resulting histograms - the solid curved lines are the expected results. There appears to be no non-statistical behaviour in the analyzing power histogram; there is possibly a small excess of points between $\chi^2 = 0.7$ and 2.1 in the yield histogram. Not shown in this figure are points with $\chi^2 > 5.0$. There were 6 of these in the yield and 5 in the analyzing power. The number of chi-square values expected to be greater than 5.0 can be found from the binomial distribution as before. The probability, p, of $\chi^2 > 5.0$ is .025 for 1 degree of freedom. Then the mean (with N = 128) is 3.2 and the standard deviation is 1.8. Thus between 1 and 5 values of chi-square are expected to be greater than 5.0. Overall then, there appears to be no strong evidence for non-statistical behaviour in any of the data.

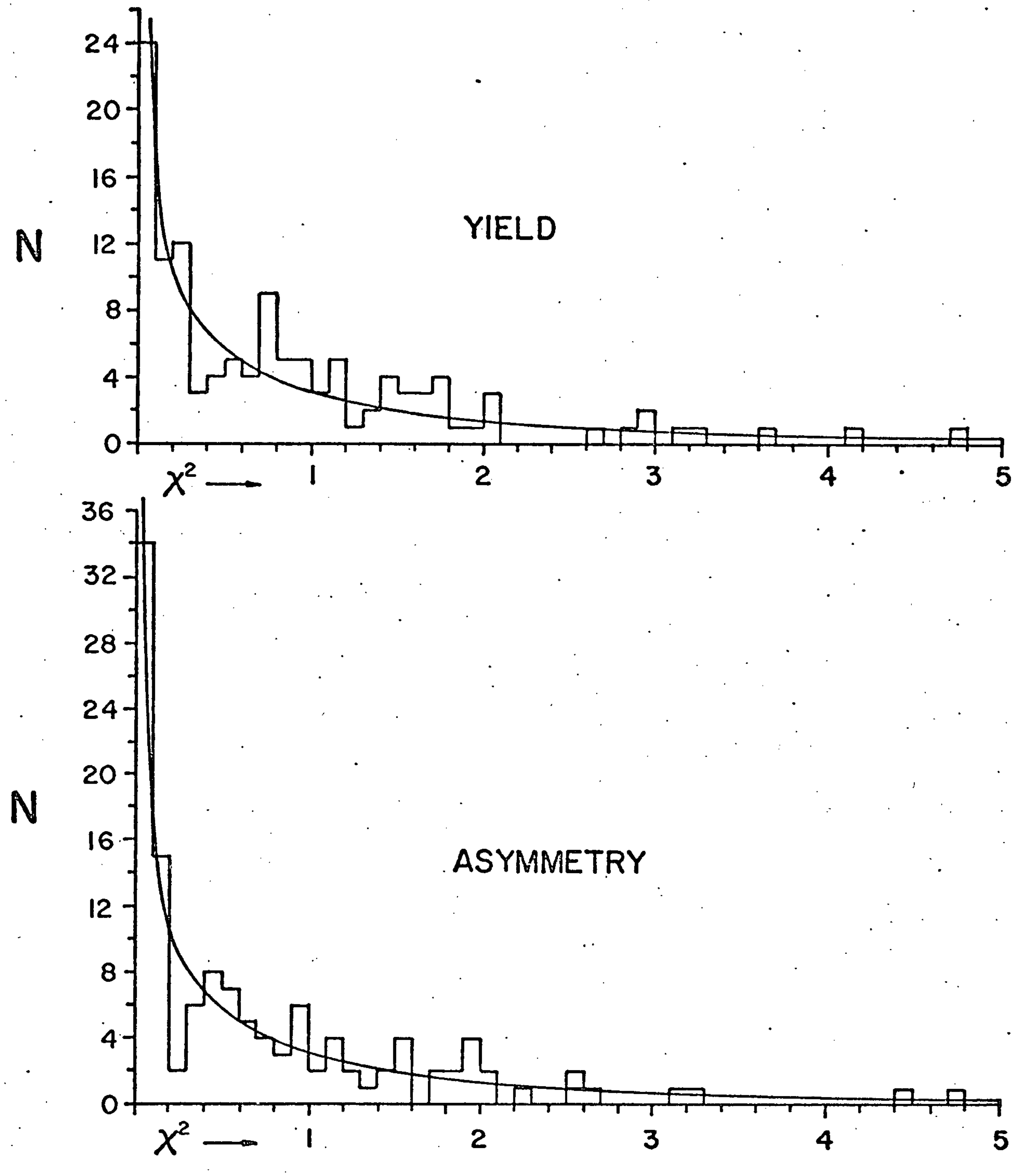

Fig. III-4 : Distribution of χ^2 for the $^{12}C(\vec{p},\gamma_0)^{13}N$ yields and asymmetries. The chi-squares were obtained by averaging the data in pairs (see text). The solid curves represent the expected χ^2-distribution for 1 degree of freedom.

3.5 Beam Polarization Measurements

The spectra obtained from the measurements using the helium polarimeter were printed out channel by channel and the final analysis was carried out by hand. The results of these measurements are shown in Table III-1 along with the polarizations as determined from the $^{12}C(\vec{p},p_o)^{12}C$ reaction. The latter values are the averages of the runs for the given energy. The analyzing powers for the ^4He measurements were taken from the data of Schwandt <u>et al</u>. (SC 71), and for the ^{12}C measurements from Meyer <u>et</u> <u>al</u>. (ME 76). No polarization results are given for the 10 MeV and 11.2 MeV $^{12}C(\vec{p},p_o)^{12}C$ data. Reference to the data of Meyer and Plattner (ME 73b) and Terrell <u>et</u> <u>al</u>. (TE 68) shows that the analyzing power for $^{12}C(\vec{p},p_o)^{12}C$ is varying rapidly at these energies, so that small deviations of the actual beam energy from the measured energy would affect the analyzing power significantly. Overall, the agreement between the two different measurements is very good. Since the helium polarimeter measurements were essentially free from uncertain backgrounds and the analyzing power is very close to 1.0 throughout the region, their average values were used in the subsequent analysis, and the polarization was assumed to be constant at each energy throughout each series of runs.

An exception to this was necessary for the 16 MeV data where, as has already been noted, a substantial change in the polarization occurred. Here the average value of the polarization, as measured for each angle throughout the run,

Table III-1

Summary of Beam Polarization Measurements

Reaction	Polarization	Comments
$^{12}C(\vec{p},p_o)^{12}C$	.460±.020	$E_{\vec{p}}$ = 13.5 MeV
$^{4}He(\vec{p},p_o)^{4}He$	.730±.017	before $E_{\vec{p}}$ = 12.0 MeV
$^{12}C(\vec{p},p_o)^{12}C$	.725±.024	$E_{\vec{p}}$ = 12.0 MeV
$^{12}C(\vec{p},p_o)^{12}C$	.730±.020	$E_{\vec{p}}$ = 14.0 MeV
$^{12}C(\vec{p},p_o)^{12}C$	.736±.018	$E_{\vec{p}}$ = 16.0 MeV
$^{4}He(\vec{p},p_o)^{4}He$	.730±.015	after $E_{\vec{p}}$ = 16.0 MeV
$^{4}He(\vec{p},p_o)^{4}He$	.721±.013	before $E_{\vec{p}}$ = 12.8 MeV
$^{12}C(\vec{p},p_o)^{12}C$	.730±.026	$E_{\vec{p}}$ = 12.8 MeV
$^{4}He(\vec{p},p_o)^{4}He$	.737±.010	after $E_{\vec{p}}$ = 12.8 MeV
$^{12}C(\vec{p},p_o)^{12}C$	.720±.015	$E_{\vec{p}}$ = 15.0 MeV
$^{12}C(\vec{p},p_o)^{12}C$	-.001±.004	$E_{\vec{p}}$ = 15.0 MeV (coils off)
$^{4}He(\vec{p},p_o)^{4}He$	.731±.008	after $E_{\vec{p}}$ = 15.0 MeV
$^{4}He(\vec{p},p_o)^{4}He$	-.001±.007	after $E_{\vec{p}}$ = 15.0 MeV (coils off)
$^{12}C(\vec{p},p_o)^{12}C$	-	$E_{\vec{p}}$ = 10.0 MeV
$^{12}C(\vec{p},p_o)^{12}C$	-	$E_{\vec{p}}$ = 11.2 MeV
$^{4}He(\vec{p},p_o)^{4}He$	.739±.013	after $E_{\vec{p}}$ = 11.2 MeV
$^{4}He(\vec{p},p_o)^{4}He$	.012±.006	after $E_{\vec{p}}$ = 11.2 MeV (coils off)
$^{12}C(\vec{p},p_o)^{12}C$	.710±.030	$E_{\vec{p}}$ = 17.0 MeV

was used.

Also shown in Table III-1 are the results of measuring the polarization with unpolarized beam. These are indentified as "coils off". The purpose of these measurements was to establish whether or not there were any indications of systematic effects contributing to the asymmetries with polarized beam. It can be seen that any deviations frcm zero are usually small and insignificant.

3.6 Angular Distribution Functions

The angular distribution of gamma radiation following the capture of unpolarized projectiles has been developed by several authors (for example, BI 60, RO 67, BL 52), and is given by

$$W_u(\theta) \sim \sum_{t,t',k} C(t,t',k)\, Re(R_t R^*_{t'})\, P_k(\cos\theta) \qquad \text{III-2}$$

where $R_t, R_{t'}$ are reduced reaction matrix elements (T-matrix elements) corresponding to different channels t,t'

$C(t,t',k)$ represents a sum over angular momentum coupling coefficients

and $P_k(\cos\theta)$ are Legendre polynomials.

The maximum value of k is given by well known theorems limiting the complexity of angular distributions.

Experimentally, the measured angular distribution can be represented by

$$W_u(\theta) \sim \sum_k A_k Q_k P_k(\cos\theta) \qquad \text{III-3}$$

where the Q_k correct for the finite size of the detector, and are given by Rose (RO 53).

Thus the experimentally determined coefficients, A_k, can be related to the T-matrix elements through the coefficients $C(t,t',k)$, as follows,

$$A_k Q_k = \sum_{t,t'} C(t,t',k)\ \mathrm{Re}(R_t R^*_{t'}) \qquad \text{III-4}$$

Methods for calculating these coefficients have been given by Sharp <u>et</u> <u>al</u>. (SH 54) among others.

It is shown in the work of Devons and Goldfarb (DE 57), following the development by Satchler (SA 55), that for the case of partially polarized spin 1/2 particles, the expression III-2 must be modified by making the replacement

$$\mathrm{Re}(R_t R^*_{t'})\ P_k(\cos\theta) \rightarrow$$

$$\mathrm{Re}(R_t R^*_{t'})\ P_k(\cos\theta) + \mathrm{Im}(R_t R^*_{t'})\ f_k(t,t')\ \vec{\mathscr{P}}\cdot\hat{n}\ P^1_k(\cos\theta)$$

Here $\vec{\mathscr{P}}$ is the incident beam polarization, $\hat{n}$ is a unit vector normal to the reaction plane (in the direction defined by the Madison Convention (BA 70)), the $P^1_k(\cos\theta)$ are associated Legendre functions, and the factor $f_k(t,t')$ is given by[1]

---

[1] Snover and Ebisawa (SN 75) have found that $f_k(t,t')$ differs by an overall sign from that given by Devons and Goldfarb.

$$f_k(t,t') = \frac{j'(j'+1) + \ell(\ell+1) - j(j+1) - \ell'(\ell'+1)}{k(k+1)} \qquad \text{III-5}$$

where j and j' are total angular momentum quantum numbers of the incident projectile corresponding to orbital angular momenta ℓ and ℓ', respectively.

Thus, equation III-2 becomes

$$W_p(\theta) \sim \sum_{t,t',k} C(t,t',k)\Big[\mathrm{Re}(R_t R^*_{t'})\ P_k(\cos\theta) + \mathrm{Im}(R_t R^*_{t'})\ f_k(t,t')\ \vec{\mathcal{P}}\cdot\hat{n}\ P^1_k(\cos\theta)\Big] \qquad \text{III-6}$$

For the case in which the proton spin is perpendicular to the reaction plane, the results of measuring the angular distribution of the gamma rays can be expressed as the sum and difference of the yields obtained with the proton spin up ($W\uparrow$) and spin down ($W\downarrow$). The sum gives the familiar unpolarized angular distribution, $W_u(\theta)$, where

$$W_u(\theta) \sim \frac{W\uparrow(\theta) + W\downarrow(\theta)}{2} = \sum_k A_k Q_k P_k(\cos\theta) \qquad \text{III-7}$$

and the difference can be expressed in terms of the analyzing power $A(\theta)$, as

$$W_u(\theta)A(\theta) \sim \frac{W\uparrow(\theta) - W\downarrow(\theta)}{2\mathcal{P}} = \sum_k B_k Q_k P^1_k(\cos\theta) \qquad \text{III-8}$$

Comparison of III-7 and III-8 to III-6 shows that the experimentally measured A_k can be related to the T-matrix elements by the angular momentum coupling coefficients C(t,t',k) as before, but now, with a polarized beam, the new experimentally determined quantities B_k can also be related to the T-matrix elements through the simple multiplicative factor $f_k(t,t')$ as follows,

$$B_k Q_k = \sum_{t,t'} C(t,t',k)\ \mathrm{Im}(R_t R^*_{t'})\ f_k(t,t') \qquad \text{III-9}$$

It is convenient to factor out A_o, which is a measure of the overall strength of the reaction, from the expressions above. Then III-7 and III-8 become

$$\frac{W{\uparrow}(\theta) + W{\downarrow}(\theta)}{2} = A_o\left[1 + \sum_k a_k Q_k P_k(\cos\theta)\right] \qquad \text{III-10}$$

$$\frac{W{\uparrow}(\theta) - W{\downarrow}(\theta)}{2\mathcal{P}} = A_o \sum_k b_k Q_k P^1_k(\cos\theta) \qquad \text{III-11}$$

Variations in a_k and b_k with energy are caused only by variations in the T-matrix elements, and not by changes in the overall strength.

The appropriate T-matrix elements are determined by noting the partial waves which take part in the reaction. For the case of spin 1/2 particles incident on a spin 0 nucleus leading to a final state with spin 1/2 and a gamma ray, as is the case here, only four partial waves can contribute, if the radiation is restricted to being only E1 and E2. By angular momentum and parity conservation, these are, in jj coupling, $s_{1/2}$ and $d_{3/2}$ capture which lead to E1 radiation and $p_{3/2}$ and $f_{5/2}$ capture which lead to E2 radiation. Thus the T-matrix elements can be labelled $se^{i\phi_s}$, $pe^{i\phi_p}$, $de^{i\phi_d}$, and $fe^{i\phi_f}$, where s and ϕ_s are the amplitude and phase for the $s_{1/2}$ partial wave, etc.

The great advantage in using polarized beams now becomes apparent. There are seven T-matrix element parameters to be determined - four amplitudes and three relative phases. If the highest multipolarity of γ-radiation is two then the maximum value of k in the summations III-7 and III-8 is four. Hence with unpolarized beam, only five coefficients can be measured experimentally, but with polarized beam, nine coefficients can be measured. Thus measurment with a polarized beam enables, in principle, the determination of all seven T-matrix elements.

The relation between the A_k and B_k coefficients and the T-matrix parameters are listed in Table III-2. The capture amplitudes have been renormalized so that the sum of the squares of the amplitudes will be equal to A_o. The relation between these reaction matrix elements and the actual reduced matrix elements $(R_t, R_{t'})$ is given in Appendix B.

It is seen from this table that A_2 is dominated by electric dipole terms, with only incoherent contributions from the much weaker quadrupole terms. The coefficient A_4 is a pure electric quadrupole term and can therefore be expected to be very small, while A_1 and A_3 result from dipole-quadrupole interference. The same considerations hold for the B_k's, although, as shown in Table III-2, these are pure interference terms (i.e., no terms such as s^2, p^2, d^2, or f^2 are present) and B_2 will not necessarily be dominated by dipole radiation if the s,d phase difference is near 0° or 180°. Thus it is seen that the dominant effect of the presence of quadrupole radiation is its interference with the dipole radiation, and the consequent appearance of Legendre and associated Legendre functions of odd degree.

Table III-2

Relation between the Angular Distribution Coefficients and the Reaction Matrix Elements *

$$A_o = s^2 + p^2 + d^2 + f^2$$

$$A_1 = 2.45spcos(\phi_s - \phi_p) - 0.35pdcos(\phi_p - \phi_d) + 2.55dfcos(\phi_d - \phi_f)$$

$$A_2 = 0.5p^2 - 0.5d^2 + 0.57f^2 + 1.41sdcos(\phi_s - \phi_d) - 0.35pfcos(\phi_p - \phi_f)$$

$$A_3 = 2.00sfcos(\phi_s - \phi_f) + 2.08pdcos(\phi_p - \phi_d) - 1.13dfcos(\phi_d - \phi_f)$$

$$A_4 = -0.57f^2 + 2.80pfcos(\phi_p - \phi_f)$$

$$B_1 = 1.22spsin(\phi_s - \phi_p) + 0.69pdsin(\phi_p - \phi_d) - 1.27dfsin(\phi_d - \phi_f)$$

$$B_2 = -0.71sdsin(\phi_s - \phi_d) + 0.29pfsin(\phi_p - \phi_f)$$

$$B_3 = -0.67sfsin(\phi_s - \phi_f) - 0.69pdsin(\phi_p - \phi_d) + 0.09dfsin(\phi_d - \phi_f)$$

$$B_4 = -0.70pfsin(\phi_p - \phi_d)$$

* The relation between the reaction matrix elements and the R_t of equation III-2 is given in Appendix B.

The solid angle correction factors Q_k are listed in Table III-3. They were calculated for the particular detector arrangement described in Chapter II using a computer program written for this purpose (LE 64).

Table III-3

Solid Angle Correction Factors

Q_o	Q_1	Q_2	Q_3	Q_4
1.000	.995	.985	.970	.950

3.7 Results of the Angular Distribution Fits

The averaged data at each energy were fit by a linear least squares technique with the angular distribution functions III-7 and III-8. This fit was performed as the first step of a two part computer analysis (BU 76a). Since the equations involved are linear in the parameters, this calculation is quite straightforward and closely follows the prescription given by Bevington (BE 69a).

The differential cross sections and fits are plotted in Figure III-5, and the asymmetries and fits are plotted in Figure III-6. The extracted coefficients and their errors are listed in Table III-4. Note that the chi-squares that are quoted have been divided by the number of degrees of freedom, ν, and are thus reduced chi-squares ($\chi^2_\nu \equiv \chi^2/\nu$). It is seen that all these fits are acceptable in the sense that the chi-squares are reasonable. The worst case for the asymmetry occurs at 13.5 MeV, where the χ^2_ν of 1.87 corresponds to a 13% confidence level for 3 degrees of freedom, which is certainly acceptable. The worst case for the yield occurs at 14 MeV; there the reduced chi-square of 4.24 corresponds to a 1.4% confidence level for 2 degrees of freedom. While this is only marginally acceptable, nothing unusual was noted in the further

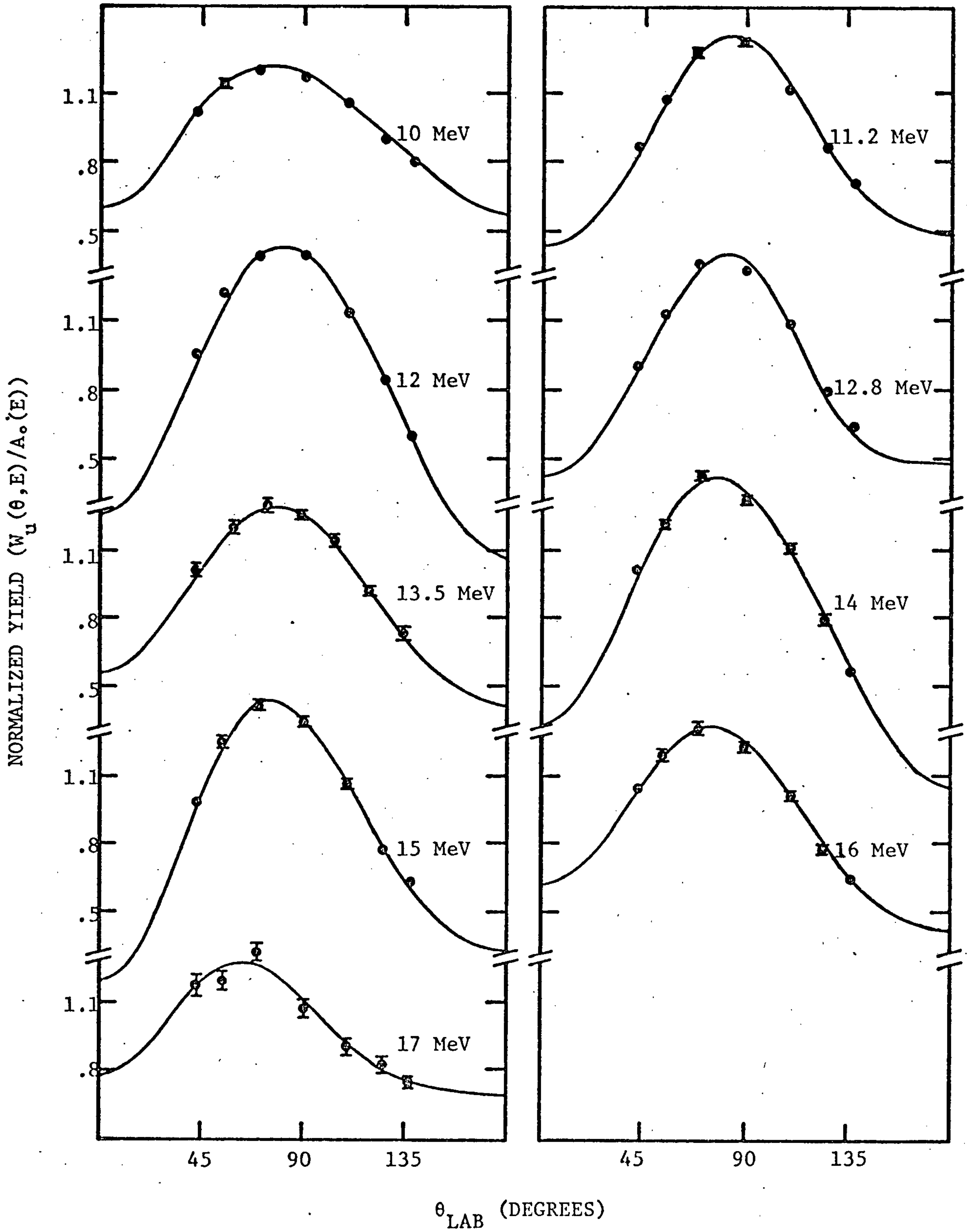

Fig. III-5 : $^{12}C(\vec{p},\gamma_0)^{13}N$ normalized differential cross sections. The solid lines are from a least squares fit to the data (see text). Statistical errors are shown where they are larger than the spot size.

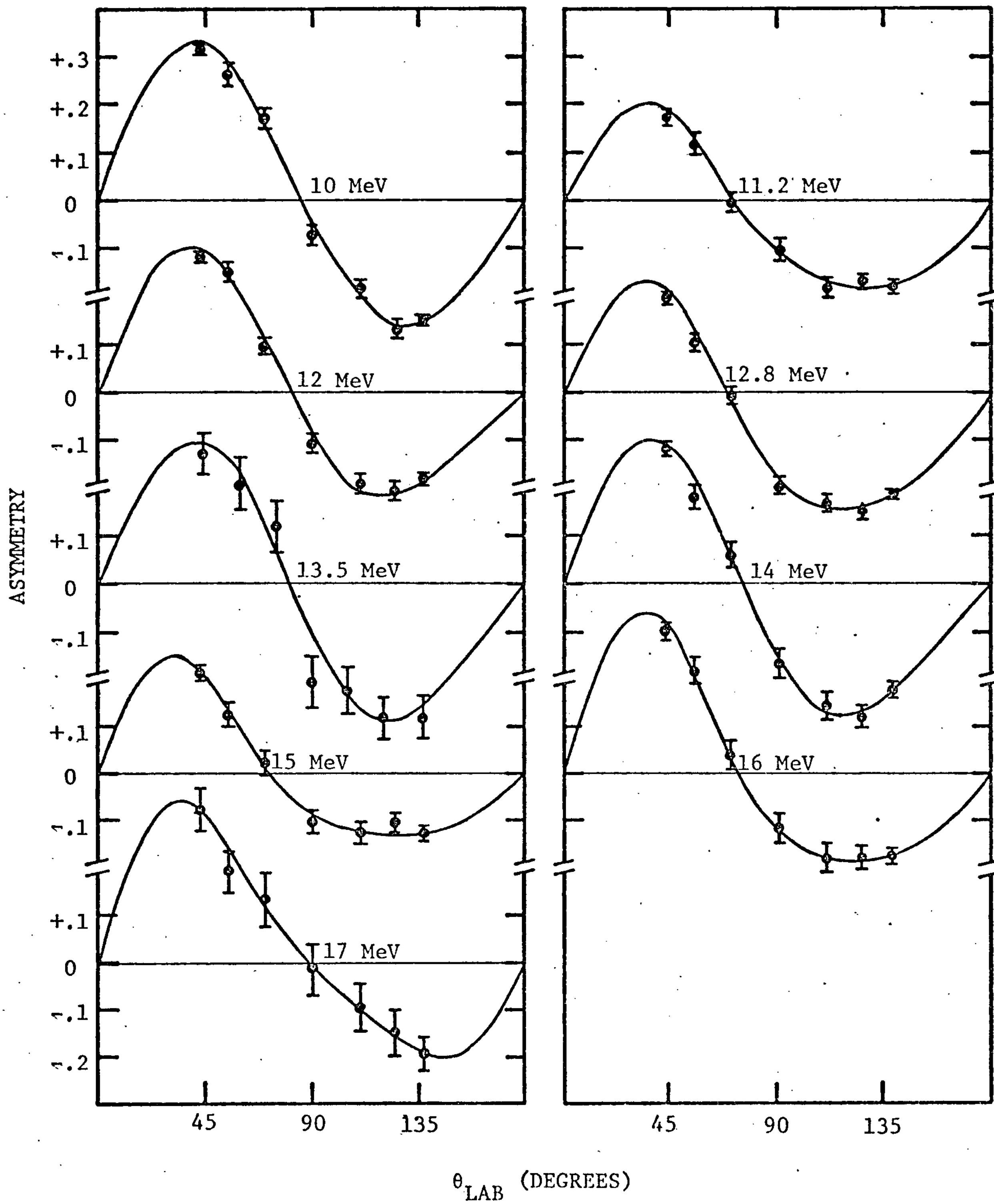

Fig. III-6 : $^{12}C(\vec{p},\gamma_0)^{13}N$ angular distributions for the asymmetries. The solid lines are least squares fits to the data (see text). Statistical errors only are shown.

Table III-4: $^{12}C(\vec{p},\gamma_o)^{13}N$ Angular Distribution Coefficients

$E_{\vec{p}}$ (MeV)	$4\pi A_o$ (μb) (c)	a_1	a_2	a_3	a_4	b_1	b_2	b_3	b_4	--- χ^2_ν --- (a)	(b)
10.0	22.0	.120	−.384	−.100	−.047	.0118	.1916	.0248	.0018	1.02	1.54
		±.012	±.039	±.028	±.045	±.0088	±.0055	±.0053	±.0064		
11.2	21.0	.086	−.620	−.114	.081	−.0711	.1125	.0267	.0124	1.02	0.49
		±.012	±.041	±.029	±.045	±.0097	±.0053	±.0058	±.0066		
12.0	24.9	.218	−.804	−.118	−.032	−.0265	.1602	.0426	−.0009	0.66	0.90
		±.011	±.038	±.024	±.041	±.0082	±.0047	±.0050	±.0056		
12.8	26.4	.147	−.641	−.186	.100	−.1140	.1358	.0418	.0096	3.58	1.15
		±.010	±.034	±.024	±.036	±.0078	±.0044	±.0047	±.0054		
13.5	22.7	.167	−.525	−.106	.104	−.0571	.1860	.0334	−.0077	1.04	1.87
		±.030	±.092	±.085	±.085	±.0224	±.0179	±.0165	±.0190		
14.0	20.8	.270	−.766	−.134	−.052	−.0871	.1713	.0498	.0011	4.24	0.51
		±.014	±.050	±.034	±.055	±.0117	±.0064	±.0069	±.0079		
15.0	17.8	.197	−.713	−.269	−.023	−.0341	.1023	.0394	.0182	1.15	0.49
		±.014	±.048	±.033	±.052	±.0109	±.0059	±.0064	±.0074		
16.0	15.7	.245	−.497	−.148	.018	−.0359	.1522	.0538	.0186	0.93	0.13
		±.017	±.055	±.033	±.062	±.0132	±.0076	±.0080	±.0092		
17.0	10.7	.253	−.230	−.212	−.045	.0275	.1551	.0251	.0272	2.89	0.24
		±.037	±.107	±.077	±.121	±.0241	±.0157	±.0157	±.0177		

(a) Reduced chi-squared for fit to yield angular distribution
(b) Reduced chi-squared for fit to asymmetry angular distribution
(c) A_o taken from Figure 6 of reference BE 76b

analysis of the 14 MeV data.

Plots of the a_k and b_k coefficients are given in Figure III-7. Also shown in this figure are the unpolarized angular distribution coefficients obtained by Berghofer _et al._ (BE 76b). Only the a_1 and a_2 coefficients are compared, because when the fits to the data of Berghofer _et al._ were extended to include a_3 and a_4 terms, the errors in a_1 and a_2 increased to such an extent that the overall agreement with the present results was obscured. The solid and dotted lines are the results of calculations with the DSD model, which will be discussed in Chapter IV.

It can be noted here that the presence of the non-zero a_3 and b_3 coefficients throughout this energy region unambiguously implies electric dipole-quadrupole interference. Both a_1 and b_1 are also seen to be non-zero. This could arise from E2 radiation, but it can also result from the presence of M1 radiation (see Appendix B). This problem is dealt with in more detail later.

3.8 Extraction of the T-matrix Elements

The capture amplitudes and phases were determined from the extracted A_k and B_k coefficients as the second step in the computer analysis. In this part of the analysis, use is made of the gradient expansion algorithm of Marquardt (MA 63) to perform a non-linear least squares fit to the equations of Table III-2. The full error matrix is retained from the first

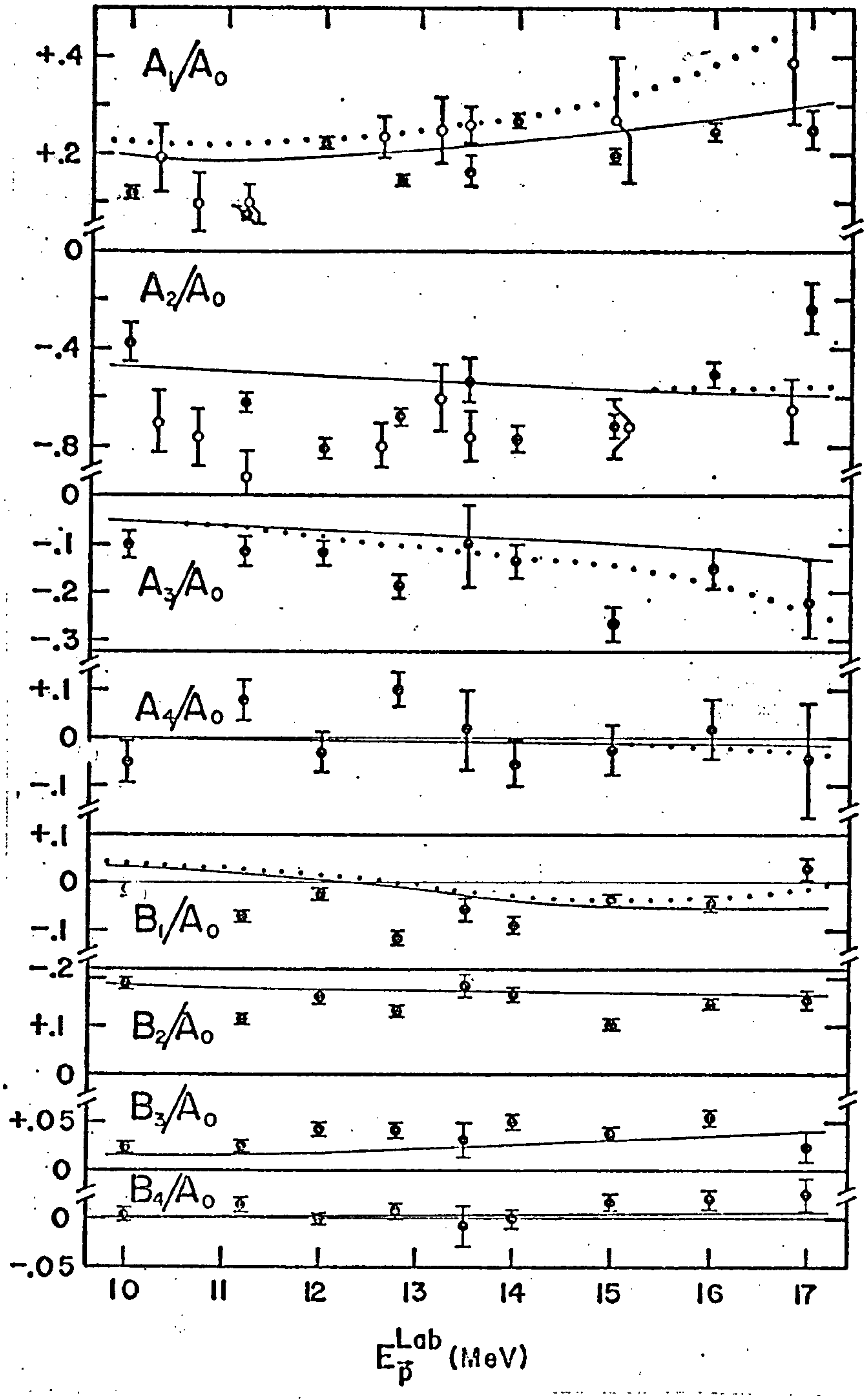

Fig. III-7 : $^{12}C(\vec{p},\gamma_0)^{13}N$ normalized angular distribution coefficients. Solid points refer to the present data; open circles refer to the data of reference (BE 76b). The solid and dotted lines are from calculations with the DSD model.

part of the analysis, including the correlation terms among all the A_k and B_k coefficients. It has been found in previous analyses that these correlations in some cases affect the values obtained for the T-matrix elements, and always affect their uncertainties (BU 76a).

Two solutions with acceptable chi-squares are found at each energy, one corresponding to dominant d-wave capture (solution I), and the other corresponding to dominant s-wave capture (solution II). The extracted reaction amplitudes and phases and associated errors for the two solutions are listed in Tables III-5 and III-6, along with the values of the reduced chi-square for each fit. Note that both solution I and solution II occur at exactly the same value of χ^2_ν; in addition, although it is not shown explicitly in these tables, both solutions occur at exactly the same value for the E2 cross section (σ_{E2}).

Most of the reduced chi-squares are clearly acceptable; the only possible exception is for the fit at 12.8 MeV where the value of 4.21 corresponds to a confidence level of 1.5% for 2 degrees of freedom.

The amplitudes and relative phase for E1 capture are plotted in Figure III-8. The solid lines in the upper part of the figure correspond to the d-wave and s-wave amplitudes, respectively, calculated with the DSD model and the solid line in the bottom part of the figure corresponds to the phase difference between the s-wave and d-wave, also calculated by the model. The calculated d-wave amplitude is seen to agree well with the d-wave amplitude from solution I. Essentially

Table III-5

T-matrix Element Fits to $^{12}C(\vec{p},\gamma_0)^{13}N$ Angular Distributions. Solution I.

$E_{\vec{p}}$ (MeV)	s	p	d	f	$\phi_p-\phi_s$	$\phi_d-\phi_s$	$\phi_f-\phi_s$	χ^2_ν
10.0	.292 ±.008	.040 ±.015	.9546 ±.0035	.041 ±.006	−66° ±17°	74.5° ±2.2°	65° ±12°	0.54
11.2	.240 ±.013	.072 ±.022	.9666 ±.0048	.056 ±.010	−28° ± 9°	134.7° ±2.8°	54° ±12°	2.85
12.0	.369 ±.016	.058 ±.012	.9236 ±.0078	.087 ±.016	68° ±25°	138.2° ±1.8°	157° ± 9°	0.87
12.8	.321 ±.015	.129 ±.023	.9322 ±.0087	.106 ±.012	−31° ± 4°	137.5° ±2.0°	51° ± 7°	4.21
13.5	.292 ±.028	.042 ±.038	.9533 ±.0108	.068 ±.025	−35° ±46°	103.8° ±5.0°	68° ±24°	0.17
14.0	.344 ±.017	.030 ±.014	.9314 ±.0071	.116 ±.015	41° ±59°	131.2° ±2.6°	106° ± 9°	0.43
15.0	.238 ±.015	.115 ±.024	.9635 ±.0057	.041 ±.031	16° ± 7°	140.0° ±3.0°	125° ±17°	2.69
16.0	.232 ±.012	.066 ±.016	.9671 ±.0046	.081 ±.012	−12° ±20°	101.2° ±4.3°	101° ±10°	1.61
17.0	.282 ±.026	.067 ±.042	.9514 ±.0104	.104 ±.017	−117° ±21°	53.6° ±6.0°	59° ±12°	1.31

all theoretical models predict that the dominant transition in the GDR will be the one in which the orbital angular momentum of the absorbing particle is increased by one unit and there is no spin flip (WI 56). In the present case, this corresponds to

Table III-6

T-matrix Element Fits to $^{12}C(\vec{p},\gamma_0)^{13}N$ Angular Distributions. Solution II.

$E_{\vec{p}}$ (MeV)	s	p	d	f	$\phi_p-\phi_s$	$\phi_d-\phi_s$	$\phi_f-\phi_s$	χ^2_ν
10.0	.931 ±.004	.035 ±.008	.361 ±.009	.045 ±.014	13° ±16°	126.8° ±1.6°	142° ±14°	0.54
11.2	.857 ±.009	.059 ±.010	.507 ±.013	.070 ±.019	91° ±15°	157.7° ±1.0°	168° ±10°	2.85
12.0	.783 ±.013	.085 ±.020	.612 ±.015	.061 ±.014	-17° ± 8°	151.8° ±0.8°	88° ±21°	0.87
12.8	.803 ±.013	.111 ±.013	.572 ±.014	.125 ±.021	95° ± 9°	153.9° ±0.8°	173° ± 5°	4.21
13.5	.881 ±.017	.065 ±.024	.467 ±.026	.046 ±.034	37° ±27°	139.0° ±3.3°	150° ±45°	0.17
14.0	.807 ±.013	.117 ±.018	.578 ±.017	.029 ±.022	22° ±10°	148.9° ±1.2°	132° ±44°	0.43
15.0	.849 ±.010	.027 ±.012	.514 ±.015	.119 ±.021	44° ±36°	160.3° ±1.1°	155° ± 7°	2.69
16.0	.900 ±.008	.075 ±.015	.423 ±.015	.072 ±.017	43° ±10°	144.7° ±1.8°	121° ±16°	1.61
17.0	.956 ±.011	.089 ±.024	.267 ±.025	.086 ±.039	-9° ±13°	122.1° ±6.5°	167° ±16°	1.31

dominant d-wave capture, and so agrees with solution I. Therefore, most of the future discussion will be based on this solution.

The relative phase $\phi_d-\phi_s$ shows some very interesting

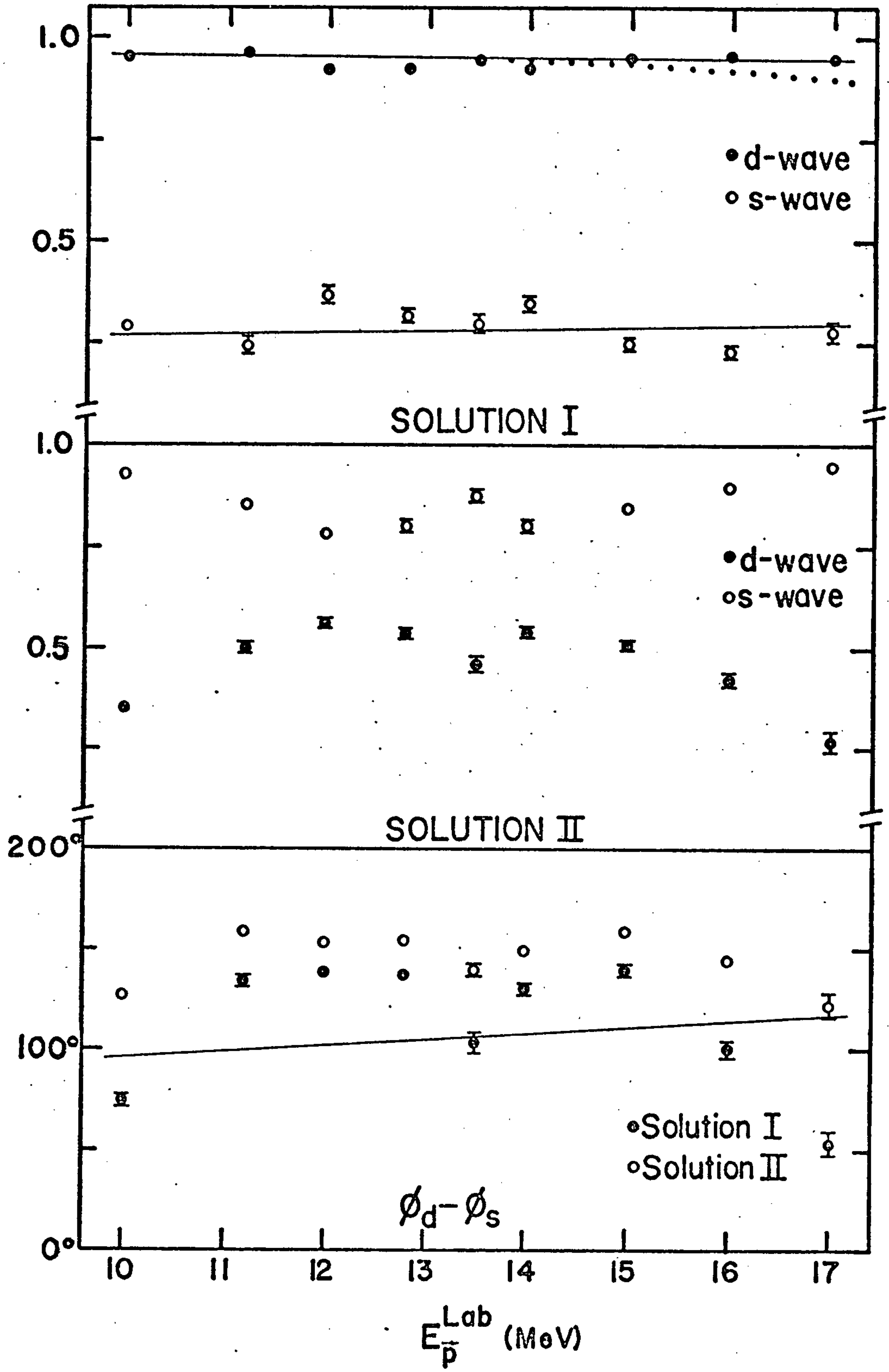

Fig. III-8 : E1 amplitudes and relative phase. Errors are shown where they are larger than the point size. The solid and dotted curves represent calculations with the DSD model (Chapter IV).

structure. There appears to be a broad overall resonance to this phase difference, and a substantial dip near 13.5 MeV. The relative change in the phase possibly indicates that only one of the reaction amplitudes participates in the pygmy resonance. The dip might result from interference between the pygmy and some level near 13.5 MeV. The nearest candidate is the level observed by Hasinoff et al. (HA 72) at E_x = 14.04 MeV in ^{13}N ($E_{\vec{p}}$ = 13.12 MeV) with a width of ∿170 keV. It would be necessary to measure in finer energy steps to clarify this point.

Parameters associated with the E2 reaction matrix elements for solution I are listed in Table III-7, and are plotted in Figure III-9 along with the results of the DSD calculation. The approximate constancy of the p,d phase difference is very interesting in that it implies that it is the s-wave phase that is resonating, unless the p-wave and d-wave phases happen to both be undergoing the same phase changes, which would be very surprising. There appears to be some fluctuations in the f,d phase difference between $E_{\vec{p}}$ = 10 MeV and 14 MeV. Here again it would interesting to measure in finer steps to investigate this structure more fully.

The errors quoted for all of the parameters extracted from the data are statistical errors only, and do not include such possible errors as beam shifts on the target or errors in the charge collection and beam polarization measurements. It has already been shown that the data is self-consistent without including errors from these sources. The effect of varying the polarization by 2% caused about a 4% change in the B_k

Table III-7

E1 Amplitude Ratio s/d and Parameters Related to E2 Capture for Solution I

$E_{\vec{p}}$ (MeV)	s/d	p/f	$\phi_p-\phi_f$	$\phi_f-\phi_d$	$\phi_p-\phi_d$	$\frac{\sigma_{E2}}{\sigma_{E1}+\sigma_{E2}}$
10.0	.306 ±.010	.99 ±.49	−131° ±13°	− 9° ±12°	−140° ±17°	.00328 ±.00081
11.2	.248 ±.014	1.28 ±.41	− 82° ±11°	−81° ±12°	−163° ± 9°	.0083 ±.0035
12.0	.399 ±.020	.67 ±.15	− 97° ±25°	19° ± 8°	− 78° ±25°	.0109 ±.0037
12.8	.344 ±.020	1.22 ±.20	− 82° ± 7°	−87° ± 8°	−169° ± 5°	.0279 ±.0076
13.5	.306 ±.033	.61 ±.73	−103° ±29°	−36° ±24°	−139° ±47°	.0063 ±.0025
14.0	.369 ±.021	.26 ±.14	− 65° ±52°	−25° ± 9°	− 90° ±59°	.0144 ±.0030
15.0	.247 ±.017	2.8 ±1.4	−142° ±13°	−15° ±17°	−157° ± 7°	.0149 ±.0045
16.0	.240 ±.013	.81 ±.30	−114° ±17°	0° ± 9°	−114° ±20°	.0109 ±.0012
17.0	.296 ±.030	.64 ±.50	−176° ±21°	5° ±11°	−171° ±20°	.0153 ±.0036

coefficients, but this usually resulted in a change of less than 1% in the values of the T-matrix elements.

Because the equations of Table III-2 are non-linear, there is no guarantee that additional solutions do not exist. An

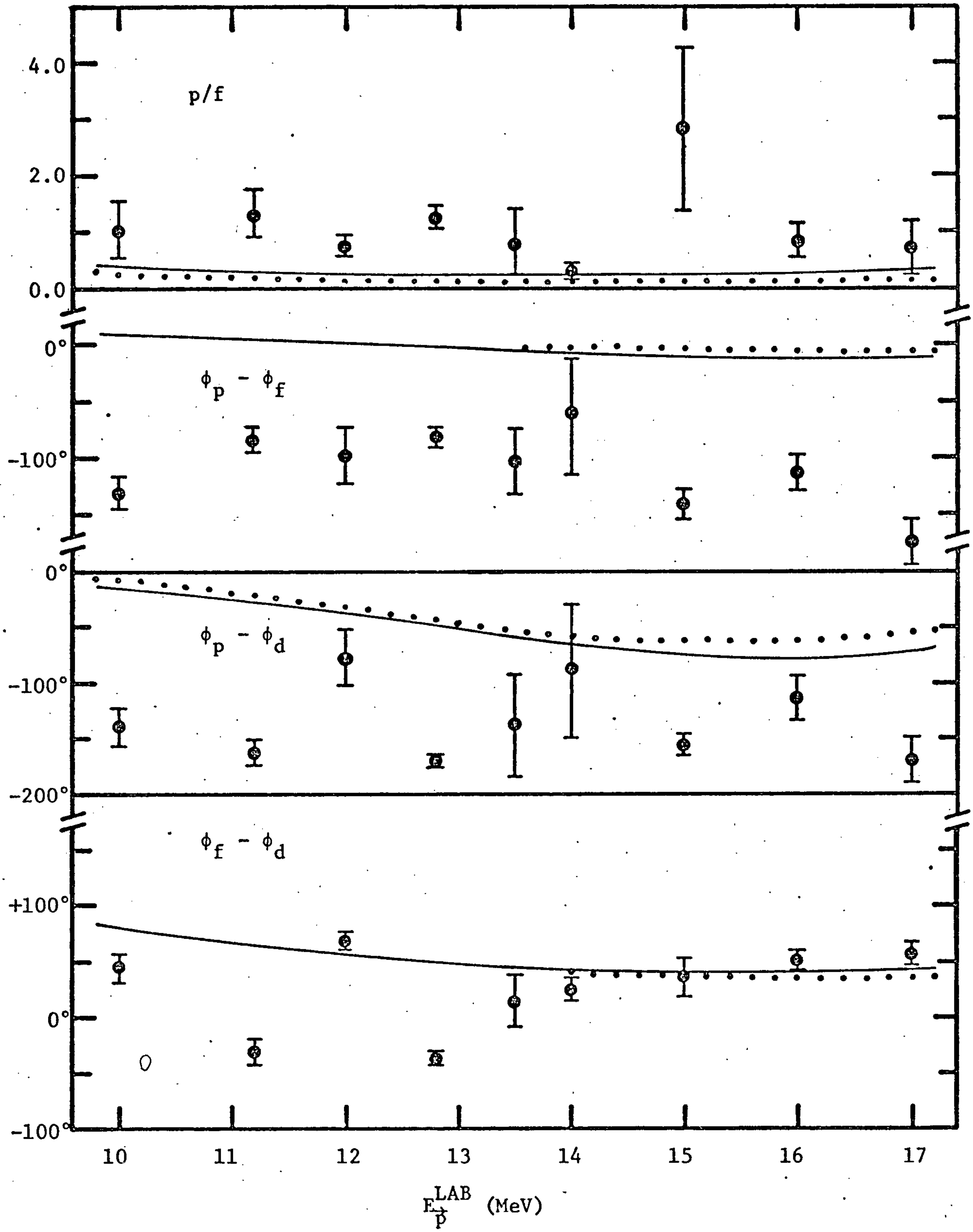

Fig. III-9 : The amplitude ratio and phases related to E2 capture. The solid and dotted curves represent calculations with the DSD model (Chapter IV).

attempt to locate at least some of these other solutions was made in the following way. First, σ_{E2} was fixed at some arbitrary value expressed as a fraction of the total cross section, and all the other parameters were allowed to vary to minimize χ^2. Then σ_{E2} was stepped to a new value and the process was repeated, with the starting guesses for the parameters at each successive step being the values obtained in the previous step. In this way, the projection of the multi-dimensional χ^2-surface was cast onto the E2 strength axis. The results of this search are plotted in Figure III-10. These results were obtained with solution I as the starting point. The first, and deepest, minimum is in each case the doubly degenerate solution corresponding to solutions I and II described previously. The second minimum in each case appears to correspond to a solution which has a different value of the s/d ratio than is obtained for the solutions at the first minimum. A typical value of s/d for solution I is 0.3, while a typical value for the second solution is 0.7. The parameters that are obtained at the second minima are listed in Table III-8.

At some, but not all, energies, the second solution was also found to be doubly degenerate. These other second solutions, where they appeared, were found to belong to the family that begins with solution II. No exhaustive search was made to find them all.

Several of the second solutions can be excluded on statistical grounds. Shown in Figure III-10 is the 1% confidence limit for each fit (χ^2 = 9.2). All of the solutions

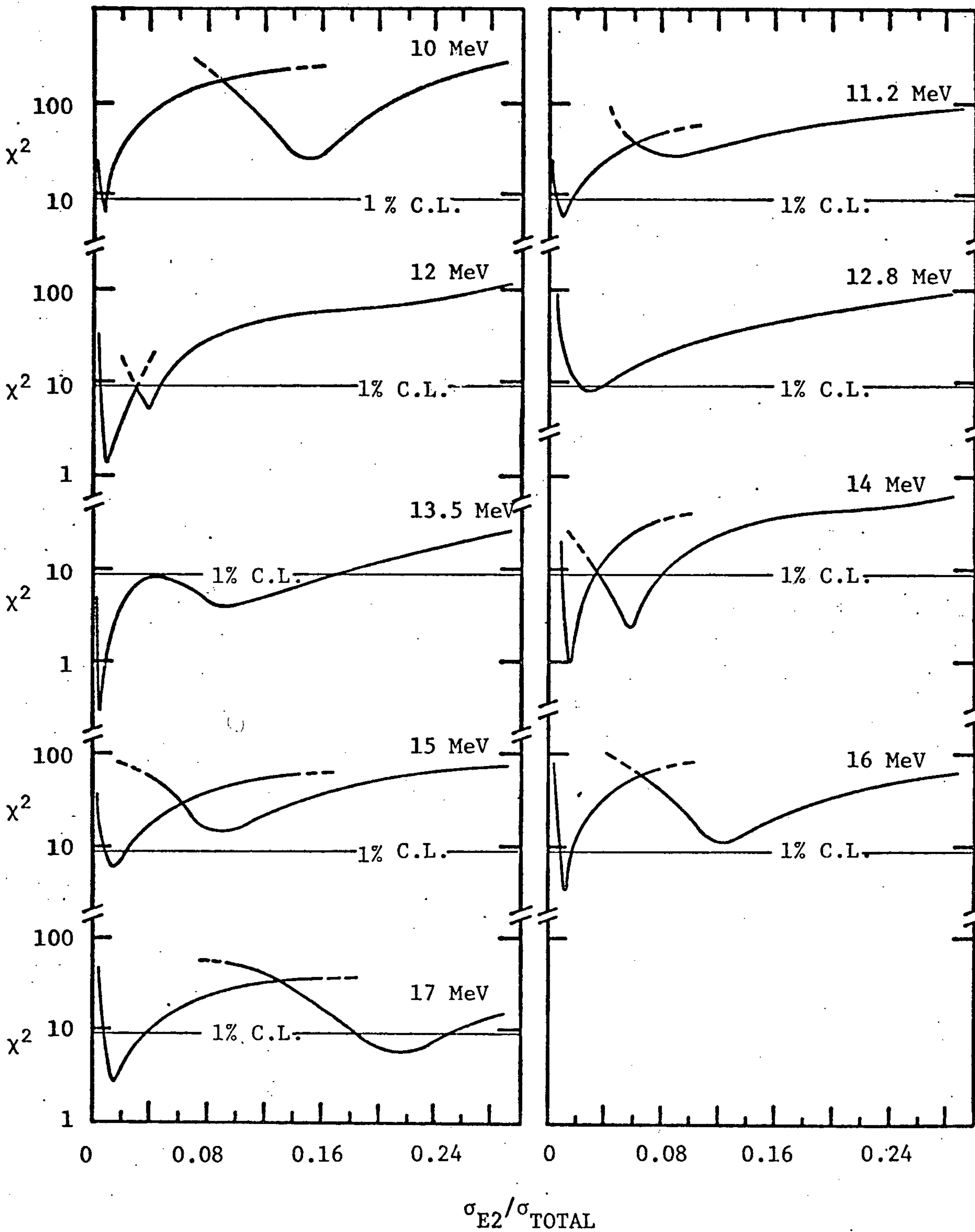

Fig. III-10 : Projection of the multidimensional χ^2-surface onto the E2 strength axis.

Table III-8

Second Solutions to the T-matrix Element Fits

$E_{\vec{p}}$ (MeV)	s/d	p/f	$\phi_d-\phi_s$	$\phi_p-\phi_f$	$\phi_f-\phi_d$	$\phi_p-\phi_d$	$\frac{\sigma_{E2}}{\sigma_{E1}+\sigma_{E2}}$	χ^2
10.0	.790 ±.022	.733 ±.026	135.8° ±1.4°	-179° ± 7°	-67.6° ± 2.6°	113° ± 5°	.1509 ±.0053	24.7
11.2	.647 ±.029	.719 ±.068	154.7° ±1.3°	-133° ±13°	-91.1° ± 5.1°	136° ± 8°	.0849 ±.0080	25.5
12.0	.642 ±.035	1.11 ±.16	148.2° ±1.2°	-167° ±21°	72.8° ± 9.4°	-95° ±12°	.0402 ±.0049	5.22
12.8*								
13.5	.710 ±.089	.560 ±.059	140.4° ±4.8°	-202° ±38°	-59.1° ±10.5°	99° ±27°	.0932 ±.0194	3.79
14.0	.659 ±.038	.391 ±.084	145.7° ±1.5°	-186° ±32°	-56.2° ± 7.2°	118° ±25°	.0562 ±.0071	2.43
15.0	.767 ±.034	.806 ±.088	158.8° ±1.3°	-143° ±13°	-80.0° ± 5.7°	137° ± 8°	.0902 ±.0078	13.3
16.0	.833 ±.040	.727 ±.072	146.1° ±1.8°	-146° ±12°	-75.7° ± 4.9°	138° ± 8°	.1234 ±.0089	11.6
17.0	.787 ±.063	.941 ±.102	136.5° ±4.8°	-151° ±14°	-72.9° ± 5.5°	137° ± 9°	.2165 ±.0172	5.97

* No second solution could be found at 12.8 MeV (see text).

at the lowest value of σ_{E2} fall below this limit, but of the second solutions, only those at 12 MeV, 13.5 MeV, 14 MeV, and 17 MeV fall below the limit. Reference to Table III-8 shows that the second solutions at 15 MeV and 16 MeV can only just be excluded on this basis.

No second solution could be found for the data at 12.8 MeV. Searches starting from many different parameter sets were made, but they always resulted in convergence either to solution I or to solution II.

A few other solutions were found which also had E2 cross sections that were larger than the solution I values. The minima of chi-square for these additional solutions always lay at unacceptably high levels.

The extraction of all the solutions described thus far are subject to the condition that there is no M1 radiation involved in the reaction. It was pointed out by Hanna *et al.* (HA 74a) that a consistency check on this condition can be made by excluding A_1 and B_1 from the analysis. These coefficients are the most sensitive to the presence of M1 radiation (see Appendix B). Using the T-matrix elements resulting from such an analysis, the A_1 and B_1 coefficients can be calculated and compared to the experimental values. In their analysis of the $^{15}N(\vec{p},\gamma_0)^{16}O$ reaction, Hanna *et al.* found that these coefficients were satisfactorily reproduced from an analysis which excluded them.

The results of such an analysis for the present data are plotted in Figure III-11. It is seen that the calculated coefficients do not agree with the experimental coefficients if only the experimental errors are taken into account. If the errors in the calculated coefficients are also taken into account, then the agreement is much more satisfactory. Several of the points lie more than two combined standard deviations apart, however, and this could be taken to be an indication that there is some M1 radiation underlying the structure in this region.

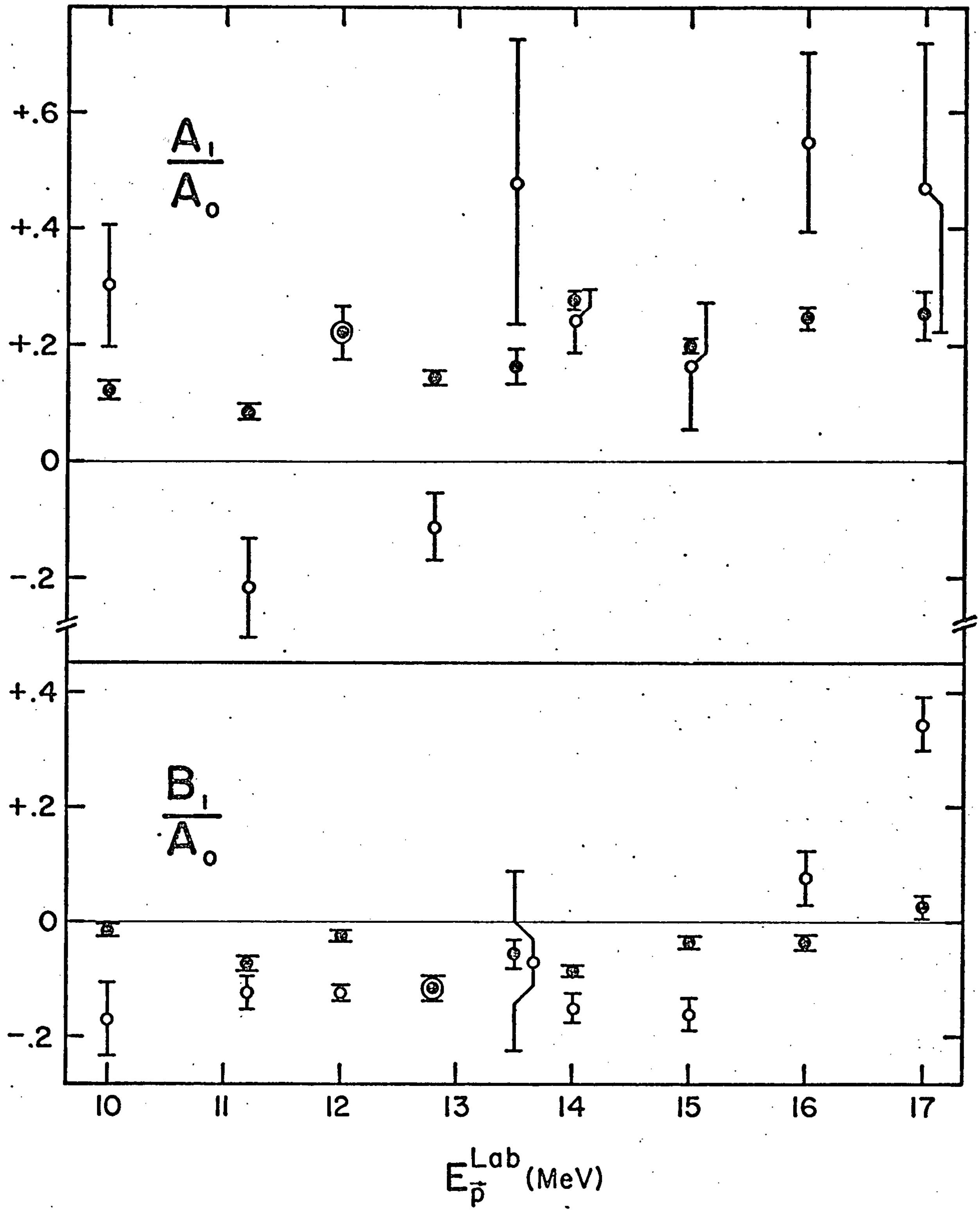

Fig. III-11 : The normalized A_1 and B_1 angular distribution coefficients. Solid points correspond to angular distribution fits to the experimental data; open circles correspond to A_1 and B_1 coefficients generated from a T-matrix element fit to the other seven A_k and B_k coefficients.

Two of these offending points lie at incident proton energies of 11.2 MeV and 12.8 MeV, which are near the interference dips in the 90° yield curve observed by Measday <u>et al</u>. (ME 73a). It seems to be fairly well established that the upper of these dips is caused by a $3/2^+$ level interfering with the broad pygmy resonance. There are still some ambiguities about the lower dip, however, and there has been some indication of M1 strength in this region. Fleming <u>et al</u>. (FL 68) observed levels in ^{13}N at excitation energies of 10.78 and 11.88 MeV. The decay of the mirror level in ^{13}C corresponding to the 11.88 MeV level has been observed to be consistent with M1 radiation in an inelastic scattering experiment (WI 69). In the present experiment, this level would be excited at an incident proton energy of 10.76 MeV. The width of this level is 130 keV (AJ 70), and its spin-parity assignment is $3/2^-$ (HS 71). If this level indeed decays by M1 radiation, the large discrepancy observed at $E_{\vec{p}} = 11.2$ MeV between the experimental A_1 coefficient and the A_1 coefficient reproduced from the analysis in which it was excluded could possibly be explained.

The decay of the 10.78 MeV level is also consistent with M1 (or possibly E2) radiation (WI 69). This level would be excited at an incident proton energy of 9.58 MeV in the present experiment.

The dominant M1 strength in this region occurs in the decay of the first T = 3/2 state in ^{13}N at $E_x = 15.07$ MeV (DI 68). However, this state is very narrow, so its effects should not be felt more than a few tens of kilovolts on either side of the resonance energy ($E_{\vec{p}}$ = 14.23 MeV).

Of course, it is also possible that more solutions exist for the analysis with A_1 and B_1 excluded. Only at one energy was a second solution found, however, although several different starting guesses were used at each energy.

There are three problems with the analysis in which A_1 and B_1 are excluded. The first is that the minima in χ^2-space are very narrow so the solutions are difficult to find, which leads to the problem just mentioned. The second is that because seven T-matrix elements are being fitted to seven experimental quantities, there are 0 degrees of freedom in the fit, so χ^2 must in fact vanish at the solution. Thus it is not possible to judge whether a solution is acceptable based on a chi-square criterion. Finally, exclusion of A_1 and B_1 puts the onus of providing evidence for the existence of E2 strength more on the other coefficients. Consequently, the errors on the extracted E2 cross sections are much larger than when A_1 and B_1 are included in the analysis.

3.9 Determination of the Cross Sections

It is seen from the above discussion that it is possible to obtain at least three solutions to the parameter of central interest - the E2 cross section. The results are plotted in Figure III-12. The energies at which there are two statistically acceptable solutions (at a 1% confidence limit)

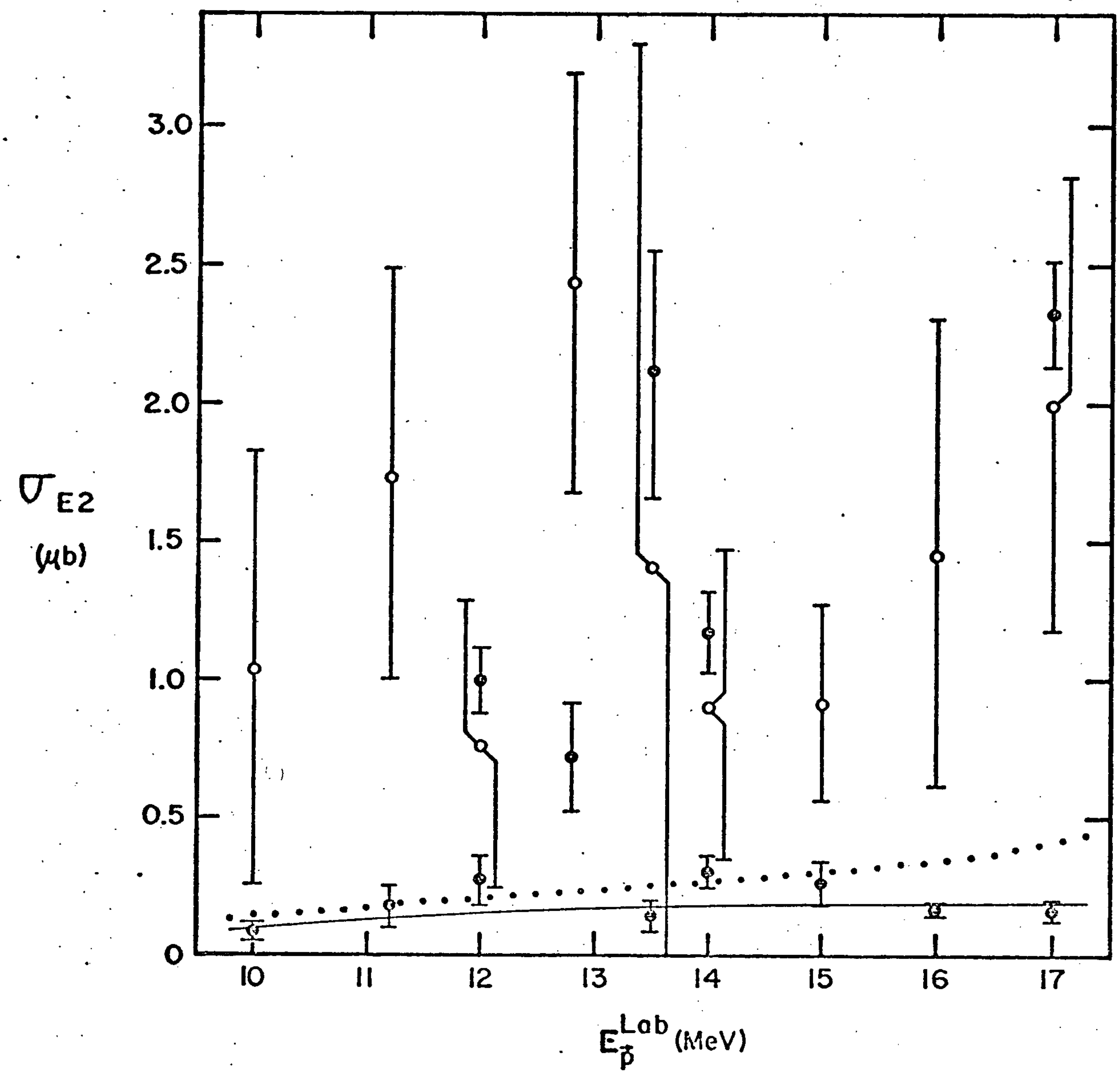

Fig. III-12 : The E2 cross sections. The solid points are from solution I (or II) and additional solutions which satisfy a 1.0 % confidence limit (see text). Open circles are from solutions obtained with A_1 and B_1 excluded from the T-matrix element fit. The solid and dotted curves are from a DSD capture model calculation (Chapter IV).

when all the coefficients are included in the analysis are indicated by two solid points at that energy on the graph. The open points correspond to solutions obtained with A_1 and B_1 excluded from the analysis. The values of σ_{E2} were calculated by comparing the fraction of E2 strength found in the present analysis to the total cross section results of Berghofer <u>et al.</u> (BE 76b). The errors shown do not include the overall ±20% normalization error from their analysis. (Because of time constraints, it was not possible to measure the efficiency of the detector; i.e. the ratio of the number of events recorded in the analysis window to the total number of events initiated in the detector by γ-rays from the $^{12}C(\vec{p},\gamma_0)^{13}N$ reaction. Therefore, the E2 cross sections could not be determined solely from the present analysis). The solid and dotted curves are results from a DSD calculation and will be discussed further in the next chapter.

It is seen that both the second solutions, where they are acceptable, and the solutions obtained with A_1 and B_1 excluded from the analysis lie at higher values of σ_{E2} and have larger errors than the solutions found at the "low" (solution I) values of σ_{E2}. The "high" values (the second solutions) of σ_{E2} from the analysis with A_1 and B_1 included also fluctuate more than the "low" values. The latter result possibly indicates that the "low" values are the correct ones, because the observed smooth variation of the a_k and b_k coefficients (see Figure III-7) would follow naturally from a smooth variation of σ_{E2}, but would be surprising if σ_{E2} showed a rapidly varying energy dependence.

It is difficult to know what to make of the fact that the σ_{E2} lie at systematically higher values when A_1 and B_1 are excluded than when they are included. Some of the problems associated with the analysis when they are excluded have been discussed in reference to the reproducibility of these coefficients. It should also be noted that satisfactory fits are obtained under the assumption that there is no M1 radiation present. Unfortunately, the only way to ascertain unambiguously if M1 radiation is present is to measure the plane polarization of the outgoing photon produced by a reaction initiated by a polarized proton (BU 75b). Such a measurement is not currently experimentally possible.

Chapter IV

THE DSD MODEL, SUM RULES AND COMPARISON WITH OTHER EXPERIMENTS

The desirability of having reaction models available with which to compare experimental data was mentioned in Chapter I. This is especially true in (p,γ) reaction studies of E2 strength where, even with polarized beams, there is not usually enough information available to separate the E1 and E2 components. Moreover, proton radiative capture reactions are particularly sensitive to the presence of direct E2 components (HA 73b), so in cases where it is desirable to learn about the collective E2 components (for example, to better understand effective charges) it is necessary to have a model available with which comparisons of quantities extracted from the data can be made, since the experiment itself cannot distinguish between these two components. Thus the purpose of a reaction model in the particular case of (p,γ) reactions is to predict what effects the presence of direct and/or collective E2 strength will have on the experimentally measured quantities. Then a comparison of the predictions with the actual experimental observations will give information on the extent to which the assumptions about the E2 strength are justified. Following the work of Potokar and others (PO 73 and references therein), Snover and Ebisawa (SN 75) have recently extended the direct semi-direct capture model to include direct and collective E2. The model will be described briefly, and comparisons of the model predictions to the present data will be made.

This chapter also contains comparisons of the present results to the isoscalar EWSR, and to the results of other, similar experiments.

4.1 The DSD Model

Lane and Lynn (LA 59) considered a direct capture model to explain the observation of Cohen (CO 55) that the cross sections for (p,γ) reactions in the energy range from 8 MeV to 22 MeV were approximately constant. These cross sections were expected to be falling rapidly as a function of energy if the compound nucleus model of Bohr (BO 36) was valid. Lane and Lynn considered the case where the incoming proton radiated energy and was captured directly into a bound state before a compound nucleus was formed. The process was considered to be mainly extra-nuclear, so that the details of the nuclear interior were relatively unimportant. Although this model gave cross sections that were in order of magnitude agreement with experiment, they were still too small by a factor of about four.

Brown (BR 64) extended this model to include the case where the incoming proton excited the target nucleus into its giant (dipole) resonance state and the proton was then scattered into a bound state. The excited core of the nucleus plus bound proton system then de-excited from the collective GDR state by emitting a gamma ray. Brown termed this process "semi-direct" to distinguish it from the one step direct process considered by Lane and Lynn. The two processes are pictured schematically in Figure IV-1.

Other workers have considered the effects of a semi-direct amplitude in nucleon capture reactions. Clement, Lane and Rook (CL 65), in a treatment only slightly different from Brown's, showed that the inclusion of the semi-direct process improved the agreement between the calculated and measured cross section for the reaction $^{142}Ce(p,\gamma)^{143}Pr$ from 10 MeV to 50 MeV. Longo and Saporetti (LO 68) included the interference term between the direct and semi-direct parts and found further improvement in the calculated cross section for this experiment. In a subsequent paper, Longo and Saporetti (LO 69) showed that inclusion of a direct E2 amplitude was important for energies above 20 MeV. More recent studies with the model have investigated different approaches to handling the description of the collective excitation (ZI 70, PO 73).

Snover and Ebisawa have extended the DSD model to include direct and collective E2 amplitudes. Because of the new details being measured in (p,γ) reactions, they calculate, in addition to the cross section, the angular distributions of the cross section and of the analyzing power. In order for a reaction model to be considered successful, it should be able to describe satisfactorily all of these experimentally measurable quantities. An outline of the model follows.

The differential cross section for a process undergoing a

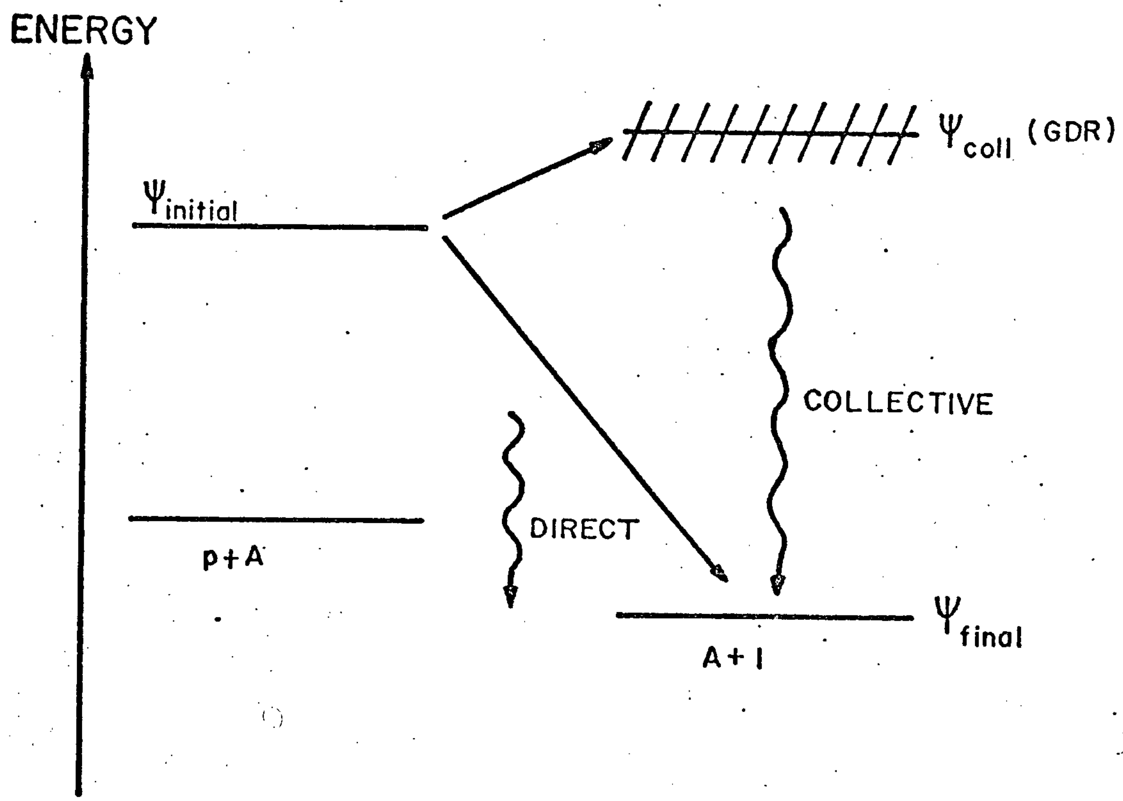

Fig. IV-1 : Schematic representation of direct and semi-direct processes. The initial p + A scattering system can proceed directly to the final bound A + 1 state with the emission of a gamma ray, or it can first excite the GDR of the core before the proton is captured into a bound state. The core + bound proton system then de-excites by the emission of a gamma ray.

transition from an initial state i to a final state f is given by (ME 65b)

$$\frac{d\sigma_{i\to f}}{d\Omega} = \frac{2\pi}{\hbar v}\left|\langle\phi_f|\hat{\varepsilon}|\phi_i\rangle\right|^2 \rho(E) \qquad \text{IV-1}$$

In this expression, ϕ_i and ϕ_f are the initial and final state wave functions, respectively, v is the incident particle velocity, $\rho(E)$ is the density of final states and $\hat{\varepsilon}$ is the appropriate electric multipole operator. Thus calculation of the differential cross section reduces to calculating matrix elements of the form

$$M_{i\to f} = \langle\phi_f|\hat{\varepsilon}|\phi_i\rangle \qquad \text{IV-2}$$

Now the Hamiltonian for the interaction of the incident nucleon with the target nucleus can be written as (BR 59b)

$$H = H_\xi + T(r) + V(\vec{r},\vec{\xi}) \qquad \text{IV-3}$$

where H is the Hamiltonian for the A nuclear particles

T(r) is the kinetic energy of the incident projectile

and $V(\vec{r},\vec{\xi})$ is the sum of the interaction potentials between the incident nucleon at location $\vec{r}$ and each of the target particles, whose location in totality is represented by $\vec{\xi}$.

A solution to the Schroedinger equation is given by $\Phi(\vec{r},\vec{\xi})$, where

$$H\Phi(\vec{r},\vec{\xi}) = E\Phi(\vec{r},\vec{\xi}) \qquad \text{IV-4}$$

and the wave function Ψ satisfies

$$H_o \Psi(\vec{r},\vec{\xi}) \equiv E\Psi(\vec{r},\vec{\xi}) \qquad \text{IV-5}$$

where $H_o = H_\xi + T(r)$.

The potential V is too complicated to permit an exact solution to IV-4, so the complex optical model potential V_{opt} is introduced, where

$$V = V_{opt} + \delta V \qquad \text{IV-6}$$

and δV, the residual particle-hole interaction, is treated as a perturbation. It was consideration of the interaction δV that enabled Brown and Bosterli (BR 59a) to correctly calculate the energy of the GDR in the shell model (see Chapter I).

Adding the optical potential to the free particle Hamiltonian H_o enables a distorted wave function $\Psi^{opt}(\vec{r},\vec{\xi})$ to be found from the solution of

$$H^{opt}\Psi^{opt}(\vec{r},\vec{\xi}) = E\Psi^{opt}(\vec{r},\vec{\xi}) \qquad \text{IV-7}$$

where $H^{opt} = H_o + V_{opt}$.

It is shown in Messiah (ME 65b) that the solution to IV-4 satisfies

$$\Phi(\vec{r},\vec{\xi}) = \left(1 + \frac{1}{E-H\pm i\varepsilon}\,\delta V\right) \Psi^{opt}(\vec{r},\vec{\xi}) \qquad \text{IV-8}$$

where $\varepsilon \to 0$ in the limit.

Substitution of IV-8 into IV-2 gives

$$M_{i\to f} = \langle\Psi_f|\hat{\varepsilon}|\Psi_i^{opt}\rangle + \sum_\lambda \frac{\langle\Psi_f|\hat{\varepsilon}|\phi_\lambda\rangle\,\langle\phi_\lambda|\delta V|\Psi_i^{opt}\rangle}{E - H \pm i\varepsilon} \qquad \text{IV-9}$$

where the $|\phi_\lambda\rangle$ are the intermediate collective states.

Now the electric multipole operator $\hat{\varepsilon}$ can be split into two parts

$$\hat{\varepsilon} = \hat{\varepsilon}_N + \hat{\varepsilon}_T \qquad \text{IV-10}$$

where $\hat{\varepsilon}_N$ acts on the nucleon and $\hat{\varepsilon}_T$ acts on the target. In addition, the $|\phi_\lambda\rangle$ have, in the present case, only one well defined state $|\phi_R\rangle$ of energy E_R and width Γ_R for a given multipolarity transition. Therefore, IV-9 finally becomes

$$M_{i\to f} = \langle\Psi_f|\hat{\varepsilon}_N|\Psi_i^{opt}\rangle + \frac{\langle\Psi_f|\hat{\varepsilon}_T|\phi_R\rangle\,\langle\phi_R|\delta V|\Psi_i^{opt}\rangle}{E - E_R + i\Gamma_R/2} \qquad \text{IV-11}$$

The first term in IV-11 represents the direct capture process, and the second term the semi-direct one.

Following the direct capture calculations of Donnelly (DO 67), Snover and Ebisawa expanded the initial state wave functions in terms of radial, angular momentum and spin wave functions as usual. Since the initial state consists of a target in its ground state and an incoming nucleon, and the electromagnetic operator consists of a sum of one-body operators, Snover and Ebisawa carry out a fractional parentage expansion of the final bound state at the beginning. This selects out only those parts of the final state which have parentage in the initial state, and therefore simplifies the angular momentum algebra. Upon reduction of the resultant angular momentum algebra, they obtain an expression for the differential cross section of the direct capture part which is written in terms of the reaction matrix elements (R_t of section 3.6) and a Legendre polynomial expansion in the angle of the emitted gamma ray. The reaction matrix elements are proportional to a direct radial matrix element, $R^d_{\ell j}$, via various statistical and phase space factors and angular momentum coupling coefficients, where $R^d_{\ell j}$ is given by

$$R^d_{\ell j}(\mathcal{L}) = \int \frac{\chi_{\ell j}(r)}{r} f_{\mathcal{L}}(r) \frac{U_{LJ}(r)}{r} r^2 dr \qquad \text{IV-12}$$

where $\chi_{\ell j}(r)$ and $U_{LJ}(r)$ are the radial parts of the initial and final state wave functions, respectively, and $f_{\mathcal{L}}(r)$ is the appropriate direct electric multipole operator. The $\chi_{\ell j}(r)$ are normalized by a phase factor $e^{i\sigma_\ell}$, where σ_ℓ is the Coulomb phase, and $U_{LJ}(r)$ is normalized by the spectroscopic factor $C^2\mathcal{S}_{LJ}$ for the final state.

With the inclusion of the semi-direct part of IV-11, the radial matrix element is modified to

$$R_{\ell j}(\mathcal{L}) = R^d_{\ell j}(\mathcal{L}) + \frac{\alpha_{\mathcal{L}T} \int \frac{\chi_{\ell j}(r)}{r} F_{\mathcal{L}T}(r) \frac{U_{LJ}(r)}{r} r^2 dr}{E - E_{\mathcal{L}T} + i\Gamma_{\mathcal{L}T}/2} \qquad \text{IV-13}$$

where $\alpha_{\mathcal{L}T}$ is the strength with which the given resonance of order $\mathcal{L}$, isospin T, is excited

and $F_{\mathcal{L}T}(r)$ is a form factor which describes the manner in which the collective state is excited.

Snover and Ebisawa (SN 76) choose a hydrodynamic model form factor for $F_{11}(r)$; that is, the collective model description of the GDR is taken to be that of an oscillation of all the protons in the nucleus against all the neutrons in the nucleus, with the nuclear surface remaining rigid. In this case, $F_{11}(r)$ is given by $rV_1(r)$ where $V_1(r)/4$ is the real symmetry term in the optical potential. For proton radiative capture, α_{11} is given by

$$\alpha_{11} = \frac{3\hbar^2 Z\beta_{11}}{4M_p A\langle r^2\rangle E_{11}} \qquad \text{IV-14}$$

where β_{11} is the fraction of the classical dipole sum rule (equation I-1) exhausted by the resonance of energy E_{11}

and $\langle r^2\rangle$ is the mean squared radius of the charge distribution in the nucleus.

The extension of the model to include direct E2 is straightforward and involves, for example, using $\ell = 2$ for the direct form factor $f_\ell(r)$. Collective isoscalar E2 strength is introduced by using a form factor $F_{\ell T}(r)$ given by

$$F_{20} = -r\,\frac{dV_o(r)}{dr} \qquad \text{IV-15}$$

where $V_o(r)$ is the real central nuclear potential. The strength $\alpha_{\ell T}$ is given by

$$\alpha_{20} = \frac{\hbar^2\beta_{20}}{2M_p E_{20}} \qquad \text{IV-16}$$

where β_{20} is the fraction of the EWSR (equation I-2) exhausted by the E2 resonance.

The quantities $E_{\ell T}$, $\beta_{\ell T}$ and $\Gamma_{\ell T}$ are not specified by the model. They are adjusted to fit the total cross section as well as possible.

4.2 The Optical Model and Calculation of the Wave Functions

The radial parts of the initial scattering state wave functions, $\chi_{\ell j}(r)$, are calculated in the optical model, first proposed by Fernbach, Serber and Taylor (FE 49) to describe the scattering of incident projectiles off a nucleus. The optical potential is given by

$$V_{opt} = V_{CN} + V_{SO} + V_{coul} \qquad \text{IV-17}$$

where V_{CN} and V_{SO} are the (complex) central nuclear and spin orbit potentials, respectively, and V_{coul} is normally taken to be that of a uniformly charged sphere of radius R_c, and is given by

$$V_{coul} = \begin{cases} \dfrac{Z_I Z_T e^2}{2R_c}\left(3 - \dfrac{r^2}{R_c^2}\right) & \text{for } r < R_c \\ \dfrac{Z_I Z_T e^2}{r} & \text{for } r > R_c \end{cases}$$

where Z_I and Z_T are the atomic numbers of the incident and target nuclei, respectively.

Normally to calculate the wave functions, optical potentials taken from elastic scattering data involving the incident nucleon (in this case, a proton) and the target nucleus under consideration (^{12}C) would be used. Unfortunately, no optical potential exists which satisfactorily describes both the differential cross section and analyzing power of the reaction $^{12}C(\vec{p},p_o)^{12}C$ in the energy region of interest here. The problem is that both of these quantities vary rapidly as a function of energy; thus the smoothly varying optical potential is not able to match the fluctuations. The rapid variations are caused by the dominance of resonance structures throughout this region, as shown in the data of Meyer <u>et</u> <u>al</u>. (ME 76).

An attempt to describe the elastic scattering of protons from carbon from $E_{\vec{p}}$ = 12 MeV to 20 MeV was made by Nodvik, Duke and Melkanoff (NO 62). These authors assumed the optical potential to be of the following form:

$$\mathrm{Re}(V_{CN}) = - V\, f(r) \qquad \text{IV-18}$$

$$\mathrm{Im}(V_{CN}) = - W \exp\{-(r-R)^2/b^2\} \qquad \text{IV-19}$$

$$V_{SO} = -\left(\frac{\hbar}{m_\pi c}\right)^2 \frac{V_S}{r} \frac{df(r)}{dr}\, \vec{\sigma}\cdot\vec{\ell} \qquad \text{IV-20}$$

$$f(r) = \left[1 + \exp\{(r-r_o)/a\}\right]^{-1} \qquad \text{IV-21}$$

where V, W and V_S are the depths of the various potential wells and $\hbar/m_\pi c = \sqrt{2.0}$ fm.

Nodvik <u>et</u> <u>al</u>. were able to fit the differential cross sections and analyzing powers quite well individually by letting several of the parameters in equations IV-18 to IV-21 vary, but they could not fit both quantities well simultaneously. In addition, the parameters fluctuated wildly as a function of energy, thereby violating the spirit of the optical model. Their final results included compromise potentials which generally did reasonably enough for the differential cross sections, but did not do so well for the analyzing powers.

Another set of optical model parameters was obtained by Watson, Singh and Segel (WA 69). These authors fitted the differential cross section and polarization data for a variety of p-shell nuclei, including ^{12}C, over the energy range from $E_{\vec{p}}$ = 10 MeV to 50 MeV. Their form of the optical potential was the same as that used by Nodvik <u>et al</u>., except that the Gaussian shape for the imaginary part of the central potential was replaced by a surface derivative form given by

$$\mathrm{Im}(V_{CN}) = 4a_I W \frac{df(r)}{dr} \qquad \text{IV-22}$$

The diffuseness a_I of the imaginary part was given a value slightly different from the diffusenesses of the real and spin-orbit parts of the potential.

The fits obtained by Watson <u>et al</u>. to the data on elastic scattering from ^{12}C were not, in general, as good as those obtained by Nodvik <u>et al</u>. This was to be expected (PE 70), since Watson <u>et al</u>. were fitting a wider range of nuclei and their parameters were constrained to be smooth functions of energy, while those of Nodvik <u>et al</u>. were not.

Thus, it was decided to attempt to find a better set of optical model parameters that would describe more satisfactorily both the differential cross section and analyzing power for the $^{12}C(\vec{p},p_0)^{12}C$ reaction. The data of Meyer _et al_. (ME 76) were used in the analysis. The starting parameters were taken to be those of Sené _et al_. (SE 70), who fitted polarized neutron scattering data from ^{12}C at $E_{\vec{n}}$ = 14.1 MeV reasonably successfully. The form of the optical potential was taken to be the same as that used by Watson _et al_., except that all three of the shapes f(r) (equation IV-21) were allowed to have independent radii and diffusenesses. The optical model code ABACUS-2[1] was used to perform the calculations. A slight modification to the code was made so that the shape parameters for the spin-orbit potential could be given values independent of those used for the shape of the central nuclear potential. By systematically varying the parameters, it was found that a fairly good fit could be obtained to the differential cross section and analyzing power data simultaneously. The parameters which best fit the data are listed in Table IV-1. Also listed in this table are the parameters obtained by Watson _et al_., to be referred to as WSS, and by Becchetti and Greenlees (BE 69b), to be referred to as BG. This last set was obtained for a wide range of nuclei with A>40, E<50 MeV. Some comments on the new set of parameters follow.

---

[1] Written by E. H. Auerbach at Brookhaven National Laboratory and adapted for use at the University of British Columbia by T. W. Donnelly and A. L. Fowler.

Table IV-1

Optical Model Parameters

Parameter*	Potential: WSS	BG	NEW
$(R_\circ)_R$	1.15-.001E	1.17	1.13
$(R_\circ)_I$	1.15-.001E	1.32	1.40
$(R_\circ)_{SO}$	1.15-.001E	1.01	.88
a_R	.57	.75	.55
a_I	.50	.51	.12
a_{SO}	.57	.75	.24
V	60-.28E+.4Z/$A^{1/3}$	54-.32E+.4Z/$A^{1/3}$	58.4
W	.59E (E<15 MeV) 9.6-.055E (E>15 MeV)	.22E-2.7 (>0) Gaussian 11.8-2.5E (>0) Surface derivative	25.42-.43E
V_{SO}	5.5	6.2	7.28-.12E

*radii and diffusenesses are in fm, potentials are in MeV, E is the laboratory energy. $R_\circ$ refers to the coefficient of $A^{1/3}$ in $r=R_\circ A^{1/3}$. Terms proportional to (N-Z) have been suppressed since N=Z for ^{12}C.

The well depths for the new potential (NEW) are fairly reasonable when compared to other optical model analyses. The depth of the real central potential is expected to have an energy dependence because of its non-locality and a Coulomb term proportional to $ZA^{-1/3}$ (PE 63). These are seen explicitly in the WSS and BG potentials. However, in the present analysis V fluctuated considerably and an overall trend was difficult to detect, so it was left constant at the value it had at $E_{\vec{p}}$ = 16.964 MeV. Neither the differential cross section nor the analyzing power varied too rapidly for a few hundred kilovolts either above or below this energy, so the effect of resonances is apparently not too strong.

The radius parameters for the imaginary and spin-orbit parts of all three potentials are quite different. However, it was found that the extreme values obtained for NEW gave the best fits to both the differential cross section and analyzing power. An increase of 10% in $(R_o)_{SO}$ to bring it more into line with the other analyses worsened the χ^2 of the fit (defined as

$$\chi^2 = \sum_{i=1}^{N} \frac{1}{(\sigma_i^{exp})^2} (\Psi_i^{fit} - \Psi_i^{exp})^2$$

the sum going over both the differential cross section and analyzing power data) by about a factor of 20. A decrease in $(R_o)_I$ of 10% worsened χ^2 by about a factor of 3.

While the value for the diffuseness of the real potential well a_R is similar to the other results, a_I and a_{SO} differ markedly. Actually, the value of a_I in the present analysis gives a shape to the imaginary part of the potential which is very similar to that obtained by Nodvik et al. The fits deteriorated rapidly when either a_I or a_{SO} was varied from its optimum value.

Shown in Figure IV-2 are the fits to the differential cross section and analyzing power data at $E_{\vec{p}}$ = 16.964 MeV obtained with the Nodvik et al. (NDM), WSS and NEW parameter sets. The analyzing power data is clearly fit much better with NEW, especially at the forward angles, and this was characteristic of the fits at all energies. There is not much to choose between NDM and NEW for the fits to the differential cross section at this or any other energy; WSS consistently underestimates this quantity at all the energies.

One disappointing aspect of all three of these optical model sets is that none of them reproduce satisfactorily the partial reaction cross sections. Shown in Figure IV-3 is a compendium of reaction cross section data (ME 77) for the $d_{3/2}$ and $s_{1/2}$ partial waves, and the reaction cross sections for these partial waves calculated with the various potentials.

The potential sets give $d_{3/2}$ reaction cross sections which do turn over similarly to the data, but at a lower energy. The calculated $s_{1/2}$ partial cross sections continue to rise at lower energies, contrary to the data. It is possible to include the total reaction cross section in the χ^2 search for the best fit, but it is difficult to know how to weight this quantity (PE 70), and in improving the fit to the reaction cross section, it may happen that the quality of the fits to the differential cross section and analyzing power will deteriorate badly. Hence, it was decided not to include the reaction cross section in the fitting procedure.

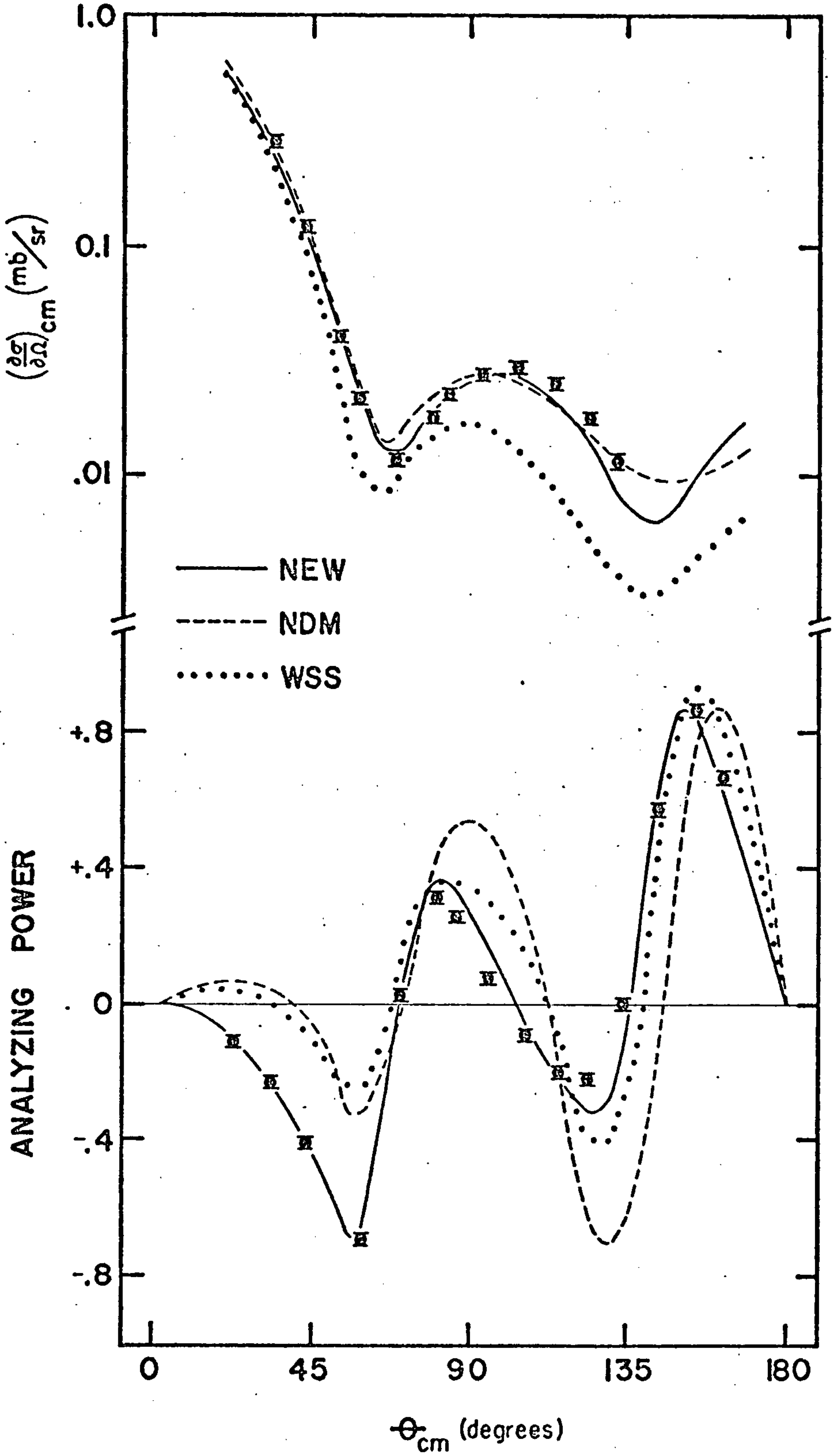

Fig. IV-2 : $^{12}C(\vec{p},p_o)^{12}C$ differential cross section and analyzing power at $E_{\vec{p}}$ = 16.964 MeV. The data are from reference (ME 76). The curves are from optical model fits using the potentials shown.

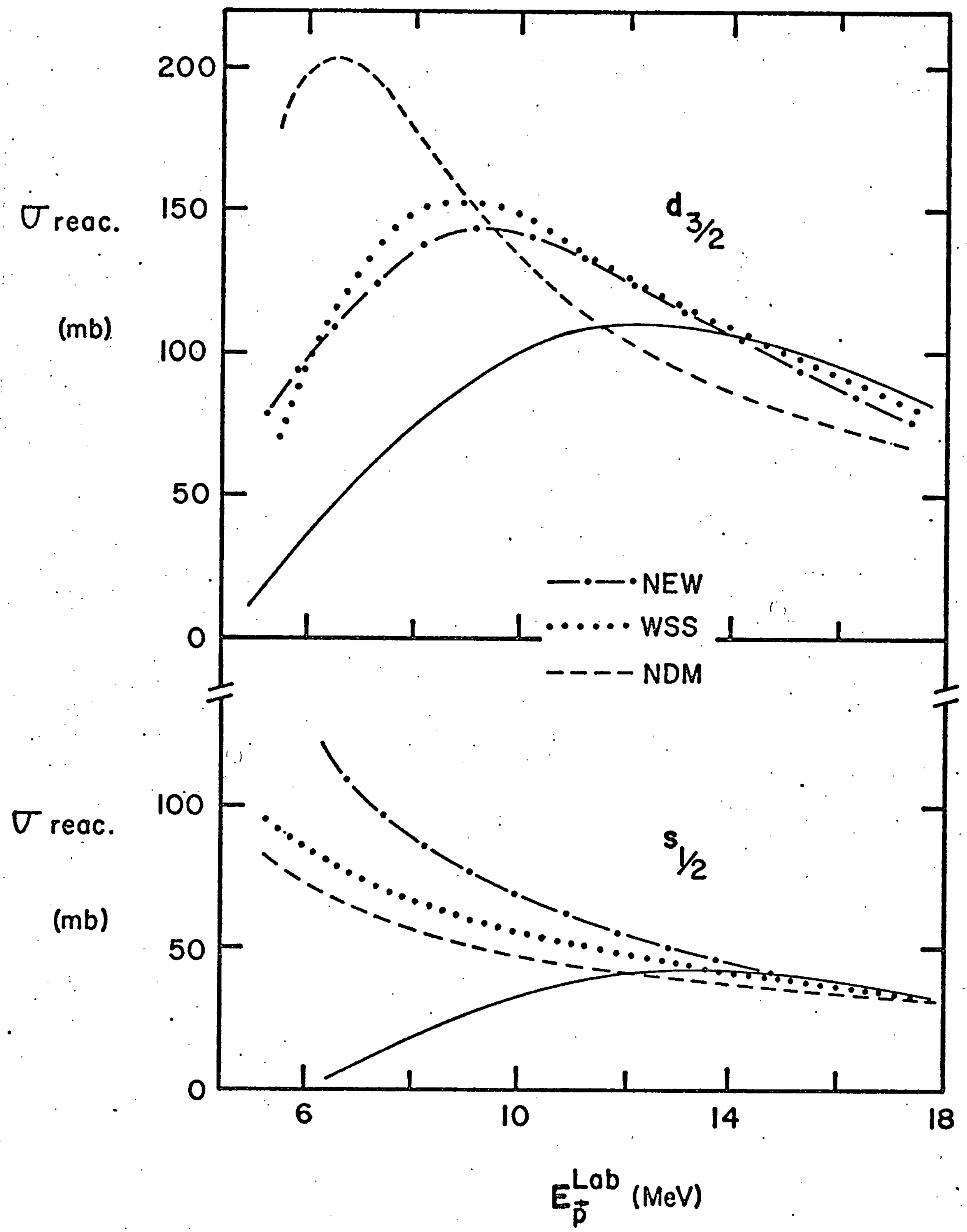

Fig. IV-3 : Comparison of the optical model analyses with some experimental partial reaction cross sections. The solid curve is a compendium of data (ME 77).

It is indeed not too surprising that the observed quantities - the differential cross section, the analyzing power and the partial reaction cross section - are not all well reproduced by this simple use of the optical model. It has been shown in the work of Mikoshiba, Terasawa and Tanifuji (MI 71) that it is important to consider the effects of coupling between scattering in the elastic channel and scattering in the inelastic channel to the 2^+ state in ^{12}C at $E_x = 4.43$ MeV. These authors investigated the region from $E_{\vec{p}} = 4$ MeV to 8 MeV with a coupled channel calculation and found that it was possible to fit reasonably well the observed excitation functions and angular distributions of both the cross section and analyzing power at these low energies. In order to extend this type of calculation to the energies of interest in the present work it would be necessary to consider the coupling of other inelastic channels in addition to the one at 4.43 MeV to the elastic channel. This was shown in the work of Johnson (JO 74) who extended the calculations of Mikoshiba <u>et al</u>. to higher energies and found that the model began to break down seriously at about $E_{\vec{p}} = 10$ MeV. A major computational effort would therefore be required to extend this approach to higher energies and this was not attempted in the present work.

All three parameter sets (NDM, WSS and NEW) were used to calculate the initial scattering state wave functions $\chi_{\ell j}(r)$ and the final bound state wave function, $U_{LJ}(r)$. The latter was found by setting $W = 0$, and varying V to fit the binding energy (E_B) of a ($p_{1/2}$) proton in the ground state of ^{13}N (E_B = -1.94 MeV). The real parts of the radial wave function calculated for the bound $p_{1/2}$ state, the initial scattering states $s_{1/2}$ and $d_{3/2}$ and the form factor $rV_1(r)$ used for the collective part of the E1 capture, are shown in Figure IV-4. It can be seen from these plots why the $d_{3/2}$ wave is expected to be dominant in the capture; it is because the $s_{1/2}$ wave has a node inside the nuclear interior (the nuclear radius is shown as 'r_o') leading to a partial cancellation of its contribution to the cross section.

4.3 Calculation of the Direct Semi-Direct Capture

The first parameter from a direct semi-direct capture calculation that must be matched to experiment is the total cross section. This is true because most of the total cross section arises from electric dipole capture, and if the E1 strength cannot be accounted for correctly, then calculations including E2 strength would be of dubious value. Thus the calculation of the total cross sections including the GDR and direct E1 and E2 capture only are shown in Figure IV-5 as a solid dotted line (NDM), an open dotted line (WSS) and a dot-dash line (NEW). The cross section calculated with the three potentials are indistinguishable in the region of the GDR near E_x = 20.8 MeV. The solid curve is the total cross section taken from reference (BE 76b). The position E_{11} and width Γ_{11} were adjusted to match the shape of the GDR,

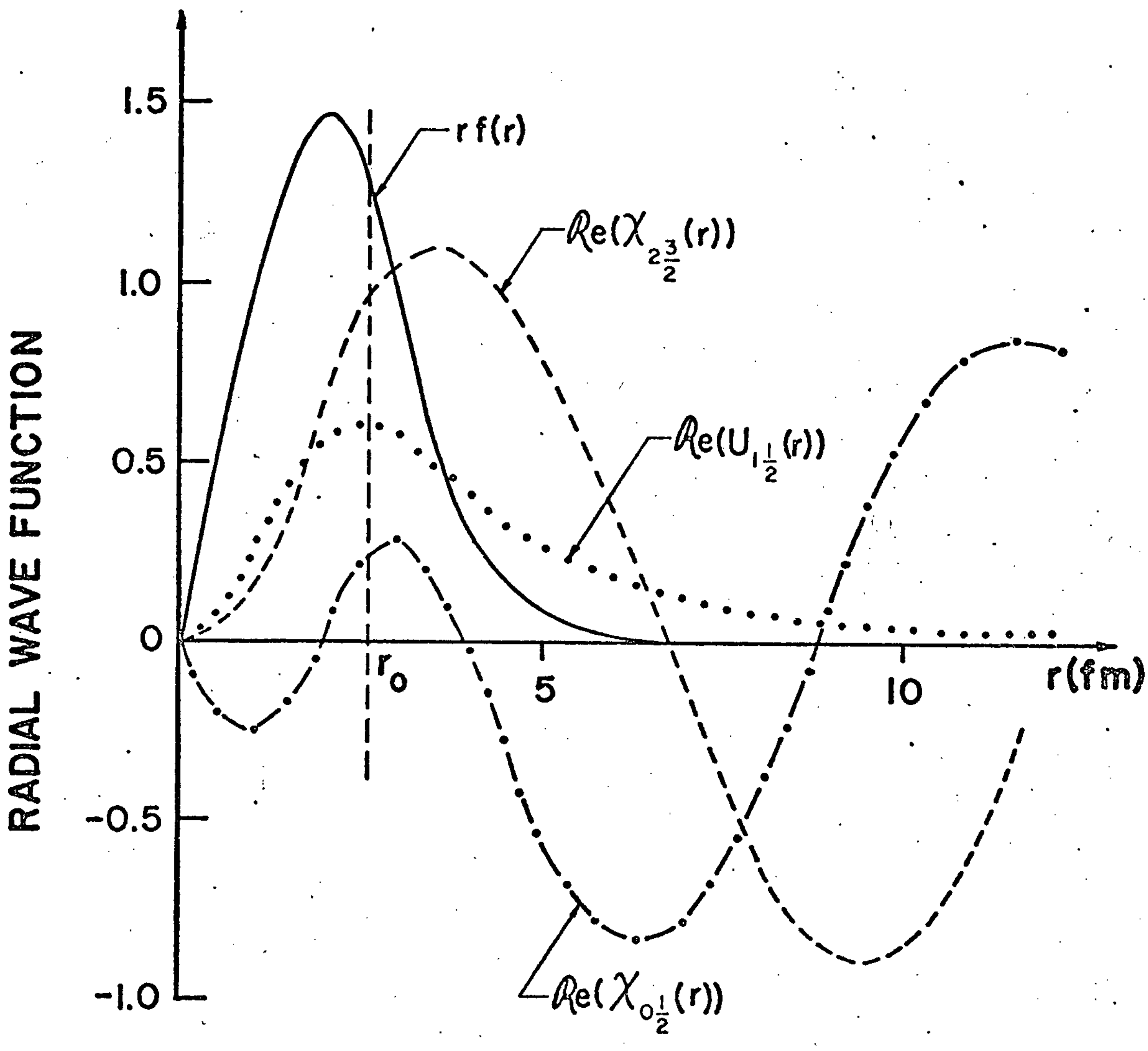

Fig. IV-4 : The real parts of the radial wave functions calculated with the NEW potential. Scattering wave functions ($s_{1/2}$ and $d_{3/2}$) leading to E1 capture only are shown. The form factor rf(r) for volume coupling to the GDR is also shown. r_o indicates the nuclear radius.

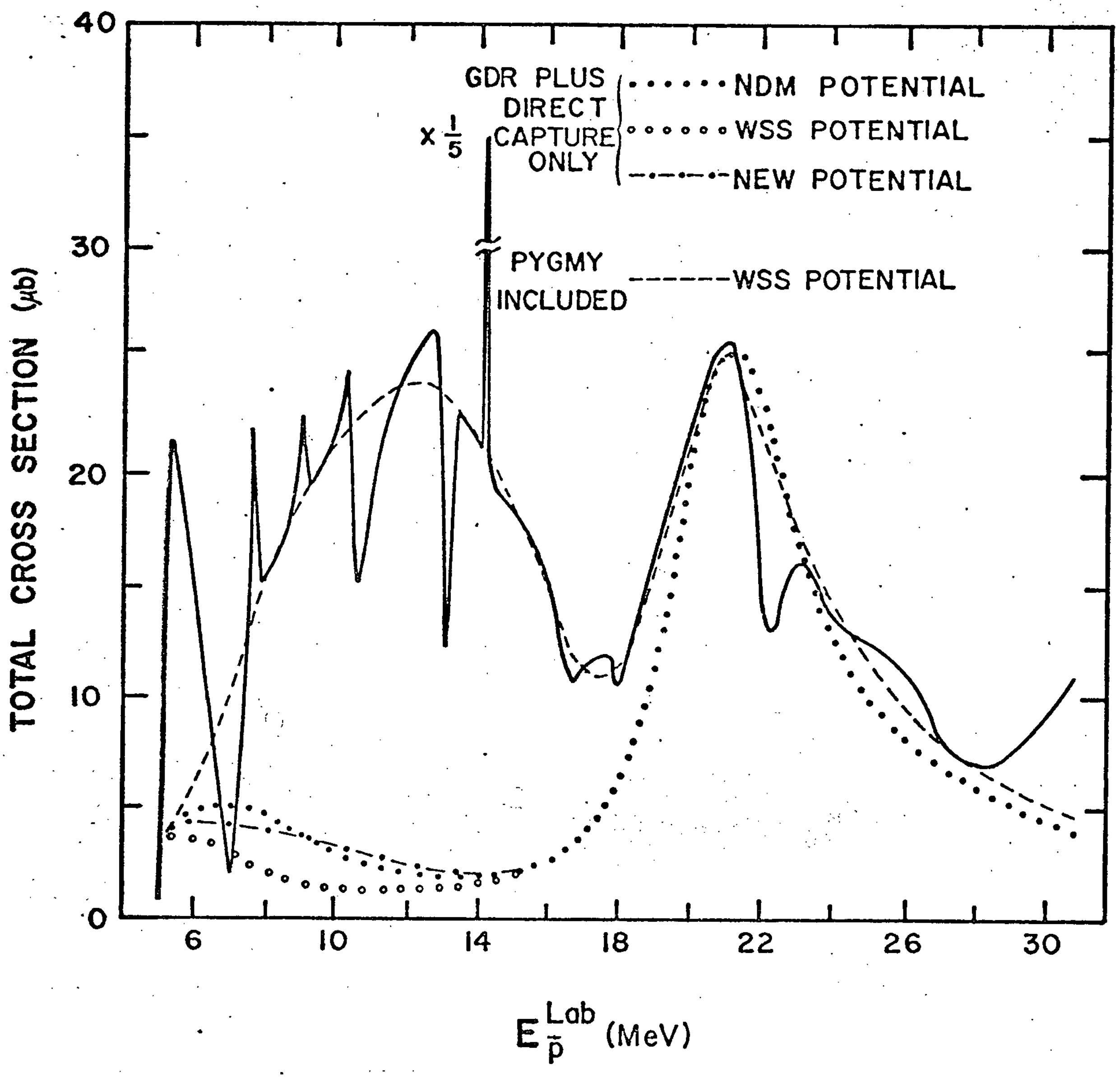

Fig. IV-5 : Fits to the $^{12}C(\vec{p},\gamma_0)^{13}N$ total cross section. The solid curve is a fit (by eye) to the data of Berghofer et al. (BE 76b).

and β_{11} was adjusted to match the total cross section. The symmetry potential $V_1(0)$ was taken to be 100 MeV from an estimate given by Bohr and Mottelson (BO 69c), and the mean square radius $\langle r^2 \rangle$ was taken to be 6.0 fm^2 from electron scattering results on ^{14}N (ME 59) ($\langle r^2 \rangle$ is approximately constant for p-shell nuclei (PR 75)).

It is clear that all three potential sets give no indication of the presence of the pygmy resonance. Presumably, this is because the coupling with the inelastic channels in the calculation of the wave functions has been ignored. Note also that the pygmy resonance shape somewhat resembles the shape of the $d_{3/2}$ partial absorption cross section (Figure IV-3). Failure to reproduce the latter might have some effect on the failure to reproduce the pygmy if the pygmy is mainly a $d_{3/2}$ resonance.

Some evidence supporting the importance of considering the coupling of inelastic channels in calculations of the (p,γ_0) cross sections is found in the work of Johnson (JO 74), who did a coupled channel calculation for the $^{12}C(p,\gamma_0)^{13}N$ reaction for energies up to $E_p = 9$ MeV. This is below the lowest energy measured in the present work, but it does extend into the low energy tail of the pygmy resonance. His calculation of the 90° yield curve, which results mostly from E1 capture, reproduces the experimental measurements very well. However, it has already been stated that his model begins to break down near the energy where the present measurements begin, so more complicated couplings would have to be introduced.

Therefore, in order to reproduce the presence of the pygmy resonance, it was necessary to introduce a second collective E1 amplitude into the present calculation. This has sometimes been necessary in previous calculations with the DSD model; for example, Snover _et al._ (SN 76) provide for fragmentation of the GDR in ^{15}N by including a small second resonance amplitude. The dashed line in Figure IV-5 shows the result of including a second amplitude in the present case using the WSS potential. The results of the calculation for all three potentials agreed to within ±20% for the total cross section and also for most of the other quantities calculated by the model, so only the results using WSS (the most general of the three potentials) will be referred to in future. The only exception was that NEW tended to give E2 direct capture cross sections that were about 40% larger than NDM or WSS above $E_{\vec{p}}$ = 16 MeV. The parameters used to reproduce the total cross section shown in Figure IV-5 are listed in Table IV-2.

Table IV-2

GDR Parameters Used to Reproduce the Total Cross Section Using the WSS Potential

	E_{11}	Γ_{11}	β_{11}
GDR	20.5 MeV	4.0 MeV	0.6
Pygmy	13.8 MeV	6.0 MeV	1.8

The very large value for β_{11} required to reproduce the pygmy resonance indicates that the pygmy is not a fragment of the GDR. It is not the result of isospin splitting of the GDR, for example. Nevertheless, reference to the figures shown in

Chapter III indicates that the model is reasonably successful in reproducing most of the experimental quantities. The solid lines in these figures represent the calculation referred to above. In cases where a dotted line is shown, an isoscalar E2 resonance is assumed to lie at E_x = 25 MeV (see below).

In Figure III-7, it can be seen that the calculations follow the trend of the measured angular distribution coefficients fairly well. The magnitude of the calculated a_3 is possibly a little low, and b_1 is perhaps more constant than the calculation indicates. The calculation also fails to reproduce the broad structure in a_2; this is very likely related to its failure to reproduce the s,d phase difference as seen in Figure III-8. The d-wave and s-wave amplitudes are well reproduced for the solution I values however, and the calculated phase difference represents a fairly good average value of the measured one. Nothing is present in the model as it stands to produce such a phase variation; here again, calculating the wave functions with allowance for coupling to the inelastic channels would be very interesting.

Neither the magnitude of the p/f ratio nor the p,f phase difference is given correctly by the model although the differences are not too severe. This is seen in Figure III-9, where it is also noted that the magnitude of the p,d phase difference is a little low. The f,d phase difference is well reproduced beyond the structure that is observed between 10 MeV and 14 MeV.

Finally, it can be seen in Figure III-12 that direct E2 capture alone satisfactorily accounts for the experimentally measured cross sections if the "low" consistent set of solutions are the correct ones.

The dotted lines in the figures are the result of assuming that an isoscalar E2 resonance exists at the expected energy of E_x = 25 MeV (see Chapter I). In the calculation, the width was taken to be the same as that of the GDR (Γ_{20} = 4 MeV), and the E2 resonance was assumed to exhaust 50% of the sum rule (β_{20} = 0.5). The central nuclear potential was taken to be $V_o(0)$ = -50 MeV (BO 69c). Over most of the region, Figure III-12 shows that the cross section is relatively insensitive to the presence of such a resonance, but at $E_{\vec{p}}$ = 16 MeV and 17 MeV, the calculation is in disagreement with the data. It is shown in Figure III-7 that the assumption of an E2 resonance brings the calculated a_3 into better agreement with the data, but the calculated a_1 becomes larger than the present measurements.

Overall, there appears to be no need to incorporate collective E2 strength into the calculation, since the inclusion of only direct E2 amplitudes provides a reasonable description of the angular distribution coefficients and the extracted E2 cross sections.

4.4 Sum Rules

Another test for the presence of collective strength in a reaction is that an appreciable fraction of the appropriate sum rule should be exhausted (BE 76a). Of course it is also necessary that this strength be concentrated in a sufficiently narrow energy range that it will appear as a resonance, which does not seem to be the case for the present measurements. Nevertheless, the direct capture contribution to the sum rules can often be significant. After converting the measured $(\vec{p},\gamma_0)$ E2 cross sections to the inverse (γ,p_0) E2 cross sections using the detailed balance theorem (Appendix A) the integral of equation I-2 from $E_{\vec{p}}$ = 10.0 MeV to 17.0 MeV (E_x = 11.1 MeV to 17.6 MeV) was found to be 0.44 ± 0.17 μb/MeV, corresponding to 10.3 ± 4.0% of the EWSR (Appendix A). These errors include the ±20% overall normalization error in the determination of the total cross section by Berghofer _et al._ (BE 76b). The fraction of the EWSR exhausted by the _calculated_ direct capture E2 cross section (WSS potential) is 6.8%. Thus the fraction of the EWSR exhausted in the $^{12}C(\vec{p},\gamma_0)^{13}N$ reaction is consistent with the calculated fraction assuming the E2 part of the reaction is proceeding solely by direct capture.

4.5 Comparison with Other Work

The E2 strength that is extracted from the present measurements is very typical of that found in other (p,γ) reactions. Detailed comparisons can be made with the results of studies of the $^{14}C(\vec{p},\gamma_0)^{15}N$ and $^{15}N(\vec{p},\gamma_0)^{16}O$ reactions, since complete analyses of these reactions are available (SN 76, AD 77). In the $^{14}C(\vec{p},\gamma_0)^{15}N$ reaction, the total E2 cross sections are typically 1.0 μb from E_x = 19.5 MeV to 27.0 MeV, compared to E2 cross sections of the order of 0.2 μb from

E_x = 11.1 MeV to 17.6 MeV in the present study. However, because of the energy-squared factor in the denominator of the EWSR, both reactions exhaust similar amounts of the sum rule limit; (10.3 ± 4.0)% of the sum rule limit is depleted in the present case compared to (6.8 ± 1.4)% in the case of $^{14}C(\vec{p},\gamma_0)^{15}N$.

A somewhat different situation possibly exists in the (γ,p_0) channel of the photodisintegration of ^{16}O. In a study of the $^{15}N(\vec{p},\gamma_0)^{16}O$ reaction, Hanna <u>et</u> <u>al</u>. (HA 74a) found evidence for a GQR which exhausted approximately 30% of the EWSR between E_x = 20.2 MeV and 26.8 MeV (about 7% of the EWSR is exhausted for the calculated E2 direct capture through this region (SN 76)). Because of the large difference in the concentration of E2 strength found in this reaction from that found in the $^{14}C(\vec{p},\gamma_0)^{15}N$ reaction, Adelberger <u>et</u> <u>al</u>. (AD 77) remeasured the $^{15}N(\vec{p},\gamma_0)^{16}O$ reaction from $E_{\vec{p}}$ = 8 MeV to 18 MeV (E_x = 19.6 MeV to 29 MeV). Considerably less E2 strength was found in the new measurement, although there was still an excess over direct capture near E_x = 20.6 MeV and 24.8 MeV. It should be pointed out that in the analysis of the original data, Hanna <u>et</u> <u>al</u>. excluded A_1 and B_1 from the fits to the T-matrix elements and so the E2 cross sections obtained were presumably subject to the limitations discussed at the end of section 3.8.

All three of these $(\vec{p},\gamma_0)$ reactions show a great many similarities. The a_k and b_k coefficients show roughly the same trends; a_1 and b_3 both become slowly more positive with increasing excitation energy, for example, and a_3 becomes more negative. As a result of the similarities in the angular distributions, the behaviour of the T-matrix elements is much the same. All three reactions are afflicted with the presence of secondary solutions some of which are acceptable in a statistical sense. In fact, in the case of the $^{14}C(\vec{p},\gamma_0)^{15}N$ reaction, some of the second solutions were "preferred" in the sense that they had lower chi-squares than those for solution I. All three reactions show the same behaviour when A_1 and B_1 are excluded from the analysis; namely, the extracted E2 cross sections are systematically higher and the A_1 and B_1 coefficients that are reproduced from the analysis which excluded them are consistent with the measured values only when the errors of the reproduced coefficients are taken into account. Finally, if the solution I values for σ_{E2} are taken to be correct, then all three excitation functions are satisfactorily reproduced by considering only direct E2 capture (with no collective E2 capture) interfering with direct and collective E1 capture.

This result is in accord with (p,γ_0) measurements in other light nuclei. For example, Noe et al. (NO 76) find by comparison to calculations with the DSD model, that there is no evidence for collective E2 strength above the GDR in the $^{11}B(p,\gamma_0)^{12}C$ reaction.

The amount of E2 strength seen in the present study is also similar to the strength seen in many (α,γ) reactions. Most of the information about these reactions comes from (α,γ_0) studies on nuclei with ground state $J^\pi = 0^+$, since only natural parity states can then be formed in the compound system, thereby permitting an unambiguous determination of the E1 and E2 strengths through measurements of the angular distributions. For example, Snover et al. (SN 74) studied the reaction $^{12}C(\alpha,\gamma_0)^{16}O$ and found 17% of the EWSR was exhausted between E_x = 12 MeV and 28 MeV. Similar results are obtained for other (α,γ_0) studies on spin 0 nuclei ranging up to A = 60; namely, about 1%/MeV of the EWSR is exhausted (HA 74c).

Thus, the present measurement of the E2 strength in ^{13}N is in agreement with similar capture reaction measurements in other light nuclei. It is also in agreement with a variety of inelastic scattering measurements on the near-by nuclei ^{12}C and ^{16}O. As mentioned in the introduction, the inelastic scattering studies on these nuclei have shown the quadrupole strength to be very much spread out. It should be noted, of course, that the present experiment investigated <u>only</u> the (γ,p_0) channel in the decay of ^{13}N. Many other possible decay branches exist, for example, proton decays to excited states in ^{12}C and neutron, alpha and deuteron, etc. decays to various levels in other neighbouring nuclei, although many of these channels are not open until higher excitation energies are reached.

Moreover, there often appears to be little strength in the other charged particle channels. For example, Weller and Blue (WE 73) investigated radiative deuteron capture by ^{11}B from E_x = 19.5 MeV to 22.3 MeV. They found that the total (γ,d_0) cross section was 13% of the total (γ,p_0) cross section measured in the $^{12}C(p,\gamma_0)^{13}N$ reaction (FI 63). If E2 deuteron decay exhibits the same characteristics as E2 proton and alpha decay ($\sigma_{E1} \simeq 1\% \, \sigma_{E2}$), then the amount of E2 strength in the deuteron channel must be very small indeed. Other nuclei near mass 13 studied with (d,γ_0) reactions include ^{15}N (DE 76) and ^{11}B (DE 74). Some evidence for M1 or E2 radiation occurring in the region of the GDR of these reactions is evident from non-zero a_1 coefficients, but no quantitative estimates were made.

Similarly, small amounts of E2 or M1 strength are seen in ^3He capture reactions on ^{12}C and ^{16}O (SH 74) through observation of non-zero a_1 coefficients. Snover and Ebisawa (EB 77) have recently found a contribution of about 0.3% of the EWSR in the $^{13}C(^3He,\gamma_0)^{16}O$ reaction from E_x = 24 MeV to 38 MeV.

The present results, then, indicate that the E2 strength in ^{13}N is very spread out.

No other quantitative measurements have been made in the mass 13 nuclei, but Shin _et al._ (SH 71) observed small non-zero a_1 and a_3 coefficients in photoproton angular distributions from inelastic electron scattering on ^{13}C at excitation energies ranging from 21 to 32 MeV. Shin _et al._ also observed much larger a_3 coefficients in a similar study on ^{12}C. These authors point out that the GDR is more concentrated in ^{12}C and thus the effects of E2 interference will be seen more clearly in the tail regions of the GDR of this nucleus than will be seen in the tail regions of the more spread out GDR of ^{13}C. Inelastic alpha scattering on ^{12}C (KN 76) has shown that less than 20% of the EWSR is exhausted between E_x = 15 MeV and 30 MeV in ^{12}C, and so it would seem that the present $^{12}C(\vec{p},\gamma_0)^{13}N$ measurement has accounted for a considerable portion of the E2 strength expected in mass 13, especially noting that the present cross sections are actually lower limits.

Chapter V

SUMMARY AND CONCLUSIONS

The main purposes of the present measurements were to extend our knowledge of the nucleus ^{13}N by investigating the nature of the E2 strength in the region below the GDR and to provide a simple test of the DSD capture model of Snover and Ebisawa. These aims have been largely achieved, but for a variety of reasons to be given below, success has not been complete.

It would appear that capture gamma ray reactions induced by polarized protons do not permit as unambiguous a determination of the capture amplitudes as was previously believed. This had already been shown to be true for the $^{14}C(\vec{p},\gamma_0)^{15}N$ and $^{15}N(\vec{p},\gamma_0)^{16}O$ reactions, where the measurements were in the region through and above the GDR. The results from the $^{12}C(\vec{p},\gamma_0)^{13}N$ reaction reported here extend these uncertainties to the region below the GDR as well. The problem is twofold; two solutions exist at several energies which are both statistically acceptable, and there might be some M1 radiation underlying the structure in this region.

So far as the first problem is concerned, there are several reasons to prefer the solution I results. First, these solutions give an E2 cross section which varies more or less smoothly with energy and the observed smooth variation of the angular distribution coefficients would arise naturally from this, but not from a cross section that was fluctuating widely. In addition, the second solutions are not always acceptable in a statistical sense, and those which are not cannot be the physical solutions. Finally, the second solution cannot always be found, for example at $E_{\vec{p}}$ = 12.8 MeV, although this may be the fault of the initial search parameters. Thus a solution which comes and goes might be believed to be just a mathematical solution which has no physical significance.

An attempt to learn about the possible presence of M1 strength was made by performing an analysis in which the coefficients most sensitive to M1 radiation, A_1 and B_1, were excluded. In this analysis, systematically higher values of the E2 cross section were found, although these values also had much larger errors. The reason for the increase in the errors is clear enough - the E2 amplitudes were being extracted from a data set that was less sensitive to their presence. However, it is not clear why the amplitudes were always larger. A major drawback to this analysis was that the valuable χ^2 significance test was lost since there were zero degrees of freedom in the fit. In any event, the solutions determined from using all of the coefficients lay at statistically satisfactory levels, so again these are the preferred solutions.

Accepting the low, consistent set of E2 cross sections as being correct, the results of this experiment agree with many measurements made in other light nuclei. In particular, proton radiative capture into ^{12}C, ^{13}N, ^{15}N and ^{16}O bear many similarities and exhaust roughly equivalent amounts of the

EWSR. The latter result has been observed in a variety of reactions involving light nuclei. Thus the present measurement has further confirmed the systematics of E2 photodisintegration for low A nuclei.

The calculations with the DSD model suffered from the deficiency that the pygmy resonance did not appear naturally from the calculation. This was actually an expected result since Johnson's work showed the importance of the coupling between the ground state and the first excited state of ^{12}C in reproducing the pygmy's low energy tail. It might be noted that several attempts to describe the pygmy with shell model calculations have not been wholly successful (KI 74, JA 71). However, when the presence of the pygmy was artificially introduced into the present calculation, the DSD model was reasonably successful in reproducing the parameters related to E2 capture. In particular, the energy dependences of the odd a_k and b_k coefficients were satisfactorily calculated assuming that only E2 direct capture radiation was interfering with the dominant E1 radiation. The various phases associated with the E2 amplitudes were also given reasonably well by the model. The E2 direct capture cross sections calculated with the model agreed with the measured cross sections, assuming the solution I values were the correct ones.

In summary, no strong evidence for the existence of a GQR located in the region of the GDR is found either in the experimental measurements of the E2 cross section or in comparisons of the results with the DSD model. The E2 cross section contributes an amount to the EWSR (10.3 ± 4.0%) that is similar to the strength seen in a variety of (p,γ_o) and (α,γ_o) reactions in the region below the expected GQR.

It would be of interest to extend these measurements to higher energies to search for evidence of collective E2 strength. Extension of the measurements both above and below the region studied in the present work using a finer grid would be of interest to establish whether the "resonances" and "dips" observed in some of the extracted quantities are real or merely statistical. It would also be of interest to extend a coupled channel calculation through the pygmy resonance region to try to understand its structure in a more satisfactory way. Much detailed experimental information now exists with which comparisons of such a calculation could be made.

Bibliography

AD 73 E. G. Adelberger, M. D. Cooper and H. F. Swanson, University of Washington Annual Report (1973) p.11.

AD 77 E. G. Adelberger, J. E. Bussoletti, K. Ebisawa, R. L. Helmer, K. A. Snover, T. A. Trainor, University of Washington Annual Report (1977) p.43.

AJ 70 F. Ajzenberg-Selove, Nuclear Physics A, 152 (1970) 1.

AR 75 E. D. Arthur, D. M. Drake and I. Halpern, Physical Review Letters, 35 (1975) 914.

BA 47 G. C. Baldwin and G. S. Klaiber, Physical Review, 71 (1947) 3.

BA 61 F. C. Barker, Nuclear Physics, 28 (1961) 96.

BA 70 Proceedings of the 3rd International Symposium on Polarization Phenomena in Nuclear Reactions, H. Barschall, W. Haeberli, eds., University of Wisconsin Press, Madison (1970) p. xxv.

BA 75 N. L. Back, J. E. Bussoletti, L. D. Knutson, K-L Liu, and T. A. Trainor, University of Washington Annual Report (1975) p.91.

BE 69a Philip R. Bevington, "Data Reduction and Error Analysis for the Physical Sciences", McGraw-Hill, New York, (1969).

BE 69b F. D. Becchetti, Jr., and G. W. Greenlees, Physical Review, 182 (1969) 1190.

BE 76a Fred E. Bertrand, Annual Review of Nuclear Science, 26 (1976) 457.

BE 76b D. Berghofer, M. D. Hasinoff, R. Helmer, S. T. Lim, D. F. Measday and K. Ebisawa, Nuclear Physics A, 263 (1976) 109.

BI 60 L. C. Biedenharn, in "Nuclear Spectroscopy", Part B, F. Ajzenberg-Selove, ed., Academic Press, New York (1960) p.732.

BI 75 J. Birkholz, Physical Review C, 11 (1975) 1861.

BL 52 John M. Blatt and L. C. Biedenharn, Reviews of Modern Physics, 224 (1952) 258.

BO 36 N. Bohr, Nature, 137 (1936) 344.

BO 69a A. Bohr and B. R. Mottelson, "Nuclear Structure", Vol. I, W. A. Benjamin, Inc., New York (1969) Chapter 3.

BO 69b A. Bohr and B. R. Mottelson, "Nuclear Structure", Vol. II, W. A. Benjamin, Inc., New York (1969) Chapter 6.

BO 69c A. Bohr and B. R. Mottelson, "Nuclear Structure", Vol. I, W. A. Benjamin, Inc., New York (1969) Chapter 2.

BR 59a G. E. Brown and M. Bolsterli, Physical Review Letters, 3 (1959) 472.

BR 59b G. E. Brown, Reviews of Modern Physics, 31 (1959) 893.

BR 64 G. E. Brown, Nuclear Physics, 57 (1964) 339.

BU 75a J. Bussoletti, University of Washington Annual Report (1975) p.42.

BU 75b J. Bussoletti, University of Washington Annual Report (1975) p.159.

BU 76a J. E. Bussoletti, K. Ebisawa, K. A. Snover, and T. A. Trainor, University of Washington Annual Report (1976) p.81.

BU 76b J. E. Bussoletti, K. A. Snover, K. Ebisawa, T. A. Trainor, H. E. Swanson, E. G. Adelberger and R. Helmer, Bulletin of the American Physical Society, 21 (1976) 996.

CA 72 R. W. Carr and J. E. E. Baglin, "Nuclear Data Tables A", Vol. 10, p.144.

CL 65 C. F. Clement, A. M. Lane and J. R. Rook, Nuclear Physics, 66 (1965) 293.

CO 55 Bernard L. Cohen, Physical Review, 100 (1955) 206.

CO 69 G. W. Cole, Jr., F. W. K. Firk and T. W. Phillips, Physics Letters B, 30 (1969) 91.

DA 64 W. W. Daehnick, Physical Review, 135 (1964) 1168.

DA 65 M. Danos and E. G. Fuller, Annual Review of Nuclear Science, 15 (1965) 29.

DE 57 S. Devons and L. J. B. Goldfarb, "Handbuch der Physik", Vol 42, Springer-Verlag, Berlin (1957) p.362.

DE 67 Sergio DeBenedetti, "Nuclear Interactions", Wiley, New York (1967) Chapter 1.

DE 74 W. Del Bianco, S. Kundu and B. Rouben, Nuclear Physics A, 232 (1974) 333.

DE 76 W. Del Bianco, S. Kundu and J. Kim, Nuclear Physics A, 270 (1976) 45.

DI 68 F. S. Dietrich, M. Suffert, A. V. Nero and S. S. Hanna, Physical Review, 168 (1968) 1169.

DO 67 T. W. Donelly, Ph.D. Thesis, University of British Columbia (1967).

EA 62 B. R. Easlea, Physics Letters, 1 (1962) 163.

EB 77 K. Ebisawa and K. A. Snover, University of Washington Annual Report (1977) p.51.

FA 71 H. Fauska, E. Preikschat, G. W. Roth and W. G. Weitkamp, University of Washington Annual Report (1971) p.6.

FE 49 S. Fernbach, R. Serber and T. B. Taylor, Physical Review, 75 (1949) 1352.

FI 63 P. S. Fisher, D. F. Measday, F. A. Nikolaev, A. Kalmykov and A. B. Clegg, Nuclear Physics, 45 (1963) 113.

FL 68 D. G. Fleming, J. Cerny, C. C. Maples and N. K. Glendenning, Physical Review, 166 (1968) 1012.

FU 73 E. G. Fuller, H. M. Gerstenberg, H. Vander Molen and S. C. Dunn, NBS Special Publication 380 (1973).

GE 53 Murray Gell-Mann and Valentine L. Telegdi, Physical Review, 91 (1953) 169.

GE 75 H. V. Geramb, K. Amos, R. Sprickmannn, K. T. Knopfle, M. Rogge, D. Ingham and C. Mayer-Boricke, Physical Review C, 12 (1975) 1697.

GL 72 H. F. Glavish, S. S. Hanna, R. Avida, R. N. Boyd, C. C. Chang and E. Diener, Physical Review Letters, 28 (1972) 766.

GL 73 H. F. Glavish, Proceedings of the International Conference on Photonuclear Reactions and Applications, Barry L. Berman, ed., Lawrence Livermore Laboratory, Livermore, Calif. (1973) p.755.

GO 48 M. Goldhaber and E. Teller, Physical Review, 74 (1948) 1046.

HA 65 R. C. Hanna, Proceedings of the 2nd International Symposium on Polarization Phenomena of Nucleons, P. Huber, H. Schopper, ed., Birkhauser Verlag, Basel (1966) p.280.

HA 72 M. Hasinoff, D. Johnson and D. F. Measday, Physics Letters B, 39 (1972) 506.

HA 73a S. S. Hanna, Proceedings of the International Conference on Photonuclear Reactions and Applications, Barry L. Berman, ed., Lawrence Livermore Laboratory, Livermore, Calif. (1973) p.417.

HA 73b I. Halpern, Proceedings of the International Conference on Photonuclear Reactions and Applications, Barry L. Berman, ed., Lawrence Livermore Laboratory, Livermore, Calif. (1973) p.909.

HA 74a S. S. Hanna, H. F. Glavish, R. Avida, J. R. Calarco, E. Kuhlmann and R. LaCanna, Physical Review Letters, 32 (1974) 114.

HA 74b M. D. Hasinoff, S. T. Lim, D. F. Measday and T. J. Mulligan, Nuclear Instruments and Methods, 117 (1974) 375.

HA 74c S. S. Hanna, Proc. Int. Conf. Nucl. Struct. and Spectro., H. P. Blok, A. E. L. Dieperink, eds., Scholar's, Amsterdam, 2 (1974) 249-85.

HA 76 M. N. Harakeh, A. R. Arends, M. J. A. DeVoight, A. G. Drentje, S. Y. Van der Werf and A. Van der Woude, Nuclear Physics A, 265 (1976) 189.

HI 57 Norton M. Hintz, Physical Review, 106 (1957) 1201.

HO 74 A. Hotta, K. Itoh and T. Saito, Physical Review Letters, 33 (1974) 790.

HS 71 T. H. Hsu, J. L. Honsaker, W. J. McDonald and G. C. Neilson, Nuclear Physics A, 174 (1971) 365.

JA 71 H. U. Jager, H. R. Kissener and R. A. Eramzhian, Nuclear Physics A, 171 (1971) 584.

JO 74 D. L. Johnson, Ph.D. Thesis, University of British Columbia (1974).

JO 77 R. Johnson, private communication.

KI 74 H. R. Kissener, A. Aswad, R. A. Eramzhiam and H. U. Jager, Nuclear Physics A, 219 (1974) 601.

KN 76 K. T. Knopfle, G. J. Wagner, A. Kiss, M. Rogge, C. Mayer-Boricke and Th. Bauer, Physics Letters B, 64 (1976) 263.

KO 76 R. Koch and H. H. Thies, Nuclear Physics A, 272 (1976) 296.

KU 74 E. Kuhlmann, J. R. Calarco, D. S. Mavis, V. K. C. Cheng and S. S. Hanna, Stanford Annual Report (1974) p.21.

LA 59 A. M. Lane, Nuclear Physics, 11 (1959) 625.

LE 50 J. S. Levinger and H. A. Bethe, Physical Review, 78 (1950) 115.

LE 64 J. L. Leigh, Ph.D. Thesis, University of British Columbia (1964).

LE 72 M. B. Lewis and F. E. Bertrand, Nuclear Physics A, 196 (1972) 337.

LI 75 S. T. Lim, Ph.D. Thesis, University of British Columbia (1975).

LO 68 G. Longo and F. Saporetti, Nuo Cim, 56b (1968) 264.

LO 69 G. Longo and F. Saporetti, Nuo Cim, 61b (1969) 167.

MA 63 D. W. Marquardt, J. Society of Industrial and Applied Math. 11 (1963) 431.

ME 59 Ulrich Meyer-Berkhout, Kenneth W. Ford and Alex E. S. Green, Annals of Physics, 8 (1959) 119.

ME 65a D. F. Measday, A. B. Clegg and P. S. Fisher, Nuclear Physics, 61 (1965) 269.

ME 65b Albert Messiah, "Quantum Mechanics", Vol. II, North Holland Publishing Co., Amsterdam (1965) Chapter 19.

ME 68 L. Meyer-Schutzmeister, Z. Vager, R. E. Segel and P. P. Singh, Nuclear Physics A, 108 (1968) 180.

ME 73a D. F. Measday, M. Hasinoff and D. L. Johnson, Canadian Journal of Physics 51 (1973) 1227.

ME 73b H. O. Meyer and G. R. Plattner, Nuclear Physics A, 199 (1973) 413.

ME 76 H. O. Meyer, J. S. Dunham, T. A. Trainor and M. P. Baker, Nuclear Physics A, 269 (1976) 269.

ME 77 H. Meyer, private communication.

MI 71 O. Mikoshiba, T. Terasawa and M. Tanifuji, Nuclear Physics A, 168 (1971) 417.

MO 76 H. P. Morsch, P. Decowski and W. Benenson, Physical Review Letters, 37 (1976) 263.

NA 65 O. Nathan and S. G. Nilsson, "Alpha-, Beta- and Gamma-Ray Spectroscopy", Vol. I, Kai Siegbahn, ed., North Holland Publishing Co., Amsterdam (1965) Chapter X.

NO 62 J. S. Nodvik, C. B. Duke and M. A. Melkanoff, Physical Review, 125 (1962) 975.

NO 76 J. Noe, P. Paul, K. A. Snover, M. Suffert and E. K. Warburton, University of Washington Annual Report (1976) p.80.

OC 73 J. S. O'Connell, Proceedings of the International Conference on Photonuclear Reactions and Applications, Barry L. Berman, ed., Lawrence Livermore Laboratory, Livermore, Calif. (1973) p.71.

PA 74 P. Paul, Pure and Applied Physics 40A (1974) 345.

PE 63 F. G. Perey, Physical Review, 131 (1963) 745.

PE 70 F. G. Perey, Proceedings of the 3rd International Symposium on Polarization Phenomena in Nuclear Reactions, H. Barschall, W. Haeberli, eds., University of Wisconsin Press, Madison (1970) p.131.

PI 71 R. Pitthan and Th. Walcher, Physics Letters B, 36 (1971) 563.

PO 73 M. Potokar, A. Likar, F. Cvelbar, M. Budnar and E. R. Hodgson, Nuclear Physics A, 213 (1973) 525.

PR 75 M. A. Preston and R. K. Bhaduri, "Structure of the Nucleus", Addison-Wesley Publishing Co., Reading, Mass. (1975) Chapter 4.

RO 53 M. E. Rose, Physical Review, 91 (1953) 610.

RO 67 H. J. Rose and D. M. Brink, Reviews of Modern Physics, 39 (1967) 306.

RU 74 L. L. Rutledge, Jr. and J. C. Hiebert, Physical Review Letters, 32 (1974) 551.

SA 55 G. R. Satchler, Proc. Phys. Soc., A68 (1955) 1041.

SC 71 P. Schwandt, T. B. Clegg and W. Haeberli, Nuclear Physics A, 163 (1971) 432.

SE 70 R. Sene, P. Delpierre, J. Kahane and M. de Billy de Crespin, Proceedings of the 3rd International Symposium on Polarization Phenomena in Nuclear Reactions, H. Barschall, W. Haeberli, eds., University of Wisconsin Press, Madison (1970) p.611.

SH 54 W. T. Sharp, J. M. Kennedy, B. J. Sears and M. G. Hoyle, AECL CRT-556.

SH 71 Y. M. Shin, C. F. Wong and H. S. Caplan, Nuclear Physics A, 166 (1971) 162.

SH 74 H. D. Shay, R. E. Peschel, J. M. Long and D. A. Bromley, Physical Review C, 9 (1974) 76.

SN 74 K. A. Snover, E. G. Adelberger and D. R. Brown, Physical Review Letters, 32 (1974) 1061.

SN 75 K. A. Snover and K. Ebisawa, University of Washington Annual Report (1975) p.152.

SN 76 K. A. Snover, J. E. Bussoletti, K. Ebisawa, T. A. Trainor and A. B. McDonald, Physical Review Letters, 37 (1976) 273.

SP 69 B. M. Spicer, Advances in Nuclear Physics II (1969) p.1.

ST 50 H. Steinwedel and J. H. D. Jensen, Z. Naturforsch, 5A (1950) 413.

SW 66 J. B. Swint, A. C. L. Barnard, T. B. Clegg and J. L. Weil, Nuclear Physics, 86 (1966) 119.

TE 68 G. E. Terrell, M. F. Jahns, M. R. Kostoff and E. M. Bernstein, Physical Review, 173 (1968) 931.

TO 73 Y. Torizuka, Y. Kojima, T. Saito, K. Itoh, A. Nakada, S. Mitsunobu, M. Nagao, K. Hosoyama, S. Fukuda and H. Miura, Proceedings of the International Conference on Photonuclear Reactions and Applications, Barry L. Berman, ed., Lawrence Livermore Laboratory, Livermore, Calif. (1973) p.675.

TY 58 H. Tyren and Th. A. J. Maris, Nuclear Physics, 7 (1958) 24.

WA 62 E. K. Warburton and H. O. Funsten, Physical Review, 128 (1962) 1810.

WA 69 B. A. Watson, P. P. Singh and R. E. Segel, Physical Review, 182 (1969) 977.

WA 72 Wayne L. Wang and C. M. Shakin, Physical Review C, 5 (1972) 1898.

WA 73 R. B. Watson, D. Branford, J. L. Black and W. J. Caelli, Nuclear Physics A, 203 (1973) 209.

WE 73 H. R. Weller and R. A. Blue, Nuclear Physics A, 211 (1973) 221.

WI 56 D. H. Wilkinson, Physica 22 (1956) 1039.

WI 69 G. Wittwer, H. G. Clerc and G. A. Beer, Physics Letters B, 30 (1969) 634.

ZI 70 J. Zimanyi, I. Halpern and V. A. Madsen, Physics Letters B, 33 (1970) 205.

Appendix A

THE ENERGY WEIGHTED SUM RULE

In this appendix, the means by which the EWSR is evaluated will be presented. This expression was first developed by Gell-Mann and Telegdi (GE 53) for even-even nuclei. The cross section for an electric transition of frequency ω and order L is given by (OC 73)

$$\sigma(\omega L) = (2\pi)^3 e^2 \left[\frac{(L+1)\left(\frac{\omega}{c}\right)^{2L-1}}{L\{(2L+1)!!\}^2}\right] B(EL,\omega) \qquad \text{A-1}$$

where $B(EL,\omega)$ is the reduced transition probability.

Setting $E = \hbar\omega$, equation A-1 becomes

$$\sigma(EL) = (2\pi)^3 e^2 \left[\frac{(L+1)\left(\frac{E}{\hbar c}\right)^{2L-1}}{L\{(2L+1)!!\}^2}\right] B(EL,E) \qquad \text{A-2}$$

which reduces to

$$\sigma(E2) = \frac{4}{75}\,\pi^3 e^2 \left(\frac{E}{\hbar c}\right)^3 B(E2,E) \qquad \text{A-3}$$

for $L = 2$.

Now use is made of the well known sum rule concerning the reduced transition probability and the energy summed over all final states f. This is given by (NA 65)

$$\sum_f B(EL,E)E = \frac{L(2L+1)^2}{4\pi}\,\frac{\hbar^2 Z^2}{2MA} \langle r^{2L-2} \rangle \qquad \text{A-4}$$

where $\langle r^{2L-2} \rangle$ is the (2L-2)th moment of the charge distribution in the ground state of the nucleus, M is the nucleon mass and A is the atomic number of the nucleus.

With L = 2, equation A-4 becomes

$$\sum_f B(E2,E)E = \frac{25}{4\pi}\frac{\hbar^2 Z^2}{MA}\langle r^2\rangle \qquad \text{A-5}$$

Thus, using equation A-3, the EWSR given by

$$\int \frac{\sigma(E2)}{E^2}\,dE = \frac{4}{75}\frac{\pi^3 e^2}{(\hbar c)^3}\sum B(E2,E)E \qquad \text{A-6}$$

reduces to

$$\int \frac{\sigma(E2)}{E^2}\,dE = \frac{\pi^2 e^2}{3\hbar c}\frac{Z^2}{A}\frac{\langle r^2\rangle}{Mc^2} \qquad \text{A-7}$$

Upon setting $e^2/\hbar c = 1/137$ and putting $Z = A/2$, the Gell-Mann-Telegdi result is obtained as

$$\int \frac{\sigma(E2)}{E^2}\,dE = \frac{\pi^2}{137}\frac{A}{12}\frac{\langle r^2\rangle}{Mc^2} \qquad \text{A-8}$$

The oft-quoted sum rule $\int \frac{\sigma(E2)}{E^2}\,dE = 0.22Z^2A^{-1/3}$ μb/MeV follows from putting $\langle r^2\rangle = 3/5\ R^2$, where $R = R_o A^{1/3}$ and $R_o = 1.2$ fm (i.e. the charge distribution is assumed to be uniform throughout the nucleus).

To obtain the EWSR for the nucleus ^{13}N, the expression given in equation A-7 is used. The mean square radius of the charge distribution for ^{13}N was assumed to be the same as the value for ^{14}N. From the work of Meyer-Berkhout _et al._ (ME 59), this is 6.0 fm². Thus from equation A-7, the EWSR limit is 4.29 μb/MeV.

To evaluate $\int \frac{\sigma(E2)}{E^2}\,dE$ for the experimental measurements, it is first necessary to convert the capture $(\vec{p},\gamma_o)$ cross sections to the inverse (γ,p_o) photodisintegration cross sections. This is accomplished using the principle of detailed balance, which states that (DE 67)

$$\sigma(\gamma,p_o) = \sigma(p,\gamma_o)\ \frac{(2I_T+1)(2I_p+1)}{2(2I_A+1)}\ \frac{p_2^2}{p_1^2} \qquad \text{A-9}$$

where I_T, I_p and I_A are the spins of the target nucleus, the proton and the residual nucleus, respectively, in a (p,γ) experiment

and p_1 and p_2 are the centre of mass momenta of the incident particles in the (γ,p) and (p,γ) processes, respectively.

Substitution of the quantities appropriate to the $^{12}C(\vec{p},\gamma_o)^{13}N$ reaction into equation A-9 yields

$$\sigma(\gamma,p_o) = \frac{793.3\ E_p^{Lab}}{E_\gamma^2}\ \sigma(p,\gamma_o)\ \mu b/MeV \qquad \text{A-10}$$

After the E2 photodisintegration cross sections had been determined in this manner, the EWSR was evaluated by breaking up the energy region studied into eight segments. Each of these segments was bounded by energies where experimental measurements were made. The EWSR was then calculated in each segment and the results added together to yield

$$\int_{11.1\ MeV}^{17.6\ MeV} \frac{\sigma(E2)}{E^2}\, dE = 0.44 \pm 0.17\ \mu b/MeV \qquad \text{A-11}$$

Further discussion of this result is given in Chapter IV.

Appendix B

T-MATRIX ELEMENTS

In this appendix, the expressions connecting the angular distribution coefficients to the reaction amplitudes and phases will be developed. Transitions involving M1 radiation will be considered in addition to those involving E1 and E2 radiation.

It has already been stated in Chapter III that for the case of a 0^+ target, $s_{1/2}$ and $d_{3/2}$ incoming partial waves lead to E1 capture, and $p_{3/2}$ and $f_{5/2}$ waves lead to E2 capture. These states will be abbreviated as s, d, p and f, respectively. By angular momentum and parity conservation, $p_{1/2}$ and $p_{3/2}$ partial waves lead to M1 capture. Making use of the tables of Carr and Baglin (CA 72), the connection between the above reduced matrix elements and the unpolarized angular distribution coefficients can be written down immediately. Using equations III-5 and III-9, it is a trivial extension to obtain the connection between the reduced matrix elements and the polarized angular distribution coefficients. The results are listed in Table B-1.

In this table, the cosines and sines of the phase angles have been omitted for clarity. It is to be understood that where a term in t and t' occurs, there is a $\cos(\phi_t - \phi_{t'})$ in the expressions for the A_k coefficients, and a $\sin(\phi_t - \phi_{t'})$ in the expressions for the B_k coefficients.

Table B-1

Relations between the Angular Distribution Coefficients and the Reduced T-matrix Elements *

$$A_o = 3s^2 + 3d^2 + 5p^2 + 5f^2 + 3p_{1/2}^2 + 3p_{3/2}^2$$

$$A_1 = 9.487sp - 1.342pd + 9.859df - 7.348sp_{3/2} - 5.196p_{3/2}d$$

$$A_2 = 2.5p^2 - 1.5d^2 + 2.857f^2 + 2.243sd - 1.75pf - 3.0p_{1/2}^2 + 1.5p_{3/2}^2 - 9.487p_{3/2}f - 11.619p_{3/2}p$$

$$A_3 = 7.746sf + 8.05pd - 4.382df$$

$$A_4 = -2.857f^2 + 13.997pf$$

$$B_1 = 4.744sp + 2.682pd - 4.930df - 3.674sp_{3/2} + 10.392p_{3/2}d$$

$$B_2 = -2.122sd + 1.458pf + 23.718p_{3/2}f$$

$$B_3 = -2.582sf - 2.683pd + .365df$$

$$B_4 = -3.499pf$$

* Note that unsubscripted p's refer to $p_{3/2}$ E2 capture.

To simplify these expressions, the following replacements are made.

$$
\begin{aligned}
s &\rightarrow s/\sqrt{3} \\
d &\rightarrow d/\sqrt{3} \\
p &\rightarrow p/\sqrt{5} \\
f &\rightarrow f/\sqrt{5} \\
p_{1/2} &\rightarrow p_{1/2}/\sqrt{3} \\
p_{3/2} &\rightarrow p_{3/2}/\sqrt{3}
\end{aligned}
\qquad \text{B-1}
$$

These substitutions lead to the set of equations listed in Table B-2. The cosines and sines have again been omitted for

---

Table B-2

Relations between the Angular Distribution Coefficients and the Reaction Amplitudes *

$A_o = s^2 + p^2 + d^2 + f^2 + p^2_{1/2} + p^2_{3/2}$

$A_1 = 2.450sp - .347pd + 2.546df - 2.449sp_{1/2} - 1.732p_{3/2}d$

$A_2 = .5p^2 - .5d^2 + .571f^2 + 1.414sd - .350pf - p^2_{1/2} + .5p^2_{3/2}$
$\qquad - 3.000p_{3/2}p - 2.450p_{3/2}f$

$A_3 = 2.000sf + 2.079pd - 1.131df$

$A_4 = -5.71f^2 + 2.799pf$

$B_1 = 1.225sp + .692pd - 1.273df - 1.225sp_{3/2} + 2.683p_{3/2}d$

$B_2 = -.737sd + .291pf + 6.124p_{3/2}f$

$B_3 = -.667sf - .693pd + .094df$

$B_4 = -.700pf$

* Note that unsubscripted p's refer to $p_{3/2}$ E2 capture.

---

clarity. In this table, the t's and t''s are now the reaction matrix elements referred to in Chapter III. The t's and t''s of Table B-1 are the actual reduced matrix elements and equations B-1 give the connections between the two.

Table III-2 has been obtained from Table B-2 simply by dropping terms involving $p_{1/2}$ and $p_{3/2}$ partial waves; that is, terms involving M1 radiation.

Appendix C

POLARIZED PROTON BEAM ASYMMETRIES

In this appendix, the asymmetries measurable with a polarized proton beam will be developed. The two detectors used in the experiment will be referred to as left (L) and right (R), with solid angles Ω_L and Ω_R, respectively, the beam polarizations as up ($\uparrow$) and down ($\downarrow$), the yields as Y, and the amount of beam delivered to the target as Q. Then there are four quantities measured, which are (HA 65)

$$Y_{L\uparrow} = Q_{L\uparrow}\, \Omega_{L\uparrow}(1 + P_{L\uparrow}A) \qquad \text{C-1}$$

$$Y_{R\uparrow} = Q_{R\uparrow}\, \Omega_{R\uparrow}(1 - P_{R\uparrow}A) \qquad \text{C-2}$$

$$Y_{L\downarrow} = Q_{L\downarrow}\, \Omega_{L\downarrow}(1 - P_{L\downarrow}A) \qquad \text{C-3}$$

$$Y_{R\downarrow} = Q_{R\downarrow}\, \Omega_{R\downarrow}(1 + P_{R\downarrow}A) \qquad \text{C-4}$$

In these expressions, $Y_{L\uparrow}$ refers to the counts recorded in the left detector when the incident beam is polarized up, etc. It has been assumed that the detectors are not sensitive to the polarization and thus A, the analyzing power of the reaction, is constant throughout.

The following further assumptions are now made. The number of protons incident on the target is assumed to be the same whether viewed from either the left or right detector; thus $Q_L = Q_R$ for each spin state. It will be assumed that the beam does not shift when the spin state is altered, thus $\Omega_\uparrow = \Omega_\downarrow$ for each detector. Finally, it will be assumed that the magnitude of the polarization is the same in the two spin states. With these assumptions, equations C-1 to C-4 become

$$Y_{L\uparrow} = Q_\uparrow \Omega_L (1 + PA) \qquad \text{C-5}$$

$$Y_{R\uparrow} = Q_\uparrow \Omega_R (1 - PA) \qquad \text{C-6}$$

$$Y_{L\downarrow} = Q_\downarrow \Omega_L (1 - PA) \qquad \text{C-7}$$

$$Y_{R\downarrow} = Q_\downarrow \Omega_R (1 + PA) \qquad \text{C-8}$$

The polarized beam asymmetries follow by taking various combinations of these equations.

The analyzing power follows from

$$R = \frac{Y_{L\uparrow} Y_{R\downarrow}}{Y_{L\downarrow} Y_{R\uparrow}} = \frac{(1 + PA)^2}{(1 - PA)^2} \qquad \text{C-9}$$

which leads to

$$A = \frac{1}{P} \frac{\sqrt{R} - 1}{\sqrt{R} + 1} \qquad \text{C-10}$$

The charge ratio asymmetry follows from

$$\frac{Y_{L\uparrow} Y_{R\uparrow}}{Y_{L\downarrow} Y_{R\downarrow}} = \frac{Q_\uparrow^2}{Q_\downarrow^2} \qquad \text{C-11}$$

or

$$\frac{Q_{\uparrow}}{Q_{\downarrow}} = \sqrt{\frac{Y_{L\uparrow}Y_{R\uparrow}}{Y_{L\downarrow}Y_{R\downarrow}}} \tag{C-12}$$

Similarly, the solid angle asymmetry arises from considering

$$\frac{Y_{L\uparrow}Y_{L\downarrow}}{Y_{R\uparrow}Y_{R\downarrow}} = \frac{\Omega_L^2}{\Omega_R^2} \tag{C-13}$$

which gives

$$\frac{\Omega_L}{\Omega_R} = \sqrt{\frac{Y_{L\uparrow}Y_{L\downarrow}}{Y_{R\uparrow}Y_{R\downarrow}}} \tag{C-14}$$